TUDelft

Delft University of Technology

A transientanisotropic gradientenhanced damage model with displacement smoothing for failure analysis in quasibrittle materials

Amani, J.

Important note
To cite this publication, please use the final published version (if applicable).
Please check the document version above.

A transient-anisotropic gradient-enhanced damage model with displacement smoothing for failure analysis in quasi-brittle materials

A transient-anisotropic gradient-enhanced damage model with displacement smoothing for failure analysis in quasi-brittle materials

Proefschrift

door

Jafar AMANI DASHLEJEH

Master of Science in Civil Engineering,
Iran University of Science and Technology, Tehran, Iran
geboren te Ardebil, Iran

Dit proefschrift is goedgekeurd door de promotoren.

Samenstelling promotiecommissie bestaat uit:

Rector magnificus,	voorzitter
Prof. dr.ir. L.J. Sluys	Technische Universiteit Delft, promotor
Prof. dr.ir. A. Simone	University of Padova, Italië, promotor

Onafhankelijke leden:	
Prof. dr. ir. J.G. Rots	Technische Universiteit Delft
Prof. dr. ir. H. Askes	Technische Universiteit Twente
Prof. dr. A. Rodríguez-Ferran	Universitat Politècnica de Catalunya, Spanje
Prof. dr. ing. B. Vandoren	Hasselt University, België
Dr. ir. F. P. van der Meer	Technische Universiteit Delft
Prof. dr. ir M. A. N. Hendriks	Technische Universiteit Delft, reservelid

An electronic version of this dissertation is available at
http://repository.tudelft.nl/.

Dedicated to

all brave women, especially those who struggle for
emancipation and justice in my homeland, Iran.

Contents

List of Abbreviations, Constants & Symbols

Abbreviations:

GEDM Gradient-enhanced damage model

FEM   Finite element method

LEFM Linear elastic fracture mechanics

Constant parameters:

E Young's modulus of material

E_imp Young's modulus of material at imperfection

ν Poisson's ratio of material

f_c Uniaxial compression strength of material

f_t Uniaxial tensile strength of material

k Ratio of uniaxial compression strength to uniaxial tensile strength

L Length of the one-dimentional example

ℓ_0 Length scale

c Constant gradient activity parameter in the GEDM

α Residual parameter in the damage softening law

β Softening parameter in the damage softening law

$\overline{\beta}$ An extra softening parameter in the modified damage softening law $\overline{\omega}$ to control the damage band size

κ_0 Damage threshold equivalent strain in the damage softening law

Symbols:

Ω Whole domain

Γ Boundary of domain Ω

$\Gamma_{\overline{\mathbf{u}}}$ Boundary where prescribed local displacements are applied

$\Gamma_{\overline{\mathbf{t}}}$ Boundary where prescribed tractions are applied

$u, \mathbf{u}$ Local displacements

$\tilde{u}, \tilde{\mathbf{u}}$ Nonlocal displacements

$u^h, \mathbf{u}^h$ FEM term of the local displacement

$\tilde{u}^h, \tilde{\mathbf{u}}^h$ FEM term of the nonlocal displacements

$\overline{u}, \overline{\mathbf{u}}$	Prescribed local displacement on boundary $\Gamma_{\overline{u}}$
$\overline{t}, \overline{\mathbf{t}}$	Prescribed traction on boundary $\Gamma_{\overline{t}}$
$\underline{n}, \underline{\mathbf{n}}$	Unit outward normal vector
ψ	Free energy density potential function
$\sigma, \boldsymbol{\sigma}$	Local stress
$\tilde{\sigma}, \tilde{\boldsymbol{\sigma}}$	Nonlocal stress
$\epsilon, \boldsymbol{\epsilon}$	Local strain
$\tilde{\epsilon}, \tilde{\boldsymbol{\epsilon}}$	Nonlocal strain
e	Local equivalent strain
$\tilde{e}$	Nonlocal equivalent strain
I_1	First invariant of the local strain tensor
$\tilde{I}_1$	First invariant of the nonlocal strain tensor
J_2	Second deviatoric invariant of the local strain tensor
$\tilde{J}_2$	Second deviatoric invariant of the nonlocal strain tensor
$w, \mathbf{w}$	Arbitrary weight/test function applied in the weak formulation of the equilibrium equation
$\tilde{w}, \tilde{\mathbf{w}}$	Arbitrary weight/test function applied in the weak formulation of the diffusion equation
$b, \mathbf{b}$	Body forces
κ	History parameter at material points that stores the largest value of $\tilde{e}$
$\dot{\kappa}$	First derivative of κ
p	Iterator on integration points
$\mathbf{N}$	Shape functions
$\mathbf{M}$	Mass-like matrix in the displacement-based GEDM formulation
$\mathbf{D}$	Diffusivity matrix in the displacement-based GEDM formulation
$\mathbf{f}_{\text{int}}$	Vectorial internal forces
$\mathbf{f}_{\text{ext}}$	Vectorial external forces
f	Loading indicator function
ω	Damage softening law
$\overline{\omega}$	Modified damage softening law with $\alpha = 1$ and $\overline{\beta}$
g	Transient activity function
n	Exponent in the transient activity function $g = 1 - \omega^n$
ω_{crit}	Critical damage used in $g = 1 - \omega^n$
$\mathbf{c}$	Gradient activity matrix
$\overline{\mathbf{c}}$	A matrix that controls the active nonlocal interactions in GEDM obtained by multipying g and $\mathbf{c}$

Summary

It is widely recognized in engineering fracture mechanics that integral and differential forms of nonlocal damage models with a constant internal length scale suffer from an incorrect representation of failure mechanisms either by spurious damage growth or by incorrect damage initiation and propagation. In this regard, in this thesis, a displacement-based gradient-enhanced damage model (GEDM) with a transient internal length scale is formulated and used for failure analysis of quasi-brittle materials. Research is focused on mode-I and mode-II failure mechanisms.

In a GEDM, a local field is enhanced into a nonlocal field and the nonlocal field is the output of the enhancement. Displacement-based GEDM enhances local displacement fields into nonlocal displacement fields instead of enhancing local equivalent strain fields into nonlocal equivalent strain fields, as in strain- and stress-based GEDMs. The key ingredient of the proposed extension is a transient internal length scale that tends to zero as the damage parameter tends to one. Various expressions for this transient internal length scale are proposed, formulated, and discussed. Also, the need for correction on the gradient activity operator in mode-II failure is demonstrated. To this end, an anisotropic formulation of the displacement-based GEDM is formulated and used to control the material failure mechanism in mode-II failure. Examples of the new model regularization capabilities are compared to the original/classical displacement-based GEDM with a constant internal length scale.

Despite the existence of spurious damage growth in mode-I failure for two dimensional problems (4-point bending beam example) for both the transient isotropic and the transient anisotropic versions, spurious damage growth is eliminated for mode-I failure in one-dimensional problems. Also, the proposed transient isotropic model eliminates spurious damage growth for mode-II failure in two-dimensional problems. However, the damage migration issue is not solved. This issue is addressed by the implementation of the transient anisotropic model. The transient anisotropic model has no damage spreading and damage migration issues in mode-II failure and realistic damage initiation and propagation are guaranteed. These features enable the representation of failure patterns i.e., thin crack-like shear-band. In practical terms this leads to a non-broadening shear fracture process zone in the wake of the crack tip, addressing one of the main criticisms of existing gradient damage models. Applicability of the proposed models is demonstrated by representative one- and two-dimensional examples.

Samenvatting

Het wordt algemeen erkend in de technische breukmechanica dat integrale en differentiële vormen van niet-lokale schademodellen met een constante interne lengteschaal lijden aan een onjuiste weergave van faalmechanismen, hetzij door oneigenlijke schadegroei of door onjuiste initiatie en voortplanting van schade. In dit verband wordt in dit proefschrift een verplaatsingsgebaseerd gradiënt-verbeterd schade model (GEDM) met veranderende interne lengteschaal geformuleerd en gebruikt voor faalanalyse van quasi-brosse materialen. Het onderzoek richt zich op mode-I en mode-II faalmechanismen.

In een GEDM wordt een lokaal veld verbeterd tot een niet-lokaal veld en het niet-lokale veld is de output van de verbetering. Op verplaatsing gebaseerde GEDM verbetert het lokale verplaatsingsveld in het niet-lokale verplaatsingsveld in plaats van het lokale equivalent rekveld te versterken in een niet-lokaal equivalent rekveld, zoals in op rek en spanning gebaseerde GEDM's. Het belangrijkste ingrediënt van de voorgestelde uitbreiding is een veranderende interne lengteschaal die naar nul gaat naarmate de schadeparameter naar één gaat. Verschillende uitdrukkingen voor deze veranderende interne lengteschaal worden voorgesteld, geformuleerd en besproken. Ook wordt de noodzaak van correctie van de gradiëntactiviteitsoperator bij falen in mode-II aangetoond. Hiervoor is een anisotrope formulering van het op verplaatsing gebaseerde GEDM geformuleerd en gebruikt om het materiaalfaalmechanisme bij mode-II-falen te beheersen. Voorbeelden van de regularisatiemogelijkheden van het nieuwe model worden vergeleken met de originele/klassieke op verplaatsing gebaseerde GEDM met een constante interne lengteschaal.

Ondanks het optreden van oneigenlijke schadegroei in mode-I-falen voor tweedimensionale problemen (bijvoorbeeld van een 4-punts buigbalk) voor zowel de veranderende isotrope als de veranderende anisotrope modellen, wordt de groei van valse schade geëlimineerd voor mode-I-falen bij één-dimensionale problemen. Ook elimineert het voorgestelde veranderende isotrope model oneigenlijke schade-groei voor mode-II-falen bij twee-dimensionale problemen. Echter, het vertoont nog steeds een probleem met de migratie van schade. Dit probleem wordt verholpen door de implementatie van het veranderende anisotrope model. Het veranderende anisotrope model vertoont geen schade-verspreiding en schade-migratieproblemen bij het falen in mode-II en realistische schade-initiatie en voortplanting zijn gegarandeerd. Deze kenmerken maken de weergave van faalpatronen mogelijk, d.w.z. een dunne discrete afschuifband. In de praktijk leidt dit tot een niet-verbredende afschuif-breukproceszone in de zone achter de scheurtip, waarmee één van de belangrijkste punten van kritiek op bestaande modellen voor gradiëntschade wordt aangepakt. De toepasbaarheid van de voorgestelde modellen wordt aangetoond met behulp van representatieve één- en twee-dimensionale voorbeelden.

Acknowledgments

1

Introduction

1.1. State-of-the-art

For numerous years, materials and structures with a quasi-brittle failure mechanism have attracted significant interest in the computational mechanics community. The representation of zero-thickness strain localization bands using nonlocal approaches is still a significant challenge in computational fracture mechanics.

1.1.1. Quasi-brittle materials failure

A quasi-brittle material (such as concrete and mortar) has a fracture process zone ahead of the crack tip and a large cracking zone prior to the final fracture. These materials often possess defects, such as notches and voids. Their mechanical properties are unaffected by these defects when in their virgin and unstressed state, and they exhibit linear elastic properties when subject to low tensile stresses. With increasing loading, the stress field in the vicinity of defects may cause strain localization within a band due to tensile straining while the material outside the band unloads elastically. In these regions, under further straining, a crack will form [1].

1.1.2. Strain localization

By de Borst et al. [2], strain localization is defined as the appearance of narrow regions in a structure where all further deformation tends to concentrate despite monotonous loading from external forces. This means that large strains will develop in a narrow region leads to increase in the amount of dissipated energy during softening upon mesh refinement. A region of the localized deformation can be represented either by a strong discontinuity (incorporating a jump across the displacement field) and a singularity in the strain field, or by two weak discontinuities (that separate the failure zone from the remaining portion of the body by a band of small but finite thickness and consist of a jump across the strain field) [3].

1

1.1.3. Damage regularization

The numerical simulation of strain localization exhibits instability and mesh dependency when a local damage model is used [4]. To address this issue, damage regularization techniques have been developed to provide a smooth and continuous transition from an undamaged state to a fully damaged state while maintaining stability and avoiding mesh dependency. The fundamental idea behind damage regularization is to introduce a regularization term in the constitutive equations of the material model. This term penalizes the formation of sharp discontinuities in the material response. By introducing this regularization term, the material response becomes smoother, allowing for a more stable and accurate simulation of damage evolution.

One of the simplest regularization methods is the crack-band method [5, 6] which modifies the stress-strain relationship to account for mesh size. More advanced regularization techniques, such as nonlocal damage theories [7], introduce a characteristic length parameter in the constitutive equation or additional regularization equations or variables acting as localization limiters. Nonlocal damage models calculate damage evolution by averaging strains over the neighborhood of a given point, where the size of the neighborhood is determined by the length scale.

1.1.4. Gradient-based nonlocal damage models

The original two-field strain-based formulation of the gradient-enhanced damage model (GEDM) [8] is a type of gradient-based nonlocal damage model which couples the equilibrium equation to a regularizing diffusion equation equipped with a constant diffusion parameter. The diffusion parameter plays an important role in the definition of the active nonlocal interactions between material points. This parameter is known as length scale parameter in the damage mechanics community, and its correlation to quantities related to the microstructure is a matter of ongoing debate; in any case, it could be understood as a localization limiter to obtain mesh-independent results. Due to the incorrect estimation of the active nonlocal interactions with a constant length scale as shown in [9], the energy transfer from integration points inside the fracture process zone to neighboring regions, generates spurious damage growth when using gradient damage models [10]. This phenomenon is more visible at high deformation levels [11]. Figure 1.1 illustrates a schematic representation of spurious damage growth within the GEDM. Figure 1.1.i to Figure 1.1.iv illustrate a schematic damaged zone for four benchmark examples at different load increments (a to e on the force-displacement curve in Figure 1.1.v). Note that bands of the damaged zones at different load increments are displayed in different colors. In the shear-band problem (mode-II) shown in Figure 1.1.iv, a schematic representation of the spurious damage migration indicates movement of the starting point of the shear-band from point A (in the imperfection zone) to point E (out of the imperfection zone), instead of producing a curved crack (shear-band) starting at point A, as confirmed by numerical and experimental results from the literature.

1

(i) Uniaxial tensile bar with imperfection

(ii) Four-point bending beam

(iii) L-shaped panel test

(iv) Shear-band problem

(v) Force-displacement curve
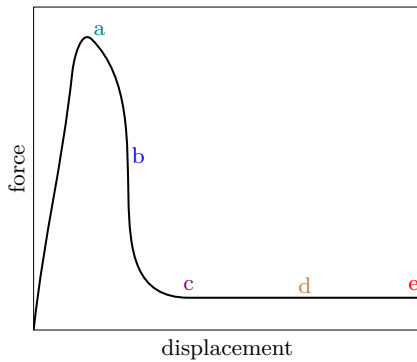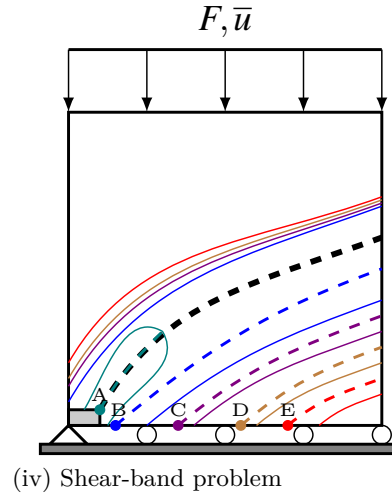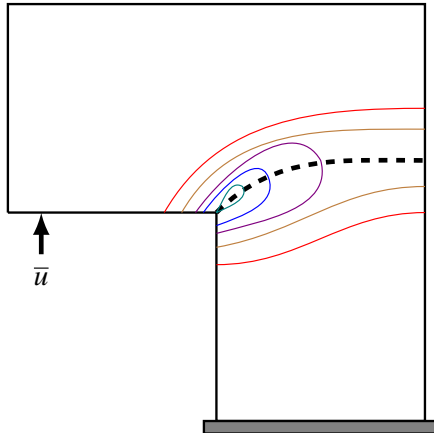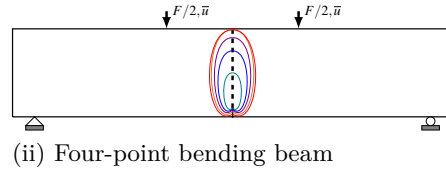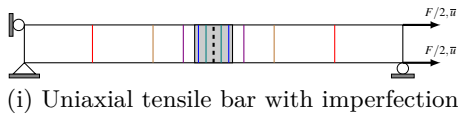
Figure 1.1: Schematic representation of (i) spurious damage widening in a uniaxial tensile bar with central imperfection, (ii) spurious damage widening in a four-point bending beam, (iii) spurious damage widening in L-shaped specimen (iv) spurious damage widening and migration of starting point (from A to E) in shear-band problem, and (v) force-displacement curve with indicated load-increment levels (points a to e). The dashed black line/curve that is illustrated in figures i to iv, shows a schematic representation of a crack that has been observed experimentally/numerically in the literature.

1

As a first attempt to solve this issue in the GEDMs, Geers et al. [10] proposed a three-field strain-based model with a transient internal length scale. They utilized a continuous transient activity parameter governed by an additional continuity equation. In [11] this issue has been more thoroughly investigated and a transient version of the original two-field GEDM is formulated by incorporating a transient length scale inside the regularization equation. Poh and Sun [12] adopted the micromorphic theory in which micro-process interactions are incorporated in the model by using an exponential transient interaction function that is linked with the damage field (transient two-field strain-based GEDM). Wu [13] proposed a geometrically regularized gradient damage model with energetic equivalence and derived the constitutive relations consistently from the standard framework of thermodynamics. They concluded that the localization bandwidth approaches a finite limit value, not exhibiting spurious damage growth. Nguyen et al. [14] introduced a modified evolving anisotropic nonlocal gradient parameter to eliminate spurious damage growth. Negi et al. proposed two types of localizing gradient damage model with smoothed and micromorphic stress-based anisotropic nonlocal interactions proposed in [15] and [16], respectively.

A strain-based or a stress-based model with transient length scale does not lead to a perfectly working model. Rather, it leads to a pathological behavior consisting in the appearance of non-smooth fields as demonstrated by Vandoren and Simone [17]. In an ideal GEDM with a transient length scale, the response at high damage levels should tend to that of the local damage model and behave well without oscillations for zero length scale values.

The displacement-based GEDM proposed by Rodríguez-Ferran et al. [18] is a two-field GEDM equipped with a constant length scale. At variance with other gradient-enhanced models, the diffusion equation is formulated in terms of the non-local/smoothed displacement field rather than a nonlocal equivalent strain. Apart from a constant length scale, the displacement-based model is a good candidate to obtain a model that can properly describe failure initiation and evolution. In this model, differently from classical strain-based models, the same interpolation order for both solution fields (i.e., local and smoothed displacements) can be used.

1.1.5. Spurious/Incorrect damage growth in GEDM

Incorrect damage growth in the gradient-enhanced damage model is the unreal, incorrect or mesh-dependent growth of damage that is caused either by incorrect definition of the regularization equation or by incorrect definition of the nonlocal interactions between material points. In the case of incorrect nonlocal interactions, damage can grow in an incorrect manner from the time when damage is initiated in a material point to the point at which it is fully damaged. This means that, when the nonlocal interactions between material points is "wrong", both spurious damage growth and physically realistic damage growth develop. There are three types of incorrect damage growth that can be observed:

- incorrect damage initiation;
- incorrect damage widening; and
- incorrect damage migration.

Incorrect damage initiation

The most commonly used method for describing crack initiation and propagation in brittle materials is the linear elastic fracture mechanics (LEFM) theory. In the LEFM, the crack is treated as an ideal crack, resulting in a stress singularity at the crack tip, indicating that the stress is infinite. As shown by Simone et al. [20], the strain-based gradient-enhanced damage model was also not able to predict damage initiation correctly due to an inaccurate calculation of the location of the maximum nonlocal equivalent strain. It is caused by an incorrect definition of the regularization equation, which includes nonlocal equivalent strain as an additional unknown parameter, resulting in oscillations in the solution field [17].

Incorrect damage widening

Spurious damage widening is a special case of the spurious damage growth. The term "spurious/incorrect damage widening" is used in this thesis to describe the incorrect increase in damage in a wider zone (see Figure 1.1) caused by the constant/non-vanishing definition of the nonlocal interactions.

Incorrect damage migration

The term "spurious/incorrect damage migration" describes the incorrect movement of the starting point of the shear band (see Figure 1.1.iv) due to the lack of anisotropy of the nonlocal interaction. According to this thesis, incorrect damage migration can only be observed in mode-II. Incorrect damage migration in the model-II case is the main motivation for developing the anisotropic model in this thesis.

1.1.6. First and second deviatoric strain invariants

With strain tensor,

$$\boldsymbol{\epsilon} = \begin{bmatrix} \epsilon_{xx} & \epsilon_{xy} & \epsilon_{xz} \\ \epsilon_{yx} & \epsilon_{yy} & \epsilon_{yz} \\ \epsilon_{zx} & \epsilon_{zy} & \epsilon_{zz} \end{bmatrix}, \tag{1.1}$$

the first invariant of the strain tensor is defined as,

$$I_1 = \text{trace}\left(\boldsymbol{\epsilon}\right) = \epsilon_{xx} + \epsilon_{yy} + \epsilon_{zz}, \tag{1.2}$$

and the second deviatoric strain invariant is,

$$J_2 = \frac{1}{3}\left(\epsilon_{xx}^2 + \epsilon_{yy}^2 + \epsilon_{zz}^2 - \epsilon_{xx}\epsilon_{yy} - \epsilon_{yy}\epsilon_{zz} - \epsilon_{xx}\epsilon_{zz}\right) + \left(\epsilon_{xy}^2 + \epsilon_{yz}^2 + \epsilon_{xz}^2\right). \tag{1.3}$$

1.1.7. Modified von-Mises equivalent strain failure criterion

A modified von-Mises equivalent strain [21] is defined as:

$$e = \frac{k-1}{2k\left(1-2\nu\right)}I_1 + \frac{1}{2k}\sqrt{\left(\frac{k-1}{1-2\nu}I_1\right)^2 + \frac{12k}{\left(1+\nu\right)^2}J_2}, \tag{1.4}$$

where $k = f_c/f_t$ in which f_c and f_t are the uniaxial compressive and the uniaxial tensile strengths of the material, respectively and ν is the Poisson's ratio and I_1 is the first strain invariant and J_2 is the second deviatoric strain invariant.

1.1.8. Exponential damage evolution function

An exponential damage softening law is defined as

$$\omega = 1 - \frac{\kappa_0}{\kappa}\left[1 - \alpha + \alpha \exp\left(-\beta(\kappa - \kappa_0)\right)\right], \tag{1.5}$$

where κ is a history parameter that stores the largest value of the nonlocal equivalent strain, $\tilde{e}$, that the materiel point has experienced during the loading process (it is therefore a non-decreasing function of strain). The initial value of κ at the first load-increment is defined by the threshold value κ_0 of the nonlocal strain. The material parameters α and β are positive and dimensionless and can be calibrated by experimental tests; they define, respectively, a parameter for controlling the residual stress and a parameter for controlling softening of a material point.

1.1.9. Loading indicator function

In Equation (1.5), damage initiates as soon as the nonlocal equivalent strain $\tilde{e}$ exceeds the threshold nonlocal strain value κ_0 and grows according to the Kuhn-Tucker conditions [22]

$$f \leq 0, \qquad \dot{\kappa} \geq 0, \qquad f\dot{\kappa} = 0, \tag{1.6}$$

where the loading function,

$$f = \tilde{e} - \kappa, \tag{1.7}$$

verifies if the material point undergoes loading $(f \geq 0)$ or unloading $(f < 0)$. In this thesis, the loading indicator function is defined as follows,

$$\text{loading indicator function} = \begin{cases} 1 & \text{if } f \geq 0 \\ 0 & \text{else} \end{cases}. \tag{1.8}$$

1.2. Objectives and outline

The main objective of this work is the development of a novel GEDM for failure analysis of quasi-brittle materials. Based on the available displacement-based GEDM [18], transient and anisotropic models are proposed that aim to remove incorrect nonlocal interactions that are the source for both incorrect damage widening and incorrect damage migration issues. Throughout this thesis, the term incorrect damage widening is used to refer to the incorrect damage growth caused by incorrect isotropic definitions of the nonlocal interactions. The term incorrect damage migration refers to the incorrect damage growth due to the lack of anisotropy of nonlocal interactions. These two incorrect damage types can not be clearly distinguished. Both incorrect damage migration and widening as a result of incorrect isotropic definition of nonlocal interactions, as well as incorrect anisotropic definition of the nonlocal interactions may occur.

For the development of the new model, the following sub-objectives (SOs) are defined:

- SO-1: Develop a damage model for removing incorrect damage widening.
- SO-2: Develop a damage model for removing incorrect damage migration.

Following this brief introduction, the rest of this thesis is organized as follows:

- In Chapter 2, different transient activity functions to address incorrect damage widening in the displacement-based GEDM are proposed. A one-dimensional benchmark example, a bar with central imperfection under tensile load, is considered and a mesh-sensitivity study is performed for the proposed transient activity functions. We have selected four functions from among the fifteen transient activity functions that have been tested and reported as the most significant.
- The isotropic formulation of the transient displacement-based GEDM is formulated and tested for two-dimensional problems in Chapter 3.
- Chapter 4 proposes an anisotropic formulation of the transient displacement-based GEDM. The capabilities of the model with respect to the definition of thin damage bands without damage widening and damage migration issues are discussed.
- Lastly, some concluding remarks are presented in Chapter 5.

It should be noted that a full integration scheme is employed throughout this thesis and for the two-dimensional studies that are presented in Chapters 3 and 4, the transient activity function $g_{\tilde{u}}$ that is proposed for a one-dimensional case in Section 2.3.4 is employed. Different types of boundary conditions (Dirichlet, homogeneous Neumann, non-homogeneous Neumann, and combined) are investigated by Tamayo-Mas and Rodríguez-Ferran [23]. As part of the implementation process of this thesis, all of these boundary conditions were tested and discussed. According to Table 1.1, only the combined BC is reported in the thesis.

As the main focus has been the definition of a new model that could address the main drawbacks of the classical strain-based GEDM, a comparison of the results with experimental data is out of the scope of this research. The computer code used to generate the results presented in this work is based on the Jem/Jive library [24], an object-oriented C++ code for finite element analysis. Gmsh software [25] is used

Table 1.1: Summary of boundary conditions and their properties [23].

	Dirichlet	Homogeneous Neumann	Non-homogeneous Neumann	Combined
Reproducibility of order 1	✓	✗	✓	✓
Displacement smoothing along the boundary	✗	✓	✓	✓
Local response normal to boundaries	✓	✗	✗	✓
Volume preservation	✓	✗	✗	✓

to generate meshes, with the resulting mesh files sent as input to Jem/Jive. Using the Paraview software [26], the contours are plotted by saving Jem/Jive outputs in Paraview format. TikZ [27] is also used to plot all curves and evolutionary plots in Chapter 2.

References

[1] M. Cervera, M. Chiumenti, and R. Codina, Mixed stabilized finite element methods in nonlinear solid mechanics: Part ii: Strain localization, Computer Methods in Applied Mechanics and Engineering 199, 2571 (2010).

[2] R. de Borst, L. Sluys, H.-B. Mühlhaus, and J. Pamin, Fundamental issues in finite element analyses of localization of deformation, Engineering Computations 10, 99 (1993).

[3] M. Jirásek, in Continuous and discontinuous modelling of cohesive-frictional materials, edited by P. A. Vermeer, H. J. Herrmann, S. Luding, W. Ehlers, S. Diebels, and E. Ramm (Springer, Berlin, Heidelberg, 2001) Chap. Modeling of localized damage and fracture in quasibrittle materials, pp. 17–29.

[4] J. C. Simo, J. Oliver, and F. Armero, An analysis of strong discontinuities induced by strain-softening in rate-independent inelastic solids, Computational mechanics 12, 277 (1993).

[5] S. Pietruszczak and Z. Mroz, Finite element analysis of deformation of strain-softening materials, International Journal for Numerical Methods in Engineering 17, 327 (1981).

[6] Z. P. Bažant, Crack band model for fracture of geomaterials, in Proceedings of the 4th international conference on numerical methods in geomechanics, Vol. 3 (Edmonton, University of Alberta) pp. 1137–1152.

[7] G. Pijaudier-Cabot and Z. P. Bažant, Nonlocal damage theory, Journal of engineering mechanics 113, 1512 (1987).

[8] R. Peerlings, R. R. de Borst, W. Brekelmans, and J. de Vree, Gradient enhanced damage for quasi-brittle materials, International Journal for Numerical Methods in Engineering 39, 3391 (1996).

[9] G. Pijaudier-Cabot, K. Haidar, and J.-F. Dubé, Non-local damage model with evolving internal length, International journal for numerical and analytical methods in geomechanics 28, 633 (2004).

[10] M. Geers, R. de Borst, W. Brekelmans, and R. Peerlings, Strain-based transient-gradient damage model for failure analyses, Computer Methods in Applied Mechanics and Engineering 160, 133 (1998).

[11] S. Saroukhani, R. Vafadari, and A. Simone, A simplified implementation of a gradient-enhanced damage model with transient length scale effects, Computational Mechanics 51, 899 (2013).

[12] L. H. Poh and G. Sun, Localizing gradient damage model with decreasing interactions, International Journal for Numerical Methods in Engineering 110, 503 (2017).

1

[13] J.-Y. Wu, A geometrically regularized gradient-damage model with energetic equivalence, Computer Methods in Applied Mechanics and Engineering 328, 612 (2018).

[14] T. H. A. Nguyen, T. Q. Bui, and S. Hirose, Smoothing gradient damage model with evolving anisotropic nonlocal interactions tailored to low-order finite elements, Computer Methods in Applied Mechanics and Engineering 328, 498 (2018).

[15] A. Negi and S. Kumar, Localizing gradient damage model with smoothed stress based anisotropic nonlocal interactions, Engineering Fracture Mechanics 214, 21 (2019).

[16] A. Negi, S. Kumar, and L. H. Poh, A localizing gradient damage enhancement with micromorphic stress-based anisotropic nonlocal interactions, International Journal for Numerical Methods in Engineering 121, 4003 (2020).

[17] B. Vandoren and A. Simone, Modeling and simulation of quasi-brittle failure with continuous anisotropic stress-based gradient-enhanced damage models, Computer Methods in Applied Mechanics and Engineering 332, 644 (2018).

[18] A. Rodríguez-Ferran, I. Morata, and A. Huerta, A new damage model based on non-local displacements, International Journal for numerical and analytical methods in geomechanics 29, 473 (2005).

[19] A. C. Eringen, C. Speziale, and B. Kim, Crack-tip problem in non-local elasticity, Journal of the Mechanics and Physics of Solids 25, 339 (1977).

[20] A. Simone, H. Askes, and L. J. Sluys, Incorrect initiation and propagation of failure in non-local and gradient-enhanced media, International Journal of Solids and Structures 41, 351 (2004).

[21] J. De Vree, W. Brekelmans, and M. Van Gils, Comparison of nonlocal approaches in continuum damage mechanics, Computers and Structures 55, 581 (1995).

[22] H. W. Kuhn and A. W. Tucker, Nonlinear programming, in in Jerzy Neyman (ed.), Proceedings 2nd Berkeley Symposium on Mathematical Statistics and Probability (Berkeley, University of California Press, 1950) pp. 481–492.

[23] E. Tamayo-Mas and A. Rodríguez-Ferran, A medial-axis-based model for propagating cracks in a regularised bulk, International Journal for Numerical Methods in Engineering 101, 489 (2015).

[24] E. Lingen and M. Stroeven, Jem/jive-a c++ numerical toolkit for solving partial differential equations, (2002).

[25] C. Geuzaine and J.-F. Remacle, Gmsh: A 3-d finite element mesh generator with built-in pre-and post-processing facilities, International journal for numerical methods in engineering 79, 1309 (2009).

1

[26] J. Ahrens, B. Geveci, and C. Law, ParaView: An End-User Tool for Large Data Visualization, Visualization Handbook (Elsevier, 2005).

[27] T. Tantau, Graph drawing in TikZ, in Proceedings of the 20th International Conference on Graph Drawing, GD'12, edited by W. Didimo and M. Patrignani (Springer, Berlin, Heidelberg, 2013) pp. 517–528.

2

Transient displacement-based GEDM: One-dimensional study

It is widely recognized that both integral and gradient forms of the nonlocal damage models with a constant internal length scale suffer from incorrect representation of failure mechanisms by either spurious damage growth or incorrect damage initiation and propagation. In this regard, in this chapter different types of transient activity functions are proposed to address incorrect damage widening in the displacement-based gradient-enhanced damage model. The key ingredient of the proposed extension is a gradient length scale that tends to zero as the damage parameter tends to one. Various expressions for this transient length scale are proposed and discussed. A one-dimensional benchmark example, a bar under uniaxial tension, is considered and a mesh-sensitivity study is performed for the proposed transient activity functions. The results show the efficiency of the proposed transient displacement-based GEDM to remove damage widening in the one-dimensional setting.

2.1. Introduction

A constant internal length scale in the strain-based integral or differential nonlocal damage models leads to an incorrect representation of failure mechanisms in terms of damage initiation, evolution, and widening [1, 2]. While damage initiation can be successfully addressed by means of anisotropic reformulations [3], damage widening and evolution require procedures that aim to reduce the nonlocal interaction. To the best of our knowledge, none of the procedures proposed so far in the context of strain-based models derived from the gradient-enhanced damage model by Peerlings et al. [4] has been successful. In this chapter, it is argued that this type of models has intrinsic features that prevent a reasonably simple and general solution. Rather, we advocate the use of displacement-based models.

Since the proposals of the nonlocal damage model of the integral type by Pijaudier-Cabot and Bažant [5] and its differential reformulation by Peerlings et al. [4], the study of failure processes in quasi-brittle materials has been addressed using strain-based models in the vast majority of cases. A strain-based nonlocal damage model is a regularized damage model in which damage is driven by a nonlocal equivalent strain. In the context of the differential version (known in the literature as implicit GEDM [4]), the nonlocal equivalent strain is a scalar field variable whose governing equation is a diffusion equation (modified Helmholtz equation); coupling with the equilibrium equation occurs through the dependence of the damage field on the nonlocal equivalent strain which in turns depends on the strain tensor. Both integral and differential versions were proposed with a constant length scale parameter.

The popularity of nonlocal models stems from their effectiveness in addressing mesh dependency caused by strain-softening in the constitutive models of a rate-independent media, together with their conceptual and implementational simplicity. Nonetheless, despite their popularity, these models are inherently flawed because of:

1. incorrect damage initiation far from crack tip [2, 6];
2. incorrect damage widening during the localization process [1]; and
3. incorrect damage migration during the localization process in mode-II dominated problems [2].

These issues are shared by both integral and differential versions of the nonlocal damage model. Our current understanding leads to the conclusion that these issues are caused by a constant length scale parameter and the anisotropy of the weight function in both local and nonlocal models. Most of the literature is dedicated to the solution of the first issue. The first to recognize the problems were Geers et al. [1] who proposed a strain-based GEDM with a transient internal length scale. A simpler version of this model was later proposed by Saroukhani et al. [7]. Notable improvements were proposed by Poh and Sun [8], Wu [9], and Nguyen et al. [10].

The common strategy adopted in these models is the reduction of the internal length scale through a scaling factor that decreases with increasing deformation levels. In an ideal situation, the internal length scale should vanish, thus removing nonlocal interaction and, consequently, eliminating incorrect damage growth. Since the length scale does not go to zero, incorrect damage growth is going to take place because the equation is a diffusion equation. As such, as long as there is a diffusion equation there will be incorrect damage unless the internal length scale

goes to zero and the model does not show any pathological behavior. Based on the following strong-form governing equations, we can see that for both strain-based and displacement-based models, the local displacement field as the first primary unknown has $\mathcal{C}^0$ continuity between elements (a piecewise linear function), resulting in $\mathcal{C}^{-1}$ continuity (a constant function) of the local equivalent strain field, e.

$$\frac{\mathrm{d}\sigma}{\mathrm{d}x} + b = 0, \tag{2.1}$$

$$\text{regularization of strain-based} \quad : \quad \tilde{e} - \frac{\mathrm{d}}{\mathrm{d}x}\left(c\frac{\mathrm{d}\tilde{e}}{\mathrm{d}x}\right) = e, \tag{2.2}$$

$$\text{regularization of displacement-based} \quad : \quad \tilde{u} - \frac{\mathrm{d}}{\mathrm{d}x}\left(c\frac{\mathrm{d}\tilde{u}}{\mathrm{d}x}\right) = u, \tag{2.3}$$

As the second primary unknown in the strain-based model, the nonlocal equivalent strain field $\tilde{e}$, has $\mathcal{C}^0$ continuity. In the case of zero length scale, $\ell_0 = 0$, the strong form identity $\tilde{e} = e$ must be satisfied. Therefore, in the strain-based model, the continuity of the local and nonlocal equivalent strains are not consistent, leading to oscillations in the solution field [3]. In the displacement-based model, the nonlocal displacement field, as the second unknown has $\mathcal{C}^0$ continuity, leads to $\mathcal{C}^{-1}$ continuity of the equivalent nonlocal strain field. With zero length scale, $\ell_0 = 0$, the strong-form identity $\tilde{u} = u$ is inherently satisfied. Hence, unlike the strain-based model, the displacement-based model has the same continuity for both local and nonlocal strain fields. This fact naturally solves the issue of inconsistent continuity and has the added advantage that oscillations in the solution field are eliminated for a transient length scale. Another important feature of the displacement-based model in its standard formulation [11] is the correct definition of the crack tip field.

Although damage widening has been discussed in detail for the strain-based model, any other model with a diffusion equation equipped with a constant internal length scale is prone to suffer from it. To the best of our knowledge, damage widening is one of the main drawbacks of the standard formulation of the displacement-based model. To properly present our proposal to address the damage widening issue, this chapter is organized as follows. Section 2.2 derives the governing one-dimensional equations of the displacement-based GEDM with transient length scale. Definitions of the proposed transient activity functions are described in Section 2.3. Different transient activity functions to address the incorrect damage widening in the displacement-based GEDM are proposed. The performance of the proposed model for the analysis of quasi-static failure by means of a one-dimensional benchmark example, a bar with central imperfection under tensile load, is demonstrated in Section 2.4. Lastly, some concluding remarks are presented in Section 2.5.

2.2. Governing equations and discretization
2.2.1. Strong-form equations and boundary conditions

A one-dimensional displacement-based GEDM with a transient length scale is formulated by means of a system of coupled differential equations expressed in terms of the classical equilibrium equation and the regularizing diffusion equation as (see [11] for the two-dimensional version)

$$\frac{\mathrm{d}\sigma}{\mathrm{d}x} + b = 0, \quad \text{on} \quad 0 \le x \le L, \tag{2.4}$$

$$\tilde{u} - \frac{\mathrm{d}}{\mathrm{d}x}\left(gc\frac{\mathrm{d}\tilde{u}}{\mathrm{d}x}\right) = u, \quad \text{on} \quad 0 \le x \le L, \tag{2.5}$$

subject to the following Dirichlet and Neumann boundary conditions applied on the local displacement field u and its gradient:

$$u = \overline{u}, \quad \text{at} \quad x = 0 \quad \text{and/or} \quad x = L, \tag{2.6}$$

$$\sigma\,\underline{n} = \overline{t}, \quad \text{at} \quad x = 0 \quad \text{and/or} \quad x = L, \tag{2.7}$$

and the following Dirichlet-type boundary condition applied on the nonlocal/smoothed displacement field $\tilde{u}$:

$$\tilde{u} = u, \quad \text{at} \quad x = 0 \quad \text{and} \quad x = L, \tag{2.8}$$

in which $\overline{u}$ and $\overline{t}$ are the prescribed displacement and traction at the boundaries, respectively defined by $\overline{u} = \overline{u}_{x=0}$ and $\overline{t} = \overline{t}_{x=0}$ at $x = 0$ and $\overline{u} = \overline{u}_{x=L}$ and $\overline{t} = \overline{t}_{x=L}$ at $x = L$. The unit outward normal $\underline{n}$ at the boundaries $x = 0$ and $x = L$ are defined by $\underline{n} = -1$ and $\underline{n} = 1$, respectively and σ and b are the stress and the body force, respectively. The system of coupled equations consists of two main unknowns, the local displacement field u and the nonlocal displacement field $\tilde{u}$. The transient activity function g and the constant gradient activity parameter c control the active nonlocal interactions between microcracks. Details regarding the weak formulation and the definition of the discrete governing equations are discussed next.

2.2.2. Weak formulation

The weighted residual approach is used to obtain the weak-form of the governing equations. To this end, Equations (2.4) and (2.5) are multiplied by the scalar functions w and $\tilde{w}$, respectively. The resulting equations are then integrated over problem domain $0 \le x \le L$ yielding

$$\int_0^L \left[w\left(\frac{\mathrm{d}\sigma}{\mathrm{d}x} + b\right)\right]\mathrm{d}x = 0, \tag{2.9}$$

$$\int_0^L \left[\tilde{w}\left(\tilde{u} - \frac{\mathrm{d}}{\mathrm{d}x}\left(gc\frac{\mathrm{d}\tilde{u}}{\mathrm{d}x}\right)\right)\right]\mathrm{d}x = \int_0^L [\tilde{w}u]\,\mathrm{d}x. \tag{2.10}$$

Using the identities

$$w \left(\frac{\mathrm{d}\sigma}{\mathrm{d}x} \right) = \frac{\mathrm{d}\,(w\sigma)}{\mathrm{d}x} - \frac{\mathrm{d}w}{\mathrm{d}x}\sigma, \tag{2.11}$$

$$\tilde{w} \left[\frac{\mathrm{d}}{\mathrm{d}x} \left(gc\frac{\mathrm{d}\tilde{u}}{\mathrm{d}x} \right) \right] = \frac{\mathrm{d}}{\mathrm{d}x} \left(\tilde{w}gc\frac{\mathrm{d}\tilde{u}}{\mathrm{d}x} \right) - \frac{\mathrm{d}\tilde{w}}{\mathrm{d}x}gc\frac{\mathrm{d}\tilde{u}}{\mathrm{d}x}, \tag{2.12}$$

and

$$\int_0^L \left[\frac{\mathrm{d}\,(w\sigma)}{\mathrm{d}x} \right] \mathrm{d}x = w\left[(\sigma)_{x=L} - (\sigma)_{x=0}\right] = 0, \tag{2.13}$$

$$\int_0^L \left[\frac{\mathrm{d}}{\mathrm{d}x} \left(\tilde{w}gc\frac{\mathrm{d}\tilde{u}}{\mathrm{d}x} \right) \right] \mathrm{d}x = \tilde{w}\left[(gc\frac{\mathrm{d}\tilde{u}}{\mathrm{d}x})_{x=L} - (gc\frac{\mathrm{d}\tilde{u}}{\mathrm{d}x})_{x=0}\right] = 0, \tag{2.14}$$

gives

$$\int_0^L \left[-\frac{\mathrm{d}w}{\mathrm{d}x}\sigma + wb \right] \mathrm{d}x = 0, \tag{2.15}$$

$$\int_0^L \left[\tilde{w}\tilde{u} + \frac{\mathrm{d}\tilde{w}}{\mathrm{d}x}gc\frac{\mathrm{d}\tilde{u}}{\mathrm{d}x} \right] \mathrm{d}x = \int_0^L \left[\tilde{w}u \right] \mathrm{d}x. \tag{2.16}$$

2.2.3. Finite element discretization

The Bubnov-Galerkin method is employed for the discretization of the governing weak-form equations. To this end, the local and nonlocal displacement fields, along with the corresponding weight functions, are discretized as follows:

$$u = \mathbf{N}\mathbf{u}^h, \quad w = \mathbf{N}\mathbf{w}^h, \quad \frac{\mathrm{d}u}{\mathrm{d}x} = \frac{\mathrm{d}\mathbf{N}}{\mathrm{d}x}\mathbf{u}^h, \quad \frac{\mathrm{d}w}{\mathrm{d}x} = \frac{\mathrm{d}\mathbf{N}}{\mathrm{d}x}\mathbf{w}^h, \tag{2.17}$$

$$\tilde{u} = \mathbf{N}\tilde{\mathbf{u}}^h, \quad \tilde{w} = \mathbf{N}\tilde{\mathbf{w}}^h, \quad \frac{\mathrm{d}\tilde{u}}{\mathrm{d}x} = \frac{\mathrm{d}\mathbf{N}}{\mathrm{d}x}\tilde{\mathbf{u}}^h, \quad \frac{\mathrm{d}\tilde{w}}{\mathrm{d}x} = \frac{\mathrm{d}\mathbf{N}}{\mathrm{d}x}\tilde{\mathbf{w}}^h, \tag{2.18}$$

in which the shape function matrix $\mathbf{N}$ interpolates both nodal displacements u and $\tilde{u}$. For a linear element with nodes i and j,

$$\mathbf{u}^h \;\; = \;\; \left[\begin{array}{cc} u_i^h & u_j^h \end{array} \right]^{\mathrm{T}}, \tag{2.19}$$

$$\tilde{\mathbf{u}}^h \;\; = \;\; \left[\begin{array}{cc} \tilde{u}_i^h & \tilde{u}_j^h \end{array} \right]^{\mathrm{T}}, \tag{2.20}$$

$$\mathbf{w}^h \;\; = \;\; \left[\begin{array}{cc} w_i^h & w_j^h \end{array} \right]^{\mathrm{T}}, \tag{2.21}$$

$$\tilde{\mathbf{w}}^h \; = \; \left[\begin{array}{cc} \tilde{w}_i^h & \tilde{w}_j^h \end{array} \right]^{\mathrm{T}}, \tag{2.22}$$

$$\mathbf{N} \; = \; \left[\begin{array}{cc} N_i & N_j \end{array} \right], \tag{2.23}$$

$$\frac{\mathrm{d}\mathbf{N}}{\mathrm{d}x} \; = \; \left[\begin{array}{cc} \frac{\partial N_i}{\partial x} & \frac{\partial N_j}{\partial x} \end{array} \right]. \tag{2.24}$$

Inserting the above relations into Equations (2.15) and (2.16) and considering the expressions evaluated at integration points, p, yields

$$\sum_p \mathbf{w}^{h\,\mathrm{T}} \frac{\mathrm{d}\mathbf{N}}{\mathrm{d}x}^{\mathrm{T}} \sigma_p \mathrm{d}x_p = \sum_p \mathbf{w}^{h\,\mathrm{T}} \mathbf{N}^{\mathrm{T}} b_p \mathrm{d}x_p, \tag{2.25}$$

$$\sum_p \left[\tilde{\mathbf{w}}^{h\,\mathrm{T}} \mathbf{N}^{\mathrm{T}} \mathbf{N} \tilde{\mathbf{u}}^h + \tilde{\mathbf{w}}^{h\,\mathrm{T}} \frac{\mathrm{d}\mathbf{N}}{\mathrm{d}x}^{\mathrm{T}} g c_p \frac{\mathrm{d}\mathbf{N}}{\mathrm{d}x} \tilde{\mathbf{u}}^h - \tilde{\mathbf{w}}^{h\,\mathrm{T}} \mathbf{N}^{\mathrm{T}} \mathbf{N} \mathbf{u}^h \right] \mathrm{d}x_p = \mathbf{0}, \tag{2.26}$$

which have to hold for any choice of $\mathbf{w}$ and $\tilde{\mathbf{w}}$. The term $\mathrm{d}x_p = J_p w_p$ is the volume of the integration point obtained by multiplication of the Jacoabian matrix J by weight value w at each integration point.

By defining $\mathbf{M}$ and $\mathbf{D}$ as the mass-like and diffusivity matrices

$$\mathbf{M} = \sum_p \mathbf{N}^{\mathrm{T}} \mathbf{N} \mathrm{d}x_p, \tag{2.27}$$

$$\mathbf{D} = \sum_p \frac{\mathrm{d}\mathbf{N}}{\mathrm{d}x}^{\mathrm{T}} g_p c_p \frac{\mathrm{d}\mathbf{N}}{\mathrm{d}x} \mathrm{d}x_p, \tag{2.28}$$

the final discretized form of the governing equations can be written as

$$\sum_p \frac{\mathrm{d}\mathbf{N}}{\mathrm{d}x}^{\mathrm{T}} \sigma_p \mathrm{d}x_p = \sum_p \mathbf{N}^{\mathrm{T}} b_p \mathrm{d}x_p + \left[\mathbf{N}^{\mathrm{T}} \bar{t}_p \right]_{x=0,L} \tag{2.29}$$

$$\mathbf{M} \tilde{\mathbf{u}}^h + \mathbf{D} \tilde{\mathbf{u}}^h - \mathbf{M} \mathbf{u}^h = \mathbf{0}. \tag{2.30}$$

Finally, the discretized governing equations are rewritten in terms of external and internal nodal forces according to

$$\mathbf{f}_{\mathrm{int}}^u = \mathbf{f}_{\mathrm{ext}}^u, \tag{2.31}$$

$$\mathbf{f}_{\text{int}}^{\tilde{u}} = \mathbf{f}_{\text{ext}}^{\tilde{u}}, \tag{2.32}$$

where

$$\mathbf{f}_{\text{int}}^{u} = \sum_{p} \frac{\text{d}\mathbf{N}}{\text{d}x}^{\text{T}} \sigma_p \text{d}x_p, \tag{2.33}$$

$$\mathbf{f}_{\text{ext}}^{u} = \sum_{p} \mathbf{N}^{\text{T}} b_p \text{d}x_p + \left[\mathbf{N}^{\text{T}}\bar{t}_p\right]_{x=0,L}, \tag{2.34}$$

$$\mathbf{f}_{\text{int}}^{\tilde{u}} = \mathbf{M}\tilde{\mathbf{u}}^{h} + \mathbf{D}\tilde{\mathbf{u}}^{h} - \mathbf{M}\mathbf{u}^{h}, \tag{2.35}$$

$$\mathbf{f}_{\text{ext}}^{\tilde{u}} = \mathbf{0}. \tag{2.36}$$

2.2.4. Consistent linearization

A consistent tangent stiffness is obtained by linearization of Equations (2.31) and (2.32) at iteration $i + 1$ with respect to the previous iteration i. Accordingly,

$$\mathbf{f}_{\text{ext},i+1}^{u} = \mathbf{f}_{\text{int},i}^{u} + \delta\mathbf{f}_{\text{int},i+1}^{u}, \tag{2.37}$$

$$\mathbf{f}_{\text{ext},i+1}^{\tilde{u}} = \mathbf{f}_{\text{int},i}^{\tilde{u}} + \delta\mathbf{f}_{\text{int},i+1}^{\tilde{u}}, \tag{2.38}$$

gives

$$\delta\mathbf{f}_{\text{int},i+1}^{u} = \mathbf{f}_{\text{ext},i+1}^{u} - \mathbf{f}_{\text{int},i}^{u}, \tag{2.39}$$

$$\delta\mathbf{f}_{\text{int},i+1}^{\tilde{u}} = \mathbf{f}_{\text{ext},i+1}^{\tilde{u}} - \mathbf{f}_{\text{int},i}^{\tilde{u}}, \tag{2.40}$$

where

$$\delta\mathbf{f}_{\text{int},i+1}^{u} = \sum_{p} \left[\frac{\text{d}\mathbf{N}}{\text{d}x}^{\text{T}} \delta\sigma_{p,i+1}\right] \text{d}x_p, \tag{2.41}$$

$$\delta\mathbf{f}_{\text{int},i+1}^{\tilde{u}} = \mathbf{M}\delta\tilde{\mathbf{u}}_{i+1}^{h} - \mathbf{M}\delta\mathbf{u}_{i+1}^{h} + \mathbf{D}\delta\tilde{\mathbf{u}}_{i+1}^{h} + \delta\mathbf{D}_{i+1}\tilde{\mathbf{u}}^{h}. \tag{2.42}$$

To obtain the stress variation at integration point, $\delta\sigma_{p,i+1}$, first, we assume the free energy density potential function, ψ, as

$$\psi = \frac{1}{2}(1 - \omega)\,\epsilon : E : \epsilon, \tag{2.43}$$

where ω is the damage softening law and E is the elastic modulus and ϵ is the strain. Then, the stress and its derivative can be obtained through

$$\sigma = \frac{\partial\psi}{\partial\epsilon} = (1 - \omega)\,E\epsilon, \tag{2.44}$$

from which

$$\delta\sigma_{i+1} = (1 - \omega_i)\, E\delta\epsilon_{i+1} - E\epsilon_i\delta\omega_{i+1}, \tag{2.45}$$

with

$$\delta\epsilon_{i+1} = \frac{\mathrm{d}\mathbf{N}}{\mathrm{d}x}\delta\mathbf{u}_{i+1}^h, \tag{2.46}$$

$$\delta\tilde{\epsilon}_{i+1} = \frac{\mathrm{d}\mathbf{N}}{\mathrm{d}x}\delta\tilde{\mathbf{u}}_{i+1}^h, \tag{2.47}$$

$$\delta\omega_{i+1} = \left(\frac{d\omega}{d\tilde{\epsilon}}\right)_i \delta\tilde{\epsilon}_{i+1} = \left(\frac{d\omega}{d\kappa}\right)_i \left(\frac{d\kappa}{d\tilde{e}}\right)_i \left(\frac{d\tilde{e}}{d\tilde{\epsilon}}\right)_i \frac{\mathrm{d}\mathbf{N}}{\mathrm{d}x}\delta\tilde{\mathbf{u}}_{i+1}^h, \tag{2.48}$$

yielding

$$\delta\sigma_{i+1} = (1 - \omega_i)\, E\frac{\mathrm{d}\mathbf{N}}{\mathrm{d}x}\delta\mathbf{u}_{i+1}^h - E\epsilon_i\left(\frac{d\omega}{d\tilde{\epsilon}}\right)_i \frac{\mathrm{d}\mathbf{N}}{\mathrm{d}x}\delta\tilde{\mathbf{u}}_{i+1}^h. \tag{2.49}$$

In general, $\mathbf{D}$ can be defined as a function of $\mathbf{u}_{i+1}^h$ and $\tilde{\mathbf{u}}_{i+1}^h$ and therefore

$$\delta\mathbf{D}_{i+1} = \left(\frac{\mathrm{d}\mathbf{D}}{\mathrm{d}\mathbf{u}^h}\right)_i \delta\mathbf{u}_{i+1}^h + \left(\frac{\mathrm{d}\mathbf{D}}{\mathrm{d}\tilde{\mathbf{u}}^h}\right)_i \delta\tilde{\mathbf{u}}_{i+1}^h, \tag{2.50}$$

leads to

$$\begin{aligned}
\delta\mathbf{f}_{\mathrm{int},i+1}^u &= \sum_p \left[\frac{\mathrm{d}\mathbf{N}^{\mathrm{T}}}{\mathrm{d}x}(1 - \omega_{p,i})\, E_p \frac{\mathrm{d}\mathbf{N}}{\mathrm{d}x}\right]\delta\mathbf{u}_{i+1}^h \mathrm{d}x_p \\
&\quad - \sum_p \left[\frac{\mathrm{d}\mathbf{N}^{\mathrm{T}}}{\mathrm{d}x} E_p\epsilon_{p,i}\left(\frac{\mathrm{d}\omega_p}{\mathrm{d}\tilde{\epsilon}_p}\right)_i \frac{\mathrm{d}\mathbf{N}}{\mathrm{d}x}\right]\delta\tilde{\mathbf{u}}_{i+1}^h \mathrm{d}x_p,
\end{aligned} \tag{2.51}$$

$$\delta\mathbf{f}_{\mathrm{int},i+1}^{\tilde{u}} = \left[-\mathbf{M} + \frac{\mathrm{d}\mathbf{D}}{\mathrm{d}\mathbf{u}^h}\tilde{\mathbf{u}}^h\right]\delta\mathbf{u}_{i+1}^h + \left[\mathbf{M} + \mathbf{D} + \frac{\mathrm{d}\mathbf{D}}{\mathrm{d}\tilde{\mathbf{u}}^h}\tilde{\mathbf{u}}^h\right]\delta\tilde{\mathbf{u}}_{i+1}^h. \tag{2.52}$$

The governing equations in the Newton-Raphson iteration are expressed as

$$\underbrace{\begin{bmatrix} \mathbf{K}_{uu}^i & \mathbf{K}_{u\tilde{u}}^i \\ \mathbf{K}_{\tilde{u}u}^i & \mathbf{K}_{\tilde{u}\tilde{u}}^i \end{bmatrix}}_{4\times4} \underbrace{\begin{bmatrix} \delta u^{i+1} \\ \delta\tilde{u}^{i+1} \end{bmatrix}}_{4\times1} = \underbrace{\begin{bmatrix} \mathbf{f}_{\mathrm{ext},i+1}^u - \mathbf{f}_{\mathrm{int},i}^u \\ \mathbf{f}_{\mathrm{ext},i+1}^{\tilde{u}} - \mathbf{f}_{\mathrm{int},i}^{\tilde{u}} \end{bmatrix}}_{4\times1}, \tag{2.53}$$

with the components of the consistent tangent matrix given by, for a 2-node bar

element,

$$
\underset{2\times2}{\underline{\mathbf{K}}^i_{uu}} \;\; = \;\; \sum_p \left[\underset{2\times1}{\frac{\mathrm{d}\mathbf{N}}{\mathrm{d}x}}^{\mathrm{T}} \underset{\text{scalar}}{(1-\omega_{p,i})} \underset{\text{scalar}}{E_p} \underset{1\times2}{\frac{\mathrm{d}\mathbf{N}}{\mathrm{d}x}} \right] \mathrm{d}x_p,
$$

(2.54)

$$
\underset{2\times2}{\underline{\mathbf{K}}^i_{u\tilde{u}}} \;\; = \;\; \sum_p \left[-\underset{2\times1}{\frac{\mathrm{d}\mathbf{N}}{\mathrm{d}x}}^{\mathrm{T}} \underset{\text{scalar}}{E_p} \underset{\text{scalar}}{\epsilon_{p,i}} \underset{\text{scalar}}{\left(\frac{\mathrm{d}\omega}{\mathrm{d}\tilde{\epsilon}}\right)}_i \underset{1\times2}{\frac{\mathrm{d}\mathbf{N}}{\mathrm{d}x}} \right] \mathrm{d}x_p,
$$

(2.55)

$$
\underset{2\times2}{\underline{\mathbf{K}}^i_{\tilde{u}u}} \;\; = \;\; -\underset{2\times2}{\underline{\mathbf{M}}} + \underset{2\times1}{\frac{\mathrm{d}\mathbf{D}}{\mathrm{d}\mathbf{u}^h}} \underset{1\times2}{\tilde{\mathbf{u}}^h},
$$

(2.56)

$$
\underset{2\times2}{\underline{\mathbf{K}}^i_{\tilde{u}\tilde{u}}} \;\; = \;\; \underset{2\times2}{\underline{\mathbf{M}}} + \underset{2\times2}{\underline{\mathbf{D}}} + \underset{2\times1}{\frac{\mathrm{d}\mathbf{D}}{\mathrm{d}\tilde{\mathbf{u}}^h}} \underset{1\times2}{\tilde{\mathbf{u}}^h},
$$

(2.57)

where

$$
\underset{2\times2}{\underline{\frac{\mathrm{d}\mathbf{D}}{\mathrm{d}\mathbf{u}^h}}\tilde{\mathbf{u}}^h} \;\; = \;\; \sum_p \left[\underset{1\times2}{\frac{\mathrm{d}g_p}{\mathrm{d}\mathbf{u}^h}} \underset{2\times1}{\tilde{\mathbf{u}}^h} \underset{2\times1}{\frac{\mathrm{d}\mathbf{N}}{\mathrm{d}x}}^{\mathrm{T}} \underset{\text{scalar}}{c_p} \underset{1\times2}{\frac{\mathrm{d}\mathbf{N}}{\mathrm{d}x}} \right] \mathrm{d}x_p,
$$

(2.58)

$$
\underset{2\times2}{\underline{\frac{\mathrm{d}\mathbf{D}}{\mathrm{d}\tilde{\mathbf{u}}^h}}\tilde{\mathbf{u}}^h} \;\; = \;\; \sum_p \left[\underset{1\times2}{\frac{\mathrm{d}g_p}{\mathrm{d}\tilde{\mathbf{u}}^h}} \underset{2\times1}{\tilde{\mathbf{u}}^h} \underset{2\times1}{\frac{\mathrm{d}\mathbf{N}}{\mathrm{d}x}}^{\mathrm{T}} \underset{\text{scalar}}{c_p} \underset{1\times2}{\frac{\mathrm{d}\mathbf{N}}{\mathrm{d}x}} \right] \mathrm{d}x_p.
$$

(2.59)

2.3. Transient activity function

In this section, different transient activity functions are proposed to equip the displacement-based GEDM with features for the removal of spurious damage growth. The transient activity functions are defined in the following forms:

1. Binary function;
2. Function linked to the damage field;
3. Function linked to both damage and nonlocal equivalent strain fields; and
4. Function based on equivalent dissipation with the strain-based model.

2.3.1. Binary function

As a preliminary attempt for removing spurious damage growth in the displacement-based GEDM, a binary function was selected in which g changes from one to zero when a material point is fully damaged ($\omega = 1$). It should be noticed that $\omega = 1$ is never reached in the case of an exponential damage softening law (from a computational view point this adds a requirement to identify a "fully" damaged integration point by defining an extra model parameter as a critical damage value in the form of $\omega_{\text{crit}} = 1 - \epsilon$ in which ϵ is sufficiently small).

2.3.2. Transient activity function linked to the damage field

An improved version of the binary function that yields a smooth decay of the transient activity function from one to zero and also avoids the extra model parameter ω_{crit} is defined as a function of the damage field: $g(\omega, n) = 1 - \omega^n$. The behavior of this function depends on the values of the exponent n:

- For $-\infty \leq n < 0$, the function returns a negative value and is not acceptable;
- For $n = 0$, the value of g is constant (equal to zero) and results into a local model;
- For $0 < n < 1$, the derivative of g is non-zero for a fully damaged material point;
- For $n = 1$, the derivative of g with respect to damage is equal to a constant value;
- For $1 < n < \infty$, defining a transient activity function is acceptable; and
- For $n \to \infty$, the function behaves like a binary function, switching from one to zero without the requirement of the definition of the extra parameter ω_{crit}.

There are qualitative differences in the derivative of the function with respect to damage when $n \leq 1$ compared to the case $n > 1$. We also noticed that simulations performed with $n \leq 1$ were not stable. Hence, the exponent n should be a real number larger than one.
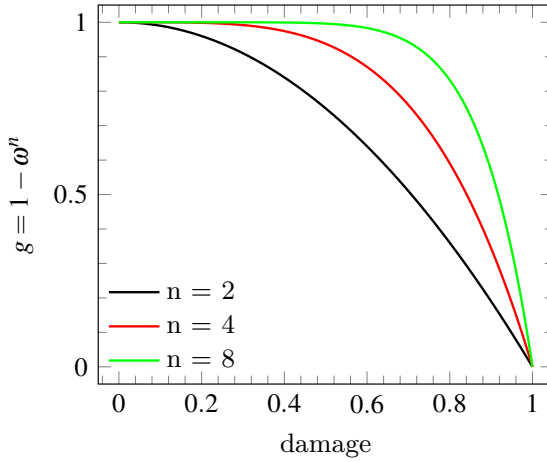
Figure 2.1: Behavior of the transient activity function $g = 1 - \omega^n$ in terms of the exponent n.

The behavior of the transient activity function $g(\omega, n) = 1 - \omega^n$ for increasing damage levels and in terms of the exponent n is plotted in Figure 2.1. The figure shows that the speed of decay of the function is inversely proportional to the value of the exponent n. Figure 2.2 shows the behavior of the transient activity function for increasing nonlocal equivalent strain levels also in terms of the exponent n. At the level of the nonlocal equivalent strain, the model with a smaller exponent n value has lower nonlocal interactions (smaller g value).
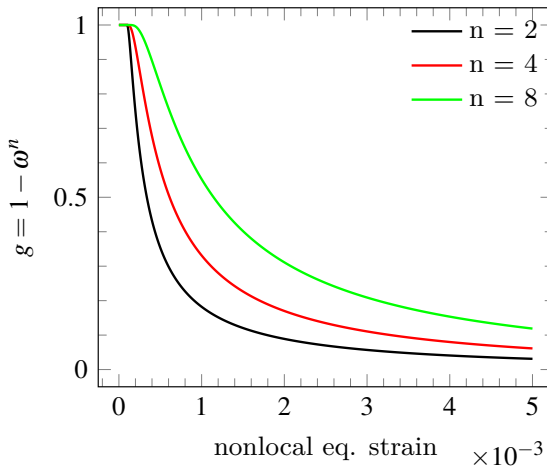

Figure 2.2: Behavior of the transient activity function $g = 1 - \omega^n$ in terms of the nonlocal equivalent strain.

2.3.3. Transient activity function linked to both damage and nonlocal equivalent strain fields

As it will be shown later, a binary activity function or a transient activity function linked to the damage field are not optimal choices. The former choice gives rise to the generation of unrealistic spikes in the solution fields when the damage profile is smooth. Also, a similar issue arises by using $g = 1 - \omega^n$ with a large value of the exponent n. At first glance the function $g = 1 - \omega^n$ with a small value of the exponent n is a good candidate for removing spurious damage growth. However, based on our numerical investigation, localization happens too quickly and results in mesh-dependent results for two-dimensional problems. Here, our aim is to define a transient activity function in such a way that it decays to zero naturally and leads to a delay of the localization process in a smoother manner. To this end, the transient activity function presented in [3] is employed. This function links damage and nonlocal equivalent strain fields as follows

$$g_{\tilde{e}}(\overline{\omega}, \tilde{e}) = \begin{cases} \frac{\tilde{e}}{\kappa_0} & \text{if} \quad \tilde{e} < \kappa_0 \\ (1 - \overline{\omega})\frac{\tilde{e}}{\kappa_0} & \text{else} \end{cases}, \tag{2.60}$$

where $\overline{\omega} = 1 - \frac{\kappa_0}{\kappa}\left[\exp(-\overline{\beta}(\kappa - \kappa_0))\right]$ is the damage value obtained using the modified exponential damage softening law obtained with $\overline{\alpha} = 1$ and $\overline{\beta}$ (the latter is as an extra model parameter used to control the damage band size). In this thesis, to avoid defining a new extra model parameter, we take $\overline{\beta} = \beta$ in which β is the material parameter used in the damage evolution law. It should anyway be stressed that this is just a choice and $\overline{\beta}$ can be different than β.

Figure 2.3 compares the force-displacement responses of strain-based and displacement based GEDMs with a constant internal length scale and a transient activity function $g_{\tilde{e}}$. Based on Figure 2.3, we notice that the displacement-based model and the strain-based model produce the same force-displacement curves with a constant length scale but different curves when equipped with the same transient activity function $g_{\tilde{e}}$. This indicates that the displacement-based model dissipates energy at a faster rate compared to the strain-based model, resulting in a more brittle response when a transient activity function is employed.
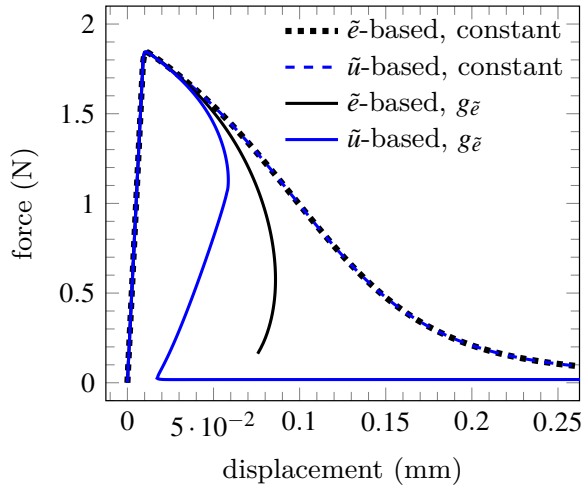
Figure 2.3: Comparison of force-displacement responses of the displacement-based and the strain-based models with constant and transient activity function using 1600 elements (one row of four-node quadrilateral elements).

2.3.4. Transient activity function based on equivalent dissipation with the strain-based model

To compensate for the fast decay of the load-displacement curve in the displacement-based model shown in Figure 2.3, we propose to enforce the same diffusion as the strain-based model in the displacement-based model. Since the strain-based model does not suffer from the issues described earlier about premature localization, this leads to the conclusion that for the displacement-based model to produce acceptable results the two models should somehow be made equivalent. This can be achieved by using a strong-form equivalence of the two governing diffusion equations which basically implies taking the derivative of the governing diffusion equation of the displacement-based model and equating the two source terms. Hence, the actual expression of the transient activity function in the displacement-based model depends on the expression of the transient activity function in the strain-based model.

To derive a new transient activity function, consider the following governing diffusion equations of the strain-based and the displacement-based models:

$$\tilde{e} - \frac{\mathrm{d}}{\mathrm{d}x}\left(g_{\tilde{e}} c_{\tilde{e}} \frac{\mathrm{d}\tilde{e}}{\mathrm{d}x} \right) = e, \tag{2.61}$$

$$\tilde{u} - \frac{\mathrm{d}}{\mathrm{d}x}\left(g_{\tilde{u}} c_{\tilde{u}} \frac{\mathrm{d}\tilde{u}}{\mathrm{d}x} \right) = u. \tag{2.62}$$

By equating the local strain fields, directly available from the first equation and obtained from $e = \mathrm{d}u/\mathrm{d}x$ applied to the second equation we obtain the relation

$$\tilde{e} - \frac{\mathrm{d}}{\mathrm{d}x}\left(g_{\tilde{e}} c_{\tilde{e}} \frac{\mathrm{d}\tilde{e}}{\mathrm{d}x} \right) = \frac{\mathrm{d}}{\mathrm{d}x}\left[\tilde{u} - \frac{\mathrm{d}}{\mathrm{d}x}\left(g_{\tilde{u}} c_{\tilde{u}} \frac{\mathrm{d}\tilde{u}}{\mathrm{d}x} \right) \right]. \tag{2.63}$$

Considering now $c_{\tilde{e}} = c_{\tilde{u}}$ and by using $\tilde{e} = \mathrm{d}\tilde{u}/\mathrm{d}x$ yield, after some simplifications, the following first-order linear ordinary differential equation

$$\frac{\mathrm{d}g_{\tilde{u}}}{\mathrm{d}\tilde{e}} + \frac{1}{\tilde{e}} g_{\tilde{u}} = \frac{1}{\tilde{e}} g_{\tilde{e}}, \tag{2.64}$$

whose general solution is

$$
g_{\tilde{u}} = \frac{\int_0^\infty \exp\left(\int_0^\infty \frac{1}{\tilde{e}} d\tilde{e}\right) \frac{1}{\tilde{e}} g_{\tilde{e}} d\tilde{e} + C_1}{\exp\left(\int_0^\infty \frac{1}{\tilde{e}} d\tilde{e}\right)}
$$

(2.65)

$$
= \frac{\int_0^\infty -\frac{1}{\tilde{e}^2} \exp\left(\frac{1}{\tilde{e}}\right) \frac{1}{\tilde{e}} g_{\tilde{e}} d\tilde{e} + C_1}{-\frac{1}{\tilde{e}^2} \exp\left(\frac{1}{\tilde{e}}\right)}
$$

$$
= \left[\int_0^\infty \frac{1}{\tilde{e}} g_{\tilde{e}} d\tilde{e}\right] + C_2
$$

$$
= \frac{1}{\tilde{e}}\left[\int_0^{\kappa_0} g_{\tilde{e}} d\tilde{e} + \int_{\kappa_0}^\infty g_{\tilde{e}} d\tilde{e}\right] + C_2
$$

$$
= \frac{1}{\tilde{e}}\left[\int_0^{\kappa_0} \left(\frac{\tilde{e}}{\kappa_0}\right) d\tilde{e} + \int_{\kappa_0}^\infty \left((1-\overline{\omega})\frac{\tilde{e}}{\kappa_0}\right) d\tilde{e}\right] + C_2
$$

$$
= \frac{\kappa_0}{\tilde{e}} + \frac{1}{\tilde{e}}\left[\int_{\kappa_0}^\infty \left(\exp\left(-\overline{\beta}(\kappa-\kappa_0)\right)\frac{\tilde{e}}{\kappa} d\tilde{e}\right)\right] + C_2,
$$

with $\kappa = \tilde{e}$

$$
g_{\tilde{u}} = \frac{\kappa_0}{\tilde{e}} + \frac{1}{\tilde{e}}\left[\int_{\kappa_0}^\infty \left(\exp\left(-\overline{\beta}(\tilde{e}-\kappa_0)\right) d\tilde{e}\right)\right] + C_2.
$$

(2.66)

Integration of the above function yields

$$
g_{\tilde{u}} = \begin{cases} 1 & \text{if} \quad \tilde{e} < \kappa_0 \\ \frac{1}{\tilde{e}}\left[\kappa_0 - \frac{1}{\beta}\left(\exp\left(-\beta(\tilde{e}-\kappa_0)\right) - 1\right)\right] & \text{else} \end{cases}.
$$

(2.67)

Figure 2.4 compares the force-displacement responses obtained with the proposed $g_{\tilde{u}}$ function against that obtained using the $g_{\tilde{e}}$ function. The figure indicates that the two curves for the transient models are basically identical, with the displacement-based model load-displacement curve being smoother than that corresponding to the transient strain-based model at the end of the snap-back branch. Figure 2.5 compares the evolutions of different transient activity functions against the nonlocal equivalent strain. It is evident that the proposed transient activity function $g_{\tilde{u}}$ delays the localization process and decays to zero at a slower pace compared to the other two curves (red and black).
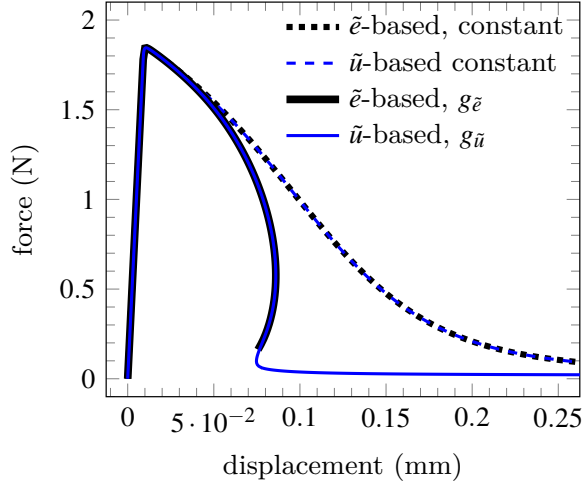
2

Figure 2.4: Comparison of force-displacement responses of the displacement-based and the strain-based models with constant and transient activity functions using 1600 elements.
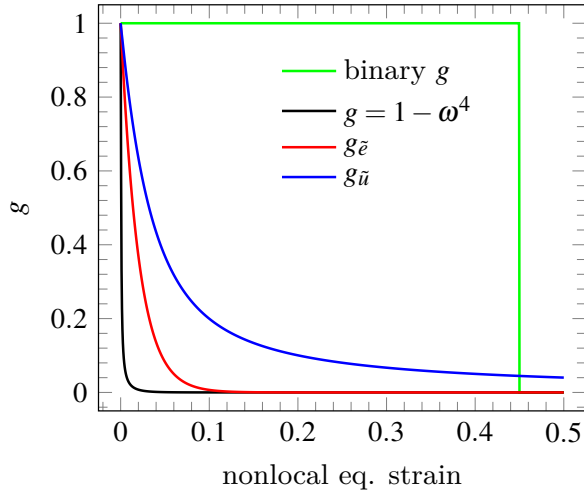

Figure 2.5: Comparison of different transient activity functions: Variations of various g functions with nonlocal equivalent strain.

Table 2.1: Uniaxial tensile bar: material and numerical parameters.

properties	symbol	value
Young's modulus	E	20×10^3 MPa
Young's modulus of imperfection	E_{imp}	18×10^3 MPa
Poisson's ratio	ν	0
constant gradient activity parameter	c	1 mm^2
damage softening law	ω	exponential
damage-initiation threshold	κ_0	10^{-4}
softening parameter	β	50
residual parameter	α	0.99

2.4. Results and discussions

To check the performance of the proposed transient displacement-based GEDM, a one-dimensional uniaxial bar with length of 100 mm and a central imperfection subject to a uniaxial tensile load as shown in Figure 2.6 is used. The imperfection is influenced by a 10 percent reduction of the Young's modulus in the central part of the bar with length of 10 mm. Material and numerical parameters are listed in Table 2.1.

For the discretization, a bilinear quadrilateral (Q4) element type is used for both local and nonlocal displacement fields. The simulation starts with displacement control until dissipation becomes significant or convergence becomes problematic in the case of existence of snap-back in the load-displacement curve due to unloading. Then the simulation continues with an energy-based arc-length control until loading is detected; at that point the solution algorithm switches back to the displacement control. It is important to note that, in simulations involving a binary activity function as described in Section 2.4.2, only displacement control is utilized. This is because multiple solutions can arise, leading to unreliable results when snap-back occurs. A detailed discussion of this issue can be found in Section 2.4.2.

As shown in Table 2.1, damage growth at a material point (i.e., an integration point) is described by an exponential damage softening law. In the following one-dimensional example, the material is assumed to fail only in tension; hence, the strain is only supposed to increase. Therefore the equivalent strain measure to be used is the absolute value of the axial strain $\tilde{e} = |\tilde{\varepsilon}_{xx}|$. This is identical to the value obtained using the Mazar's criterion where only the positive part of the strain is considered. In the modified von-Mises equivalent strain model, this can be achieved by using an infinite (i.e., very large) value of k.
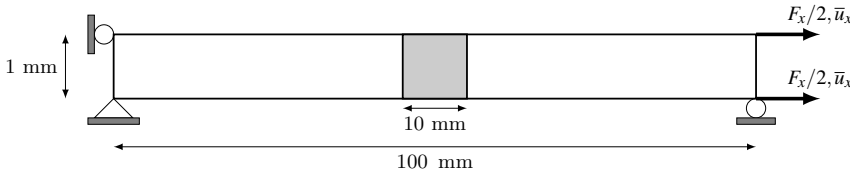

Figure 2.6: A uniaxial tensile bar with central imperfection: geometry and boundary conditions.
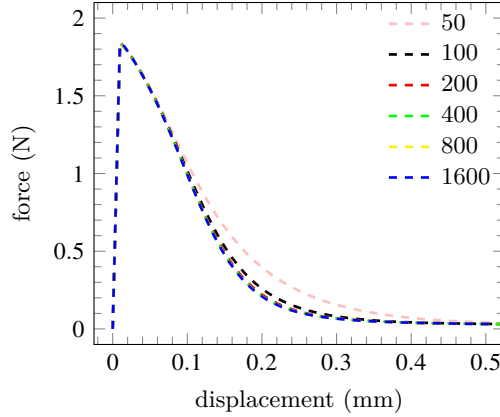
2

Figure 2.7: Mesh sensitivity study using a constant length scale.

2.4.1. Damage spreading in the classical model

Figure 2.7 shows a mesh-sensitivity study for the one-dimensional tensile bar test with the constant activity function. In this example, six mesh configurations with 50, 100, 200, 400, 800 and 1600 bilinear quadrilateral elements in the horizontal direction and one element in vertical direction are employed. The evolution of damage, nonlocal equivalent strain, and loading indicator function for the results with 400 elements are plotted in Figure 2.8 a, b and c, respectively. For the standard model the evolution of the transient activity function is constant ($g = 1$) and is therefore not reported. Figure 2.8a shows that the damaged region expands as the load increases. This is supported by the increasing values of the nonlocal equivalent strain and the loading indicator function during the evolution process, as demonstrated in Figure 2.8b and Figure 2.8c, respectively.

2.4.2. Preliminary binary function

Figure 2.9 shows a mesh-sensitivity study for the one-dimensional tensile bar test with a binary gradient activity function. The curves are obtained with a displacement control algorithm and the parameter $\omega_{\text{crit}} = 0.9999$. The drops in the force-displacement curves are due to the use of a displacement control algorithm to trace the equilibrium path. Figure 2.10a, b, c, d and e show the evolution of damage, non-local equivalent strain, loading indicator function, transient activity function and horizontal displacement with 400 elements for the transient model with a binary activity function, respectively. Apart from needing an extra input parameter ω_{crit} as a critical damage level, the following numerical issues arise by using a binary function:

- Spurious damage growth increases by using a larger value of ω_{crit} because the model behaves like the standard model up until very high strain levels.

- As shown in Figure 2.11 for $c = 5 \text{ mm}^2$, by using larger value of the length
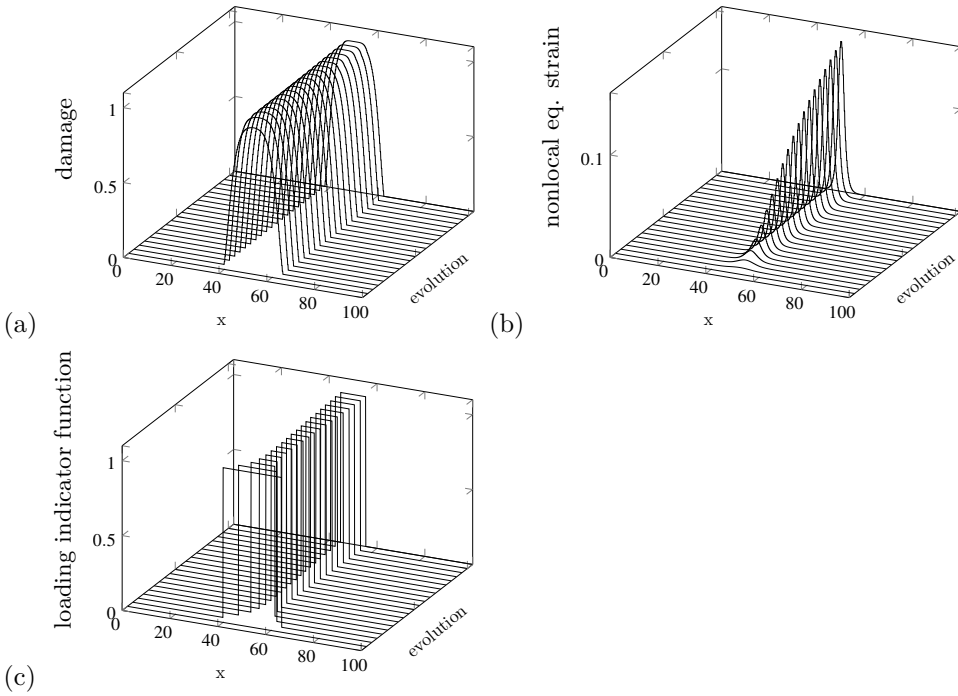
Figure 2.8: Evolution of (a) damage, (b) nonlocal equivalent strain and (c) loading indicator function for the standard model with 400 elements and $c = 1$ mm^2. Evolution axis is up to 0.5 mm.

scale, the damage profile plateaus (becomes flat in a large central portion of the bar) and strain localization happens in more than one random location in the central region, mainly determined by round-off errors and the error tolerance used in the Newton-Raphson iterative procedure (although the relative large value of the length scale and critical damage level are also partly responsible for this behavior). Using a strict error tolerance to identify the material points with maximum damage value somehow solves the issue but the tolerance turns out to be problem-dependent.
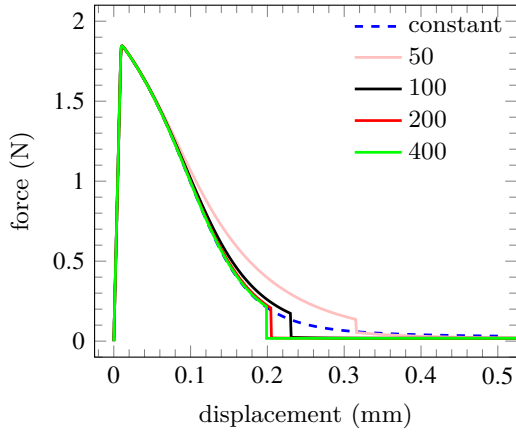
Figure 2.9: Mesh sensitivity study using transient model with binary activity function and ω_{crit} = 0.9999. The case with dashed blue line corresponds to the converged solution of the model with a constant gradient activity parameter obtained using 1600 elements.
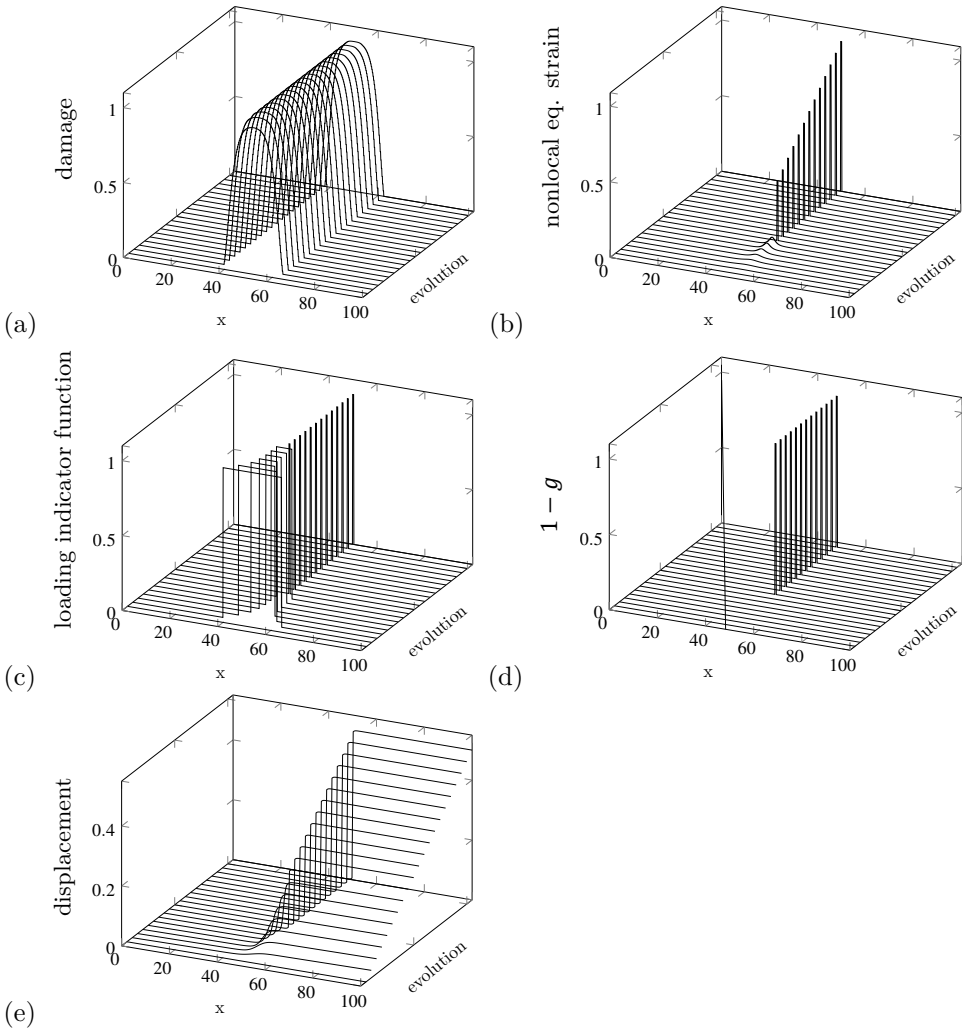
Figure 2.10: Evolution of (a) damage, (b) nonlocal equivalent strain, (c) loading indicator function, (d) $1 - g$ and (e) horizontal displacement using a binary activity function with 400 elements, $\omega_{\text{crit}} = 0.9999$ and $c = 1 \text{ mm}^2$. Evolution axis is up to 0.5 mm.
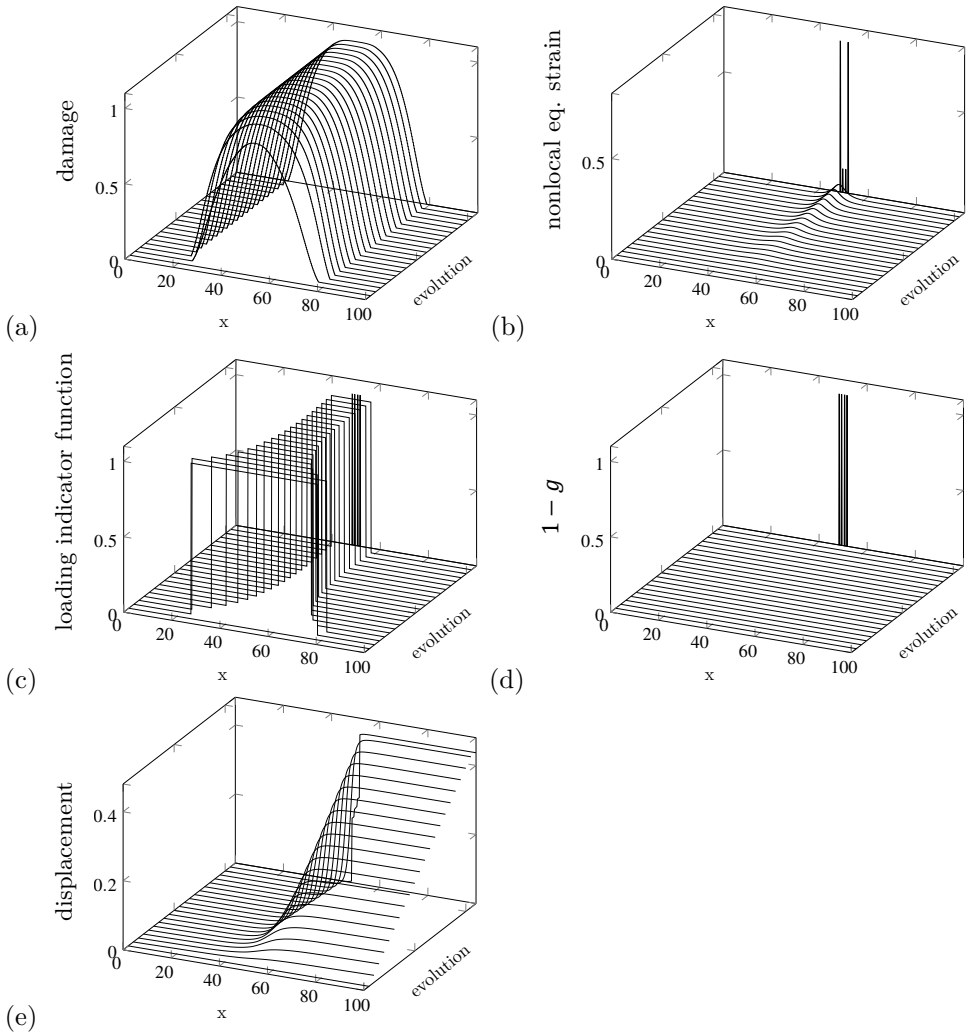
Figure 2.11: Evolution of (a) damage, (b) nonlocal equivalent strain, (c) loading indicator function, (d) $1-g$ and (e) horizontal displacement using a binary activity function with 400 elements ($\omega_{\text{crit}} = 0.9999$ and $c = 5$ mm^2). The spikes in panels (b) and (d) appear when the damage profile is flat (due to relative large value of length scale, critical damage level, and tolerance). Such a behavior happens for instance with a slack error tolerance (equal to 10^{-4} for displacements control instead of 10^{-6} or 10^{-2} for energy control instead of 10^{-4}). In these cases, the solution field localizes incorrectly in more than one element leading to the creation of more than one spike in the damage evolution plot. The expected final profiles should contain a single spike in the center of the bar. Evolution axis is up to 0.4367 mm.

2.4.3. Transient activity function linked to the damage field

The problem with the transient activity functions $g(\omega, n) = 1 - \omega^n$ is that the decreasing nonlocal interaction between material points is too fast, causing premature mesh-sensitivity as illustrated in Figure 2.13 for $n = 4$. Mesh sensitivity, in this case, starts as soon as the load-displacement curve shows a snap-back response. We can postpone the appearance of the snap-back point by increasing the exponent n until the response becomes identical to that of the standard model (i.e., a constant gradient activity function). The problem with large values of the exponent n is the appearance of damage spreading. As shown in Figure 2.12, a mesh configuration with 1600 elements is used to investigate the effect of the exponent n on the force-displacement responses, and the responses are compared to the force-displacement response obtained by the model with a constant length scale. It is evident that increasing the exponent n delays localization. By using $n = \infty$ the function $g = 1 - \omega^n$ tends to the binary function and decays to zero without needing an extra input parameter ω_{crit}.

Figure 2.13 shows a mesh-sensitivity study in terms of the force-displacement curves performed with $g = 1 - \omega^4$. Figure 2.14 shows that by using $g = 1 - \omega^4$ damage broadening is removed, but, as shown in Figure 2.13, the convergence to a mesh-dependent results is too slow means requirement of a very fine mesh size in the damaged region. In addition, our numerical investigations in a two-dimensional setting shows its mesh-dependency. The local response of the model in terms of damage and nonlocal equivalent strain fields offers a more complete picture of what is happening: the only way to stop damage spreading is to stop spreading of the nonlocal equivalent strain.

A possible solution is to delay the decay of the transient activity function with the introduction of a residual R and a critical damage value ω_{crit} to set the transient activity function to zero. Such a modification allows the model to build up damage up to significant strain level thus releasing a reduced amount of elastic energy after the critical damage level is reached. The residual R can be introduced by a modification of the $g(\omega, n)$ function as in $g(\omega, n, R, \omega_{\text{crit}}) = 1 - (1 - R)\,\omega^n$. This function however can generate spikes (as shown in Figure 2.11) when the damage profile is too flat.

2
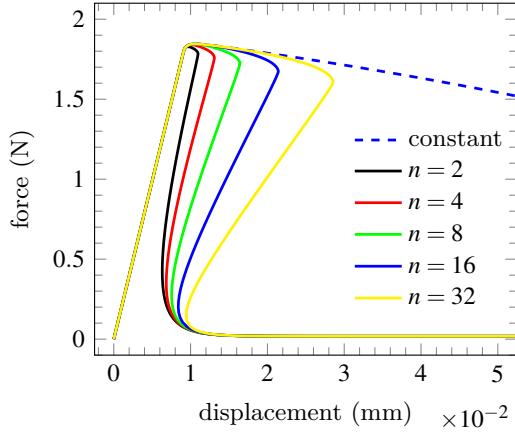
Figure 2.12: Effect of n in $g = 1 - \omega^n$ on the force-displacement response (with 1600 elements). The case with dashed blue line corresponds to the converged solution of the model with a constant gradient activity parameter obtained using 1600 elements.


Figure 2.13: Mesh sensitivity study using $g = 1 - \omega^4$. The case with dashed blue line corresponds to the converged solution of the model with a constant gradient activity parameter obtained using 1600 elements.

Figure 2.14: Evolution of (a) damage, (b) nonlocal equivalent strain, (c) loading indicator function, (d) $1 - g$ and (e) horizontal displacement using $g = 1 - \omega^4$ with 400 elements. Evolution axis is up to 0.05 mm.

2.4.4. Transient activity function from strain-based model

Figure 2.15 shows a mesh-sensitivity study obtained with the $g_{\tilde{e}}$ function. The evolutions of damage, nonlocal equivalent strain, loading indicator function, transient activity function and horizontal displacement with 400 elements are plotted in Figure 2.16a, b, c, d and e, respectively. Comparison of the force-displacement curves with the force-displacement curves obtained by $g = 1 - \omega^4$ indicates the performance of this function to delay the localization process (and the spikes in the evolution profiles discussed earlier are not present anymore).
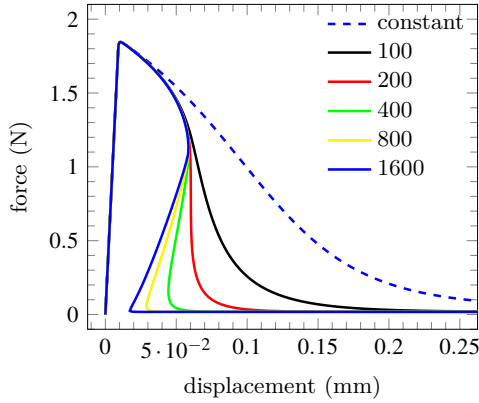
Figure 2.15: Mesh sensitivity study using a transient activity function $g_{\tilde{e}}$ from a strain-based model. The case with dashed blue line corresponds to the converged solution of the model with a constant gradient activity parameter obtained using 1600 elements
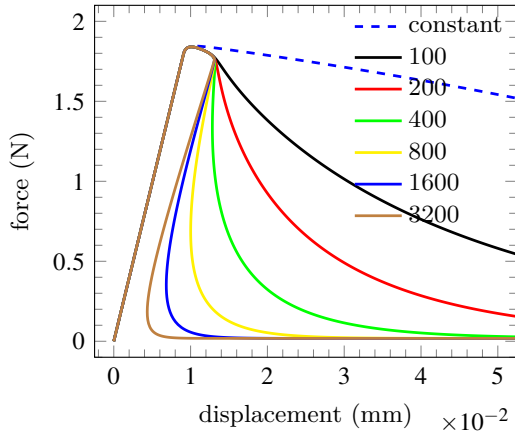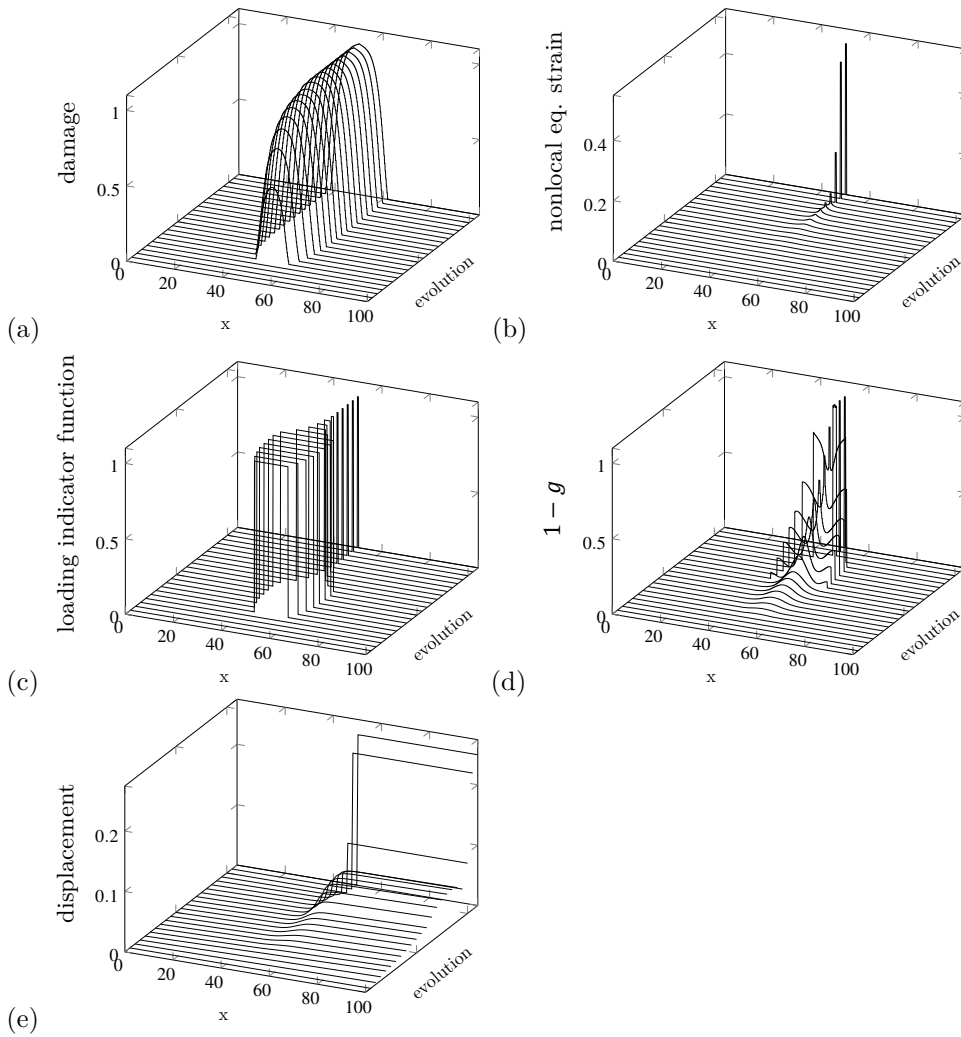
Figure 2.16: Evolution of (a) damage, (b) nonlocal equivalent strain, (c) loading indicator function, (d) $1 - g$ and (e) horizontal displacement using a transient activity function $g_{\tilde{e}}$ with 400 elements. Evolution axis is up to 0.25 mm.

2.4.5. Transient activity function based on an equivalent dissipation with the strain-based model

Figure 2.17 shows a mesh-sensitivity study using the $g_{\tilde{u}}$ function. The results are mesh independent. It means the dissipation tends to a non-zero value. The evolutions of damage, nonlocal equivalent strain, loading indicator function, transient activity function and horizontal displacement with 400 elements are plotted in Figure 2.18a, b, c, d and e respectively. The loading indicator function in Figure 2.18c shows no damage spreading.
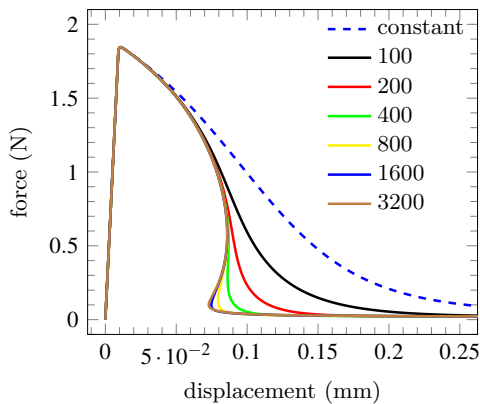
Figure 2.17: Mesh sensitivity study using a transient activity function $g_{\tilde{u}}$. The case with dashed blue line corresponds to the converged solution of the model with a constant gradient activity parameter obtained using 1600 elements.
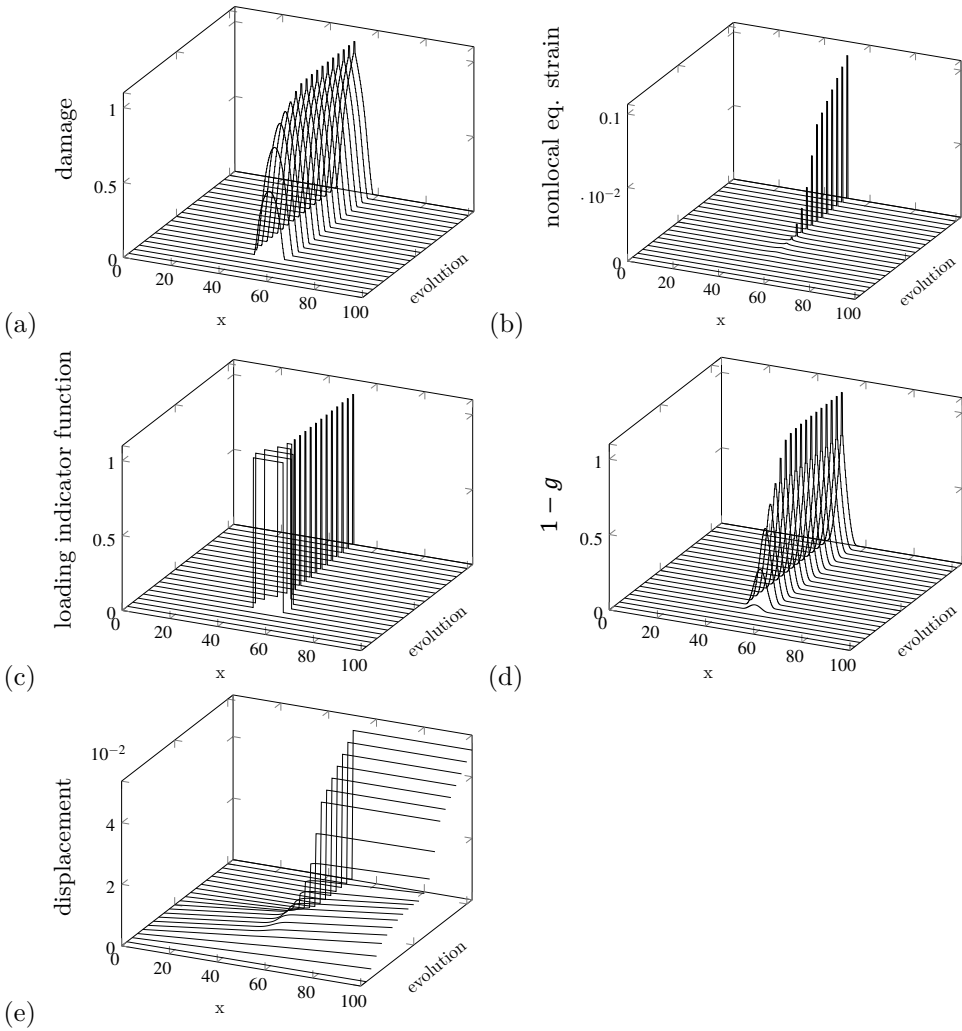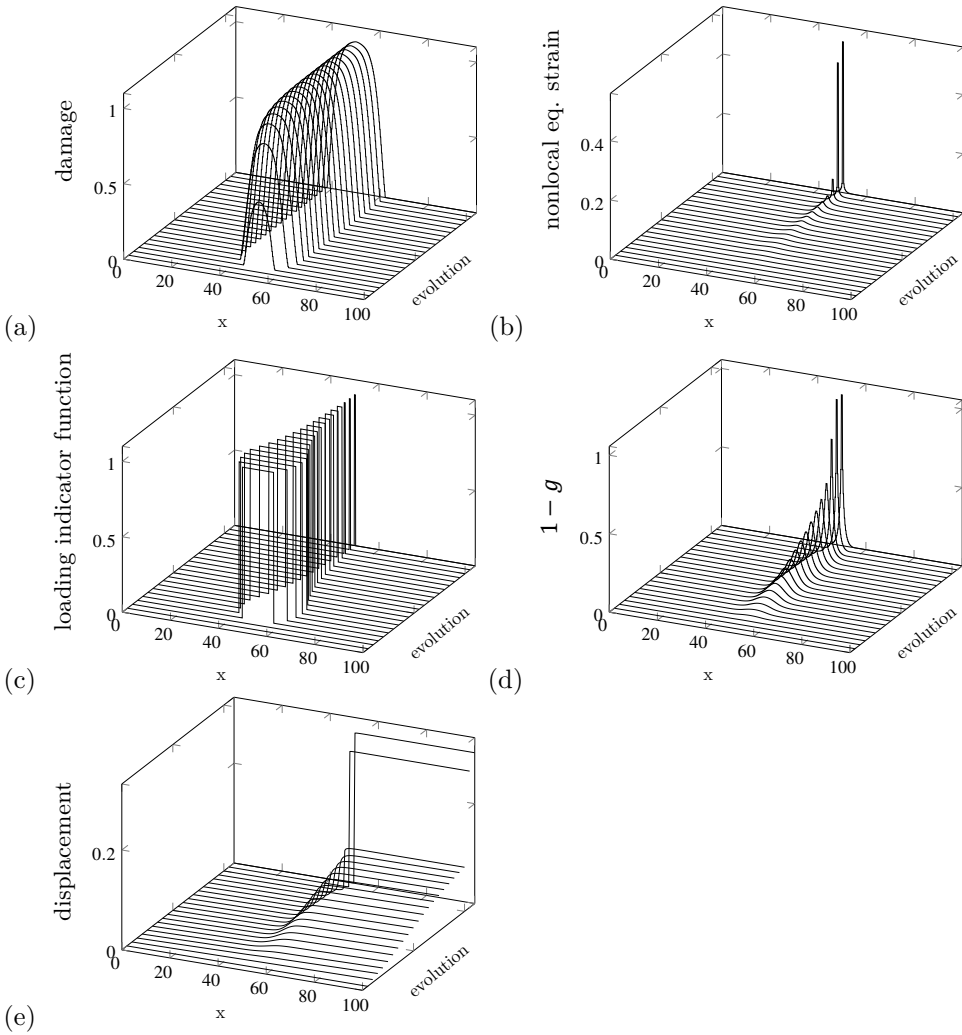
Figure 2.18: Evolution of (a) damage, (b) nonlocal equivalent strain, (c) loading indicator function, (d) $1-g$ and (e) horizontal displacement using a transient activity function $g_{\tilde{u}}$ with 400 elements. Evolution axis is up to 0.25 mm.

2.5. Conclusions

A displacement-based gradient enhanced damage model equipped with a transient activity function solves the problem of incorrect damage widening in a one dimensional setting, bridging damage and fracture mechanics for quasi-brittle failure. The model can appropriately describe the discontinuous nature of the displacement field at final stages of failure. Hence, the problem of spurious damage growth in the original displacement-based GEDM is eliminated. Here, we relied on a one-dimensional situation to derive the transient activity functions. Among the fifteen transient activity functions that have been tested, four functions were selected for this chapter. We have observed that not all transient activity functions are suitable. Those with fast decays to zero for instance give rise to mesh-dependency.

References

[1] M. Geers, R. de Borst, W. Brekelmans, and R. Peerlings, Strain-based transient-gradient damage model for failure analyses, Computer Methods in Applied Mechanics and Engineering 160, 133 (1998).

[2] A. Simone, H. Askes, and L. J. Sluys, Incorrect initiation and propagation of failure in non-local and gradient-enhanced media, International Journal of Solids and Structures 41, 351 (2004).

[3] B. Vandoren and A. Simone, Modeling and simulation of quasi-brittle failure with continuous anisotropic stress-based gradient-enhanced damage models, Computer Methods in Applied Mechanics and Engineering 332, 644 (2018).

[4] R. Peerlings, R. R. de Borst, W. Brekelmans, and J. de Vree, Gradient enhanced damage for quasi-brittle materials, International Journal for Numerical Methods in Engineering 39, 3391 (1996).

[5] G. Pijaudier-Cabot and Z. P. Bažant, Nonlocal damage theory, Journal of engineering mechanics 113, 1512 (1987).

[6] A. Simone, G. N. Wells, and L. J. Sluys, From continuous to discontinuous failure in a gradient-enhanced continuum damage model, Computer Methods in Applied Mechanics and Engineering 192, 4581 (2003).

[7] S. Saroukhani, R. Vafadari, and A. Simone, A simplified implementation of a gradient-enhanced damage model with transient length scale effects, Computational Mechanics 51, 899 (2013).

[8] L. H. Poh and G. Sun, Localizing gradient damage model with decreasing interactions, International Journal for Numerical Methods in Engineering 110, 503 (2017).

[9] J.-Y. Wu, A geometrically regularized gradient-damage model with energetic equivalence, Computer Methods in Applied Mechanics and Engineering 328, 612 (2018).

[10] T. H. A. Nguyen, T. Q. Bui, and S. Hirose, Smoothing gradient damage model with evolving anisotropic nonlocal interactions tailored to low-order finite elements, Computer Methods in Applied Mechanics and Engineering 328, 498 (2018).

[11] A. Rodríguez-Ferran, I. Morata, and A. Huerta, A new damage model based on non-local displacements, International Journal for numerical and analytical methods in geomechanics 29, 473 (2005).

3

Transient displacement-based GEDM: Two-dimensional study

In this chapter, a transient length-scale extension of the displacement-based gradient-enhanced isotropic damage model for two-dimensional problems is proposed. Model formulation and implementation are thoroughly discussed, and its regularization capabilities are compared to those of the corresponding constant length-scale version in classical benchmark problems. Despite the existence of spurious damage growth in mode-I failure, in mode-II failure realistic damage initiation, growth and propagation are guaranteed.

3.1. Introduction

As outlined in Section 2.1, there is a need to develop a transient displacement-based GEDM in order to deal with incorrect damage widening and migration issues.

Throughout this chapter, we will be focusing on answering the following question:

Would it be possible to use the transient activity function that has been formulated and used as part of the previous chapter in a one-dimensional setting in order to eliminate the spurious damage growth in a two-dimensional setting as well?

To answer this question, it is necessary to investigate the difference between one- and two-dimensional damage regularization approaches. We believe that there is currently no reliable continuous damage model without damages spreading and migration issues in higher dimensions that can provide mesh-independent results when the length scale tends to zero. This is considered to be one of the major limitations associated with the continuous damage theory, and one that cannot be ignored.

The purpose of this chapter is to present some preliminary steps toward developing a reliable continuous damage model that does not suffer from problems associated with damage widening and migration issues in higher dimensions. This highlights the necessity of investigating the fidelity of the proposed transient activity functions in the previous chapter in a two-dimensional setting. For this purpose, two-dimensional studies have been conducted using the transient activity function $g_{\tilde{u}}$ that was proposed in Section 2.3.4 for the one-dimensional case. The performance of the proposed model in two-dimensional problems will be evaluated based on its ability to eliminate spurious damage widening and damage migration in mode-I and mode-II failure mechanisms.

This chapter is organized as follows: Section 3.2 contains the governing equations of the displacement-based GEDM with transient length scale for two-dimensional problems. Section 3.3 presents the results of the two-dimensional displacement-based GEDM equipped with the transient length scale defined in Section 2.3. We conclude this chapter in Section 3.4 with some comments about the pros and cons of the proposed model.

3.2. Governing equations and discretization

3.2.1. Strong-form equations and boundary conditions

A two-dimensional displacement-based gradient-enhanced damage model with transient activity is formulated by a system of coupled differential equations expressed in terms of the classical equilibrium equation and a diffusion equation as

$$\nabla^s \cdot \boldsymbol{\sigma} + \mathbf{b} = \mathbf{0}, \quad \text{in} \quad \Omega, \tag{3.1}$$

$$\tilde{\mathbf{u}} - \nabla \cdot (gc\nabla\tilde{\mathbf{u}}) = \mathbf{u}, \quad \text{in} \quad \Omega, \tag{3.2}$$

subject to Dirichlet and Neumann boundary conditions applied on the local displacement field $\mathbf{u}$ and its gradient as

$$\mathbf{u} = \overline{\mathbf{u}}, \qquad \text{on} \quad \Gamma_{\overline{\mathbf{u}}}, \tag{3.3}$$

$$\boldsymbol{\sigma}\underline{\mathbf{n}} = \overline{\mathbf{t}}, \qquad \text{on} \quad \Gamma_{\overline{\mathbf{t}}}, \tag{3.4}$$

and the following Dirichlet type and non-homogeneous Neumann boundary conditions applied on the nonlocal displacement field $\tilde{\mathbf{u}}$ and its gradient

$$\tilde{\mathbf{u}} \cdot \underline{\mathbf{n}} = \mathbf{u} \cdot \underline{\mathbf{n}}, \qquad \text{on} \quad \Gamma, \tag{3.5}$$

$$\underline{\mathbf{n}} \cdot \nabla\tilde{\mathbf{u}} \cdot \mathbf{t} = \underline{\mathbf{n}} \cdot \nabla\mathbf{u} \cdot \mathbf{t}, \qquad \text{on} \quad \Gamma, \tag{3.6}$$

where boundary $\Gamma = \Gamma_{\overline{\mathbf{u}}} \cup \Gamma_{\overline{\mathbf{t}}}$ and $\Gamma_{\overline{\mathbf{u}}} \cap \Gamma_{\overline{\mathbf{t}}} = \oslash$ in which $\overline{\mathbf{u}}$ and $\overline{\mathbf{t}}$ are the prescribed local displacement and traction vectors applied on boundaries $\Gamma_{\overline{\mathbf{u}}}$ and $\Gamma_{\overline{\mathbf{t}}}$, respectively, and $\boldsymbol{\sigma}$ and $\mathbf{b}$ are the stress tensor and the body forces vector, respectively. The unit outward normal and tangent vectors on the boundary Γ are defined by $\underline{\mathbf{n}} = \left[\underline{n}_x, \underline{n}_y\right]^{\mathrm{T}}$ and $\overline{\mathbf{t}} = \left[\overline{t}_x, \overline{t}_y\right]^{\mathrm{T}}$, respectively and ∇^s and ∇ are the gradient operators applied on the local and nonlocal displacement fields , respectively and defined as

$$\nabla^s = \begin{bmatrix} \frac{\partial}{\partial x} & 0 \\ 0 & \frac{\partial}{\partial y} \\ \frac{\partial}{\partial y} & \frac{\partial}{\partial x} \end{bmatrix}, \qquad \nabla = \begin{bmatrix} \frac{\partial}{\partial x} & 0 \\ \frac{\partial}{\partial y} & 0 \\ 0 & \frac{\partial}{\partial x} \\ 0 & \frac{\partial}{\partial y} \end{bmatrix}. \tag{3.7}$$

The parameters g and c control the active nonlocal interactions between microcracks in which g is a transient activity function and $c = \ell_0^2$ is a constant gradient activity parameter. Details regarding the weak formulation and the definition of the discrete governing equations are discussed next.

3.2.2. Weak formulation

The weighted residual approach is used to obtain the weak-form of the governing equations. To this end, the governing strong-form equations, Equations (3.1) and (3.2), are multiplied by the vectorial functions $\mathbf{w}$ and $\tilde{\mathbf{w}}$, respectively. The resulting equations are then integrated over problem domain Ω yielding

$$\int_{\Omega} [\mathbf{w} \cdot (\nabla^s \cdot \boldsymbol{\sigma} + \mathbf{b})] \, \mathrm{d}\Omega = 0, \tag{3.8}$$

$$\int_{\Omega} [\tilde{\mathbf{w}} \cdot (\tilde{\mathbf{u}} - \nabla \cdot (gc\nabla\tilde{\mathbf{u}}))] \, \mathrm{d}\Omega = \int_{\Omega} [\tilde{\mathbf{w}} \cdot \mathbf{u}] \, \mathrm{d}\Omega. \tag{3.9}$$

Using the identities

$$\mathbf{w} \cdot (\nabla^s \cdot \boldsymbol{\sigma}) = \nabla^s \cdot (\mathbf{w} \cdot \boldsymbol{\sigma}) - \nabla^s \mathbf{w} : \boldsymbol{\sigma}, \tag{3.10}$$

$$\tilde{\mathbf{w}} \cdot [\nabla \cdot (gc\nabla\tilde{\mathbf{u}})] = \nabla \cdot (\tilde{\mathbf{w}} \cdot gc\nabla\tilde{\mathbf{u}}) - \nabla\tilde{\mathbf{w}} : g\,c\nabla\tilde{\mathbf{u}}, \tag{3.11}$$

and

$$\int_{\Omega} [\nabla \cdot (\tilde{\mathbf{w}} \cdot gc\nabla\tilde{\mathbf{u}})] \, \mathrm{d}\Omega = \int_{\Gamma} \left[\tilde{\mathbf{w}} \cdot (gc\nabla\tilde{\mathbf{u}} \cdot \underline{\mathbf{n}}) \right] \mathrm{d}\Gamma, \tag{3.12}$$

$$\int_{\Omega} [\nabla^s \cdot (\mathbf{w} \cdot \boldsymbol{\sigma})] \, \mathrm{d}\Omega = \int_{\Gamma_{\bar{\mathbf{t}}}} \left[\mathbf{w} \cdot (\boldsymbol{\sigma} \cdot \underline{\mathbf{n}}) \right] \mathrm{d}\Gamma = \int_{\Gamma_{\bar{\mathbf{t}}}} \left[\mathbf{w} \cdot \bar{\mathbf{t}} \right] \mathrm{d}\Gamma, \tag{3.13}$$

and substituting them into Equations (3.8) and (3.9) lead to

$$\int_{\Omega} [\nabla^s \mathbf{w} : \boldsymbol{\sigma}] \, \mathrm{d}\Omega = \int_{\Omega} [\mathbf{w} \cdot \mathbf{b}] \, \mathrm{d}\Omega + \int_{\Gamma_{\bar{\mathbf{t}}}} \left[\mathbf{w} \cdot \bar{\mathbf{t}} \right] \mathrm{d}\Gamma, \tag{3.14}$$

$$\int_{\Omega} [\tilde{\mathbf{w}}\tilde{\mathbf{u}} + \nabla\tilde{\mathbf{w}} : g\,c\nabla\tilde{\mathbf{u}} - \tilde{\mathbf{w}}\mathbf{u}] \, \mathrm{d}\Omega = \int_{\Gamma} \left[\tilde{\mathbf{w}} \cdot \left(gc\nabla\tilde{\mathbf{u}} \cdot \underline{\mathbf{n}} \right) \right] \mathrm{d}\Gamma. \tag{3.15}$$

To apply the non-homogeneous Neumann boundary condition (the right-hand side of Equation (3.15)), we can decompose $\tilde{\mathbf{w}}$ as an arbitrary function in the form of $\tilde{\mathbf{w}} = (\tilde{\mathbf{w}} \cdot \mathbf{t}) \cdot \mathbf{t} + (\tilde{\mathbf{w}} \cdot \underline{\mathbf{n}}) \cdot \underline{\mathbf{n}}$ such that $\tilde{\mathbf{w}} \cdot \underline{\mathbf{n}} = 0$ leads to the final weak-form of the governing equations as

$$\int_{\Omega} [\nabla^s \mathbf{w} : \boldsymbol{\sigma}] \, \mathrm{d}\Omega = \int_{\Omega} [\mathbf{w} \cdot \mathbf{b}] \, \mathrm{d}\Omega + \int_{\Gamma_{\bar{\mathbf{t}}}} \left[\mathbf{w} \cdot \bar{\mathbf{t}} \right] \mathrm{d}\Gamma, \tag{3.16}$$

$$\int_{\Omega} [\tilde{\mathbf{w}}\tilde{\mathbf{u}} + \nabla\tilde{\mathbf{w}} : g\,c\nabla\tilde{\mathbf{u}} - \tilde{\mathbf{w}}\mathbf{u}] \, \mathrm{d}\Omega = \int_{\Gamma} \left[(\tilde{\mathbf{w}} \cdot \mathbf{t}) \cdot \mathbf{t} \cdot \left(gc\nabla\tilde{\mathbf{u}} \cdot \underline{\mathbf{n}} \right) \right] \mathrm{d}\Gamma. \tag{3.17}$$

3.2.3. Finite element discretization

The Bubnov-Galerkin method is employed for the discretization of the weak-form of the governing equations. To this end, the local and nonlocal displacement fields, along with the corresponding weight functions, are discretized at the element level as follows:

$$\mathbf{u} = \mathbf{N}\mathbf{u}^h, \quad \mathbf{w_u} = \mathbf{N}\mathbf{w}_\mathbf{u}^h, \quad \nabla^s\mathbf{u} = \nabla^s\mathbf{N}\mathbf{u}^h, \quad \nabla^s\mathbf{w_u} = \nabla^s\mathbf{N}\mathbf{w}_\mathbf{u}^h, \tag{3.18}$$

$$\tilde{\mathbf{u}} = \mathbf{N}\tilde{\mathbf{u}}^h, \quad \mathbf{w}_{\tilde{\mathbf{u}}} = \mathbf{N}\mathbf{w}_{\tilde{\mathbf{u}}}^h, \quad \nabla\tilde{\mathbf{u}} = \nabla\mathbf{N}\tilde{\mathbf{u}}^h, \quad \nabla\mathbf{w}_{\tilde{\mathbf{u}}} = \nabla\mathbf{N}\mathbf{w}_{\tilde{\mathbf{u}}}^h, \tag{3.19}$$

in which the same shape function matrix, $\mathbf{N}$, is employed to interpolate displacement fields, $\mathbf{u}$ and $\tilde{\mathbf{u}}$, and the weight functions, $\mathbf{w_u}$ and $\mathbf{w}_{\tilde{\mathbf{u}}}$. Inserting the above relations into the final weak form (Equations (3.16) and (3.17)) and expressing the stress and strain tensors in their vector form yield

$$\sum_p \mathbf{w}_\mathbf{u}^{h\,\mathrm{T}} \nabla^s \mathbf{N}^\mathrm{T} \boldsymbol{\sigma}_p \mathrm{d}v_p = \sum_p \mathbf{w}_\mathbf{u}^{h\,\mathrm{T}} \mathbf{N}^\mathrm{T} \mathbf{b}_p \mathrm{d}v_p + \int_{\Gamma_{\bar{\mathbf{t}}}} \mathbf{w}_\mathbf{u}^{h\,\mathrm{T}} \mathbf{N}^\mathrm{T}\bar{\mathbf{t}}_p \mathrm{d}\Gamma, \tag{3.20}$$

$$\sum_p \left[\mathbf{w}_{\tilde{\mathbf{u}}}^{h\,\mathrm{T}} \mathbf{N}^\mathrm{T}\mathbf{N}\tilde{\mathbf{u}}^h + \mathbf{w}_{\tilde{\mathbf{u}}}^{h\,\mathrm{T}} \nabla\mathbf{N}^\mathrm{T} g_p c \nabla \mathbf{N}\tilde{\mathbf{u}}^h - \mathbf{w}_{\tilde{\mathbf{u}}}^{h\,\mathrm{T}}\mathbf{N}^\mathrm{T}\mathbf{N}\mathbf{u}^h \right]\mathrm{d}v_p =$$
$$\sum_p \left[\left(\mathbf{w}_{\tilde{\mathbf{u}}}^{h\,\mathrm{T}}\mathbf{N}_p^\mathrm{T} \cdot \mathbf{t}_p \right) \cdot \mathbf{t}_p \cdot \left(g_p c \nabla \mathbf{N}\tilde{\mathbf{u}}^h \cdot \underline{\mathbf{n}}_p \right) \right]\mathrm{d}\Gamma_p, \tag{3.21}$$

which have to hold for any choice of $\mathbf{w_u}$ and $\mathbf{w}_{\tilde{\mathbf{u}}}$. By removing $\mathbf{w_u}$ and $\mathbf{w}_{\tilde{\mathbf{u}}}$ from both sides of the equations results in

$$\sum_p \nabla^s \mathbf{N}^\mathrm{T} \boldsymbol{\sigma}_p \mathrm{d}v_p = \sum_p \mathbf{N}^\mathrm{T} \mathbf{b}_p \mathrm{d}v_p + \int_{\Gamma_{\bar{\mathbf{t}}}} \mathbf{N}^\mathrm{T}\bar{\mathbf{t}}_p \mathrm{d}\Gamma, \tag{3.22}$$

$$\sum_p \left[\mathbf{N}^\mathrm{T}\mathbf{N}\tilde{\mathbf{u}}^h + \nabla\mathbf{N}^\mathrm{T} g_p c \nabla \mathbf{N}\tilde{\mathbf{u}}^h - \mathbf{N}^\mathrm{T}\mathbf{N}\mathbf{u}^h \right]\mathrm{d}v_p =$$
$$\sum_p \left[\left(\mathbf{N}_p^\mathrm{T} \cdot \mathbf{t}_p \right) \cdot \mathbf{t}_p \cdot \left(g_p c \nabla \mathbf{N}\tilde{\mathbf{u}}^h \cdot \underline{\mathbf{n}}_p \right) \right]\mathrm{d}\Gamma_p. \tag{3.23}$$

Now, by defining $\mathbf{M}$ and $\mathbf{D}$ as the mass-like and diffusivity matrices

$$\mathbf{M} \;=\; \sum_p \mathbf{N}^\mathrm{T}\mathbf{N}\mathrm{d}v_p, \tag{3.24}$$

$$\mathbf{D} \;=\; \sum_p \nabla\mathbf{N}^\mathrm{T} g_p c \nabla\mathbf{N}\mathrm{d}v_p, \tag{3.25}$$

and the matrix

$$\mathbf{K}_{\partial\Omega} = \sum_p \left[\left(\mathbf{N}_p^{\mathrm{T}} \cdot \mathbf{t}_p\right) \cdot \mathbf{t}_p \cdot \left(g_p c \nabla \mathbf{N} \cdot \underline{\mathbf{n}}_p\right)\right] \mathrm{d}\Gamma_p, \tag{3.26}$$

that can be written as

$$\mathbf{K}_{\partial\Omega} = \sum_p \left[\mathbf{N}_p^{\mathrm{T}} \mathbf{a}_p g_p c \nabla \mathbf{N}\right] \mathrm{d}\Gamma_p, \tag{3.27}$$

with

$$\mathbf{a}_p = \left[\begin{array}{cccc} n_x t_x^2 & n_y t_x^2 & n_x t_x t_y & n_y t_x t_y \\ n_x t_x t_y & n_y t_x t_y & n_x t_y^2 & n_y t_y^2 \end{array}\right], \tag{3.28}$$

the discretized form of the governing equations is expressed as

$$\sum_p \nabla^s \mathbf{N}^{\mathrm{T}} \boldsymbol{\sigma}_p \mathrm{d}v_p = \sum_p \mathbf{N}^{\mathrm{T}} \mathbf{b}_p \mathrm{d}v_p + \int_{\Gamma_{\bar{\mathbf{t}}}} \mathbf{N}^{\mathrm{T}} \bar{\mathbf{t}}_p \mathrm{d}\Gamma, \tag{3.29}$$

$$\mathbf{M}\tilde{\mathbf{u}}^h + \mathbf{D}\tilde{\mathbf{u}}^h - \mathbf{M}\mathbf{u}^h - \mathbf{K}_{\partial\Omega}\mathbf{u}^h = \mathbf{0}. \tag{3.30}$$

Finally, the discretized governing equations are rewritten in terms of external and internal nodal forces according to

$$\mathbf{f}_{\mathrm{int}}^{\mathbf{u}} = \mathbf{f}_{\mathrm{ext}}^{\mathbf{u}}, \tag{3.31}$$

$$\mathbf{f}_{\mathrm{int}}^{\tilde{\mathbf{u}}} = \mathbf{f}_{\mathrm{ext}}^{\tilde{\mathbf{u}}}, \tag{3.32}$$

in which

$$\mathbf{f}_{\mathrm{int}}^{\mathbf{u}} = \sum_p \nabla^s \mathbf{N}^{\mathrm{T}} \boldsymbol{\sigma}_p \mathrm{d}v_p, \tag{3.33}$$

$$\mathbf{f}_{\mathrm{ext}}^{\mathbf{u}} = \sum_p \mathbf{N}^{\mathrm{T}} \mathbf{b}_p \mathrm{d}v_p + \int_{\Gamma_{\bar{\mathbf{t}}}} \mathbf{N}^{\mathrm{T}} \bar{\mathbf{t}}_p \mathrm{d}\Gamma, \tag{3.34}$$

$$\mathbf{f}_{\mathrm{int}}^{\tilde{\mathbf{u}}} = \mathbf{M}\tilde{\mathbf{u}}^h + \mathbf{D}\tilde{\mathbf{u}}^h - \mathbf{M}\mathbf{u}^h - \mathbf{K}_{\partial\Omega}\mathbf{u}^h, \tag{3.35}$$

$$\mathbf{f}_{\mathrm{ext}}^{\tilde{\mathbf{u}}} = \mathbf{0}. \tag{3.36}$$

3.2.4. Consistent linearization

A consistent tangent stiffness is obtained by linearization of Equations (3.31) and (3.32) at iteration $i+1$ with respect to the previous iteration i. Accordingly,

$$\mathbf{f}_{\mathrm{ext},i+1}^{\mathbf{u}} = \mathbf{f}_{\mathrm{int},i}^{\mathbf{u}} + \delta\mathbf{f}_{\mathrm{int},i+1}^{\mathbf{u}}, \tag{3.37}$$

$$\mathbf{f}_{\mathrm{ext},i+1}^{\tilde{\mathbf{u}}} = \mathbf{f}_{\mathrm{int},i}^{\tilde{\mathbf{u}}} + \delta\mathbf{f}_{\mathrm{int},i+1}^{\tilde{\mathbf{u}}}, \tag{3.38}$$

gives

$$\delta \mathbf{f}^{\mathbf{u}}_{\text{int},i+1} \;=\; \mathbf{f}^{\mathbf{u}}_{\text{ext},i+1} - \mathbf{f}^{\mathbf{u}}_{\text{int},i}, \tag{3.39}$$

$$\delta \mathbf{f}^{\tilde{\mathbf{u}}}_{\text{int},i+1} \;=\; \mathbf{f}^{\tilde{\mathbf{u}}}_{\text{ext},i+1} - \mathbf{f}^{\tilde{\mathbf{u}}}_{\text{int},i}, \tag{3.40}$$

where

$$\delta \mathbf{f}^{\mathbf{u}}_{\text{int},i+1} \;=\; \sum_p \left[\nabla^s \mathbf{N}^{\mathrm{T}} \delta \boldsymbol{\sigma}_{p,i+1} \right] \mathrm{d}v_p, \tag{3.41}$$

$$\delta \mathbf{f}^{\tilde{\mathbf{u}}}_{\text{int},i+1} \;=\; \mathbf{M}\delta \tilde{\mathbf{u}}^h_{i+1} - \mathbf{M}\delta \mathbf{u}^h_{i+1} + \mathbf{D}\delta \tilde{\mathbf{u}}^h_{i+1}$$

$$+ \;\; \delta \mathbf{D}_{i+1}\tilde{\mathbf{u}}^h - \mathbf{K}_{\partial\Omega}\delta \mathbf{u}^h_{i+1} - \delta \mathbf{K}_{\partial\Omega_{i+1}}\mathbf{u}^h. \tag{3.42}$$

To obtain the stress variation, $\delta\boldsymbol{\sigma}_{i+1}$, we assume the free energy density potential function

$$\psi = \frac{1}{2}(1-\omega)\,\boldsymbol{\epsilon} : \boldsymbol{\mathcal{C}} : \boldsymbol{\epsilon}, \tag{3.43}$$

which leads to the expressions of the stress tensor and its derivative:

$$\boldsymbol{\sigma} = \frac{\partial \psi}{\partial \boldsymbol{\epsilon}} = (1-\omega)\,\boldsymbol{\mathcal{C}} : \boldsymbol{\epsilon}, \tag{3.44}$$

$$\delta\boldsymbol{\sigma}_{i+1} = (1-\omega_i)\,\boldsymbol{\mathcal{C}}\delta\boldsymbol{\epsilon}_{i+1} - \boldsymbol{\mathcal{C}}\boldsymbol{\epsilon}_i\delta\omega_{i+1}, \tag{3.45}$$

with $\boldsymbol{\mathcal{C}}$ the fourth order elastic moduli tensor and

$$\delta\boldsymbol{\epsilon}_{i+1} = \nabla^s \mathbf{N}\delta\mathbf{u}^h_{i+1}, \qquad \delta\tilde{\boldsymbol{\epsilon}}_{i+1} = \nabla^s \mathbf{N}\delta\tilde{\mathbf{u}}^h_{i+1}, \tag{3.46}$$

$$\delta\omega_{i+1} = \left(\frac{\partial\omega}{\partial\tilde{\boldsymbol{\epsilon}}}\right)_i \delta\tilde{\boldsymbol{\epsilon}}_{i+1} = \left(\frac{\partial\omega}{\partial\kappa}\right)_i \left(\frac{\partial\tilde{e}}{\partial\tilde{\boldsymbol{\epsilon}}}\right)_i \left(\frac{\partial\tilde{e}}{\partial\tilde{\boldsymbol{\epsilon}}}\right)_i \nabla^s \mathbf{N}\delta\tilde{\mathbf{u}}^h_{i+1}. \tag{3.47}$$

With these expressions, the stress increment is written as

$$\delta\boldsymbol{\sigma}_{i+1} = (1-\omega_i)\,\boldsymbol{\mathcal{C}}\nabla^s \mathbf{N}\delta\mathbf{u}^h_{i+1} - \boldsymbol{\mathcal{C}}\boldsymbol{\epsilon}_i\left(\frac{\partial\omega}{\partial\tilde{\boldsymbol{\epsilon}}}\right)_i \nabla^s \mathbf{N}\delta\tilde{\mathbf{u}}^h_{i+1}. \tag{3.48}$$

The matrices $\mathbf{D}$ and $\mathbf{K}_{\partial\Omega}$ are defined as a function of both $\mathbf{u}^h_{i+1}$ and $\tilde{\mathbf{u}}^h_{i+1}$. Hence, their linearizations give

$$\delta\mathbf{D}_{i+1} = \left(\frac{\partial\mathbf{D}}{\partial\mathbf{u}^h}\right)_i \delta\mathbf{u}^h_{i+1} + \left(\frac{\partial\mathbf{D}}{\partial\tilde{\mathbf{u}}^h}\right)_i \delta\tilde{\mathbf{u}}^h_{i+1}, \tag{3.49}$$

$$\delta\mathbf{K}_{\partial\Omega_{i+1}} = \left(\frac{\partial\mathbf{K}_{\partial\Omega}}{\partial\mathbf{u}^h}\right)_i \delta\mathbf{u}^h_{i+1} + \left(\frac{\partial\mathbf{K}_{\partial\Omega}}{\partial\tilde{\mathbf{u}}^h}\right)_i \delta\tilde{\mathbf{u}}^h_{i+1}. \tag{3.50}$$

Substitution of the above variations into Equations (3.41) and (3.42) leads to

$$\delta \mathbf{f}^{\mathbf{u}}_{\text{int},i+1} = \sum_p \left[\nabla^s \mathbf{N}^{\mathrm{T}} (1 - \omega_i)\, \mathcal{C} \nabla^s \mathbf{N} \right] \delta \mathbf{u}^h_{i+1} \mathrm{d}v_p -$$
$$\sum_p \left[\nabla^s \mathbf{N}^{\mathrm{T}} \mathcal{C} \boldsymbol{\epsilon}_i \left(\frac{\partial \omega}{\partial \tilde{\boldsymbol{\epsilon}}} \right) \nabla^s \mathbf{N} \right] \delta \tilde{\mathbf{u}}^h_{i+1} \mathrm{d}v_p, \tag{3.51}$$

$$\delta \mathbf{f}^{\tilde{\mathbf{u}}}_{\text{int},i+1} = \left[-\mathbf{M} - \mathbf{K}_{\partial\Omega} + \frac{\partial \mathbf{D}}{\partial \mathbf{u}^h} \tilde{\mathbf{u}}^h - \frac{\partial \mathbf{K}_{\partial\Omega}}{\partial \mathbf{u}^h} \mathbf{u}^h \right] \delta \mathbf{u}^h_{i+1} +$$
$$\left[\mathbf{M} + \mathbf{D} + \frac{\partial \mathbf{D}}{\partial \tilde{\mathbf{u}}^h} \tilde{\mathbf{u}}^h - \frac{\partial \mathbf{K}_{\partial\Omega}}{\partial \tilde{\mathbf{u}}^h} \mathbf{u}^h \right] \delta \tilde{\mathbf{u}}^h_{i+1}. \tag{3.52}$$

Finally, the discretized governing equations at a Newton-Raphson iteration read

$$\underbrace{\begin{bmatrix} \mathbf{K}^i_{\mathbf{u}\mathbf{u}} & \mathbf{K}^i_{\mathbf{u}\tilde{\mathbf{u}}} \\ \mathbf{K}^i_{\tilde{\mathbf{u}}\mathbf{u}} & \mathbf{K}^i_{\tilde{\mathbf{u}}\tilde{\mathbf{u}}} \end{bmatrix}}_{16 \times 16} \underbrace{\begin{bmatrix} \delta \mathbf{u}^{i+1} \\ \delta \tilde{\mathbf{u}}^{i+1} \end{bmatrix}}_{16 \times 1} = \underbrace{\begin{bmatrix} \mathbf{f}^{\mathbf{u}}_{\text{ext},i+1} - \mathbf{f}^{\mathbf{u}}_{\text{int},i} \\ -\mathbf{f}^{\tilde{\mathbf{u}}}_{\text{int},i} \end{bmatrix}}_{16 \times 1}, \tag{3.53}$$

with components

$$\underbrace{\mathbf{K}^i_{\mathbf{u}\mathbf{u}}}_{8 \times 8} = \sum_p \left[\underbrace{\nabla^s \mathbf{N}^{\mathrm{T}}}_{8 \times 3} \underbrace{(1 - \omega_i)}_{\text{scalar}} \underbrace{\mathcal{C}}_{3 \times 3} \underbrace{\nabla^s \mathbf{N}}_{3 \times 8} \right] \mathrm{d}v_p, \tag{3.54}$$

$$\underbrace{\mathbf{K}^i_{\mathbf{u}\tilde{\mathbf{u}}}}_{8 \times 8} = \sum_p \left[-\underbrace{\nabla^s \mathbf{N}^{\mathrm{T}}}_{8 \times 3} \underbrace{\mathcal{C}}_{3 \times 3} \underbrace{\boldsymbol{\epsilon}_i}_{3 \times 1} \underbrace{\left(\frac{\partial \omega}{\partial \tilde{\boldsymbol{\epsilon}}} \right)_i}_{1 \times 3} \underbrace{\nabla^s \mathbf{N}}_{3 \times 8} \right] \mathrm{d}v_p, \tag{3.55}$$

$$\underbrace{\mathbf{K}^i_{\tilde{\mathbf{u}}\mathbf{u}}}_{8 \times 8} = -\underbrace{\mathbf{M}}_{8 \times 8} - \underbrace{\mathbf{K}_{\partial\Omega}}_{8 \times 8} + \underbrace{\frac{\partial \mathbf{D}}{\partial \mathbf{u}^h}}_{8 \times 1} \underbrace{\tilde{\mathbf{u}}^h}_{1 \times 8} - \underbrace{\frac{\partial \mathbf{K}_{\partial\Omega}}{\partial \mathbf{u}^h}}_{8 \times 1} \underbrace{\mathbf{u}^h}_{1 \times 8}, \tag{3.56}$$

$$\underbrace{\mathbf{K}^i_{\tilde{\mathbf{u}}\tilde{\mathbf{u}}}}_{8 \times 8} = \underbrace{\mathbf{M}}_{8 \times 8} + \underbrace{\mathbf{D}}_{8 \times 8} + \underbrace{\frac{\partial \mathbf{D}}{\partial \tilde{\mathbf{u}}^h}}_{8 \times 1} \underbrace{\tilde{\mathbf{u}}^h}_{1 \times 8} - \underbrace{\frac{\partial \mathbf{K}_{\partial\Omega}}{\partial \tilde{\mathbf{u}}^h}}_{8 \times 1} \underbrace{\mathbf{u}^h}_{1 \times 8}, \tag{3.57}$$

in which

$$\underbrace{\frac{\partial \mathbf{D}}{\partial \mathbf{u}^h} \tilde{\mathbf{u}}^h}_{8\times 8} \;=\; \sum_p \left[\underbrace{\frac{\partial g_p}{\partial \mathbf{u}^h}}_{1\times 8} \underbrace{\tilde{\mathbf{u}}^h}_{8\times 1} \underbrace{\nabla \mathbf{N}^\mathrm{T}}_{8\times 4} \underbrace{c}_{\mathrm{scalar}} \underbrace{\nabla \mathbf{N}}_{4\times 8} \right] \mathrm{d}v_p, \tag{3.58}$$

$$\underbrace{\frac{\partial \mathbf{D}}{\partial \tilde{\mathbf{u}}^h} \tilde{\mathbf{u}}^h}_{8\times 8} \;=\; \sum_p \left[\underbrace{\frac{\partial g_p}{\partial \tilde{\mathbf{u}}^h}}_{1\times 8} \underbrace{\tilde{\mathbf{u}}^h}_{8\times 1} \underbrace{\nabla \mathbf{N}^\mathrm{T}}_{8\times 4} \underbrace{c}_{\mathrm{scalar}} \underbrace{\nabla \mathbf{N}}_{4\times 8} \right] \mathrm{d}v_p, \tag{3.59}$$

$$\underbrace{\frac{\partial \mathbf{K}_{\partial\Omega}}{\partial \mathbf{u}^h} \mathbf{u}^h}_{8\times 8} \;=\; \sum_p \left[\underbrace{\frac{\partial g_p}{\partial \mathbf{u}^h}}_{1\times 8} \underbrace{\mathbf{u}^h}_{8\times 1} \underbrace{\mathbf{N}^\mathrm{T}}_{8\times 2} \underbrace{\mathbf{a}_p}_{2\times 4} \underbrace{c}_{\mathrm{scalar}} \underbrace{\nabla \mathbf{N}}_{4\times 8} \right] \mathrm{d}\Gamma_p, \tag{3.60}$$

$$\underbrace{\frac{\partial \mathbf{K}_{\partial\Omega}}{\partial \tilde{\mathbf{u}}^h} \mathbf{u}^h}_{8\times 8} \;=\; \sum_p \left[\underbrace{\frac{\partial g_p}{\partial \tilde{\mathbf{u}}^h}}_{1\times 8} \underbrace{\mathbf{u}^h}_{8\times 1} \underbrace{\mathbf{N}^\mathrm{T}}_{8\times 2} \underbrace{\mathbf{a}_p}_{2\times 4} \underbrace{c}_{\mathrm{scalar}} \underbrace{\nabla \mathbf{N}}_{4\times 8} \right] \mathrm{d}\Gamma_p, \tag{3.61}$$

where p is a material/integration point.

3.3. Results and discussions

In this section, the merit of the proposed transient displacement-based GEDM is demonstrated by means of two-dimensional benchmark examples. First, as a mode-I failure example, a four-point bending test is modeled and the results are compared against the displacement-based model with a constant internal length scale to show the efficiency of the proposed model for the removal of spurious damage growth. Then, the formation of shear bands under model-II failure is investigated on a plate with an imperfection. Finally, the performance of the model is evaluated through an L-shaped panel test in order to obtain a thin crack-like damage band. Both local and nonlocal displacement fields are simulated using quadrilateral linear (Q4) element types with full integration schemes. The modified von-Mises equivalent strain [1] is employed to calculate both local and nonlocal equivalent strains. It should be noted that the transient activity function $g_{\tilde{u}}$ that is proposed in Section 2.3.4 is employed.

3.3.1. Mode-I failure: a notched four-point concrete beam

A four-point bending beam specimen reported experimentally in [2] is considered. This example illustrates the performance of the proposed transient displacement-based GEDM for removing the incorrect damage widening in two-dimensional problems under mode-I failure. As shown in Figure 3.1a, a specimen with a vertical crack at the center of the bottom edge and with dimensions 500 mm × 100 mm with uniform thickness 50 mm under plane strain condition and simply supported with a span of 450 mm is investigated. Geometry and boundary conditions are also shown in Figure 3.1a. The vertically downward loads are applied at two points trisecting the span, and the vertical displacement at point A with an offset of 7.5 mm from the center-line of the beam is monitored. Due to the symmetry (symmetric geometry and boundary conditions), only half of the specimen is simulated as shown in Figure 3.1b. The numerical parameters and material properties are taken from [3] and are listed in Table 3.1.

Table 3.1: Four-point bending beam: material and damage parameters.

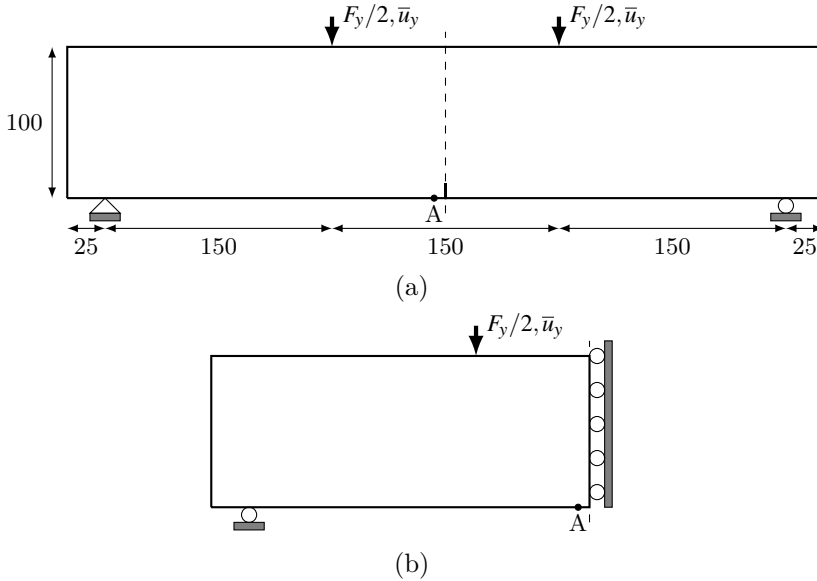|	symbol	value
Young's modulus	E	40×10^3 MPa
Poisson's ratio	ν	0.2
constant gradient activity parameter	c	4 mm^2
damage softening law	ω	exponential
damage threshold equivalent strain	κ_0	7.5×10^{-5}
softening parameter	β	300
residual parameter	α	0.92
compressive to tensile strength ratio	k	10

Figure 3.1: Four-point bending beam: geometry and boundary conditions for (a) full specimen and (b) half specimen (unit of length: mm).

For the mesh sensitivity study, four pre-refined mesh configurations with bilinear quadrilateral elements and with element sizes in the central part (damaged zone) of the beam equal to 2.5, 1.25, 0.625 and 0.3125 mm, respectively are generated using Gmsh [4]. The corresponding force-displacement curves are plotted in Figure 3.2 and compared to those obtained with the displacement-based model with a constant length scale. As shown in Figure 3.2, apart from a more brittle response of the proposed transient length scale model in comparison with the constant length scale model, the load-displacement curves show that the transient model is properly regularized and a mesh size equal to 1.25 mm, almost half of the length scale size, $\ell_0 = 2$ mm, is sufficient to guarantee an almost converged solution.

To investigate the efficiency of the proposed model in the removal of incorrect damage widening at high deformation level, the load was further increased compared to the level reached in Figure 3.2. The load-displacement curves with high deformation level for both transient and constant length scale models are reported in Figure 3.3. The damage, nonlocal equivalent strain, loading indicator function and g contours at snap-shot d (before starting the high deformation level) are compared in Figure 3.3. The corresponding contours at all indicated snap-shots in Figure 3.3 are compared in Figure 3.5. For plotting the contours of both Figures 3.4 and 3.5, the finest mesh configuration with element sizes 0.3125 mm is employed.
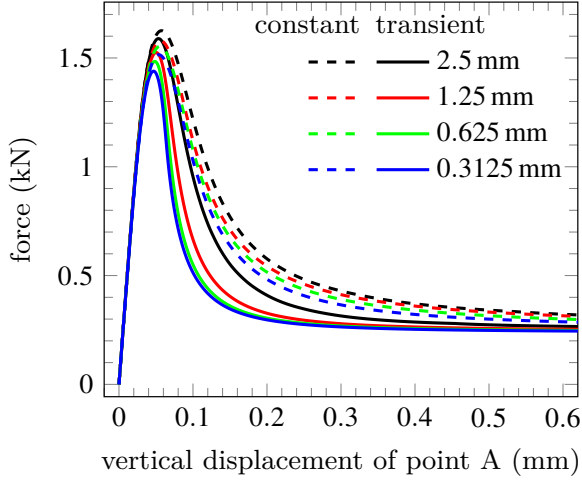
3

Figure 3.2: Four-point bending beam: a mesh-sensitivity study for the models with an evolving $g_{\tilde{u}}$ (solid) and a constant length scale (dashed).
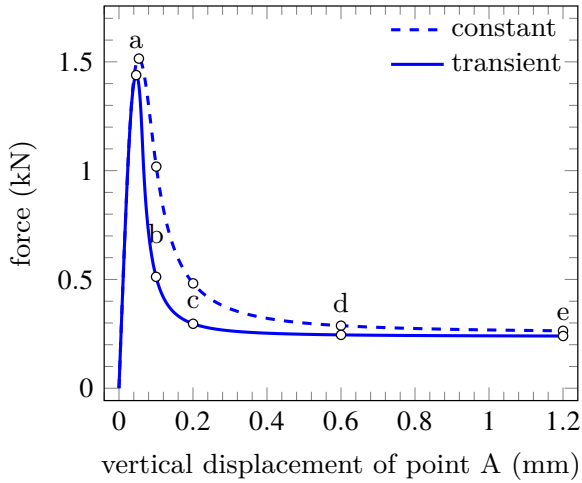

Figure 3.3: Four-point bending beam: force-displacement curves used to verify the presence of the incorrect damage widening in the transient isotropic model.
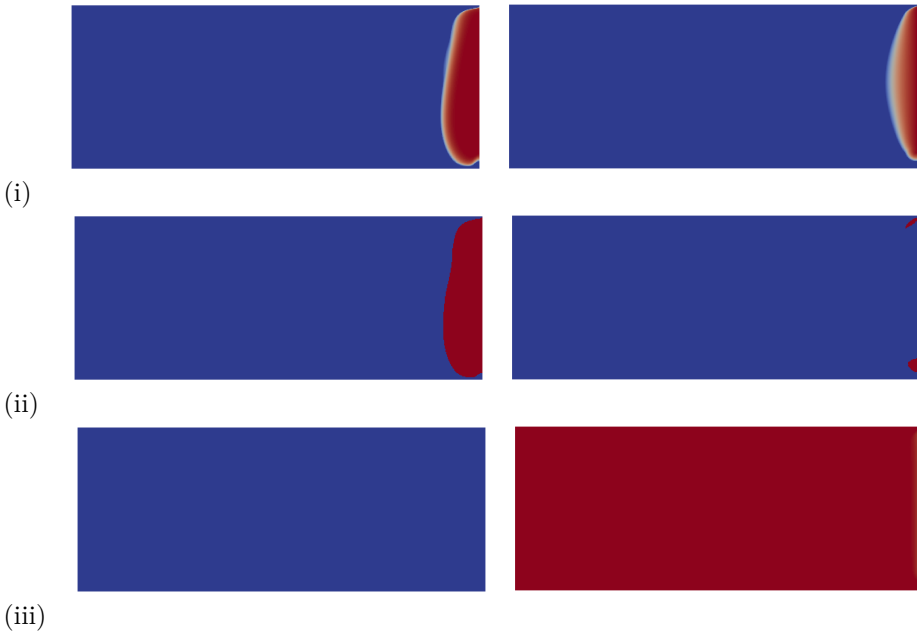
(i)

(ii)

(iii)

Figure 3.4: Four-point bending beam: comparison of the final (i) damage, (ii) loading indicator function and (iii) g contours with (left) constant model and (right) transient isotropic model at displacement point e. The ranges of all figures are [0: blue, 1: red].

From the analysis of the contours shown in Figures 3.4 and 3.5, the presence of incorrect damage widening, albeit limited compared to the constant model, is still evident in the region around the crack tip. In the results obtained from the proposed transient model (i.e., the one shown in the right part of the figures), the growth of both damaged region and loading indicator function are observed in the lower part of the crack-tip, as evident from the comparison of sub-figures (a) and (e) in Figure 3.5. Based on the results of this example, it can be concluded that the proposed transient isotropic model failed to eliminate the incorrect damage widening issue in two-dimensional problems under mode-I failure.

(i) damage

(ii) loading indicator function

(iii) *g*
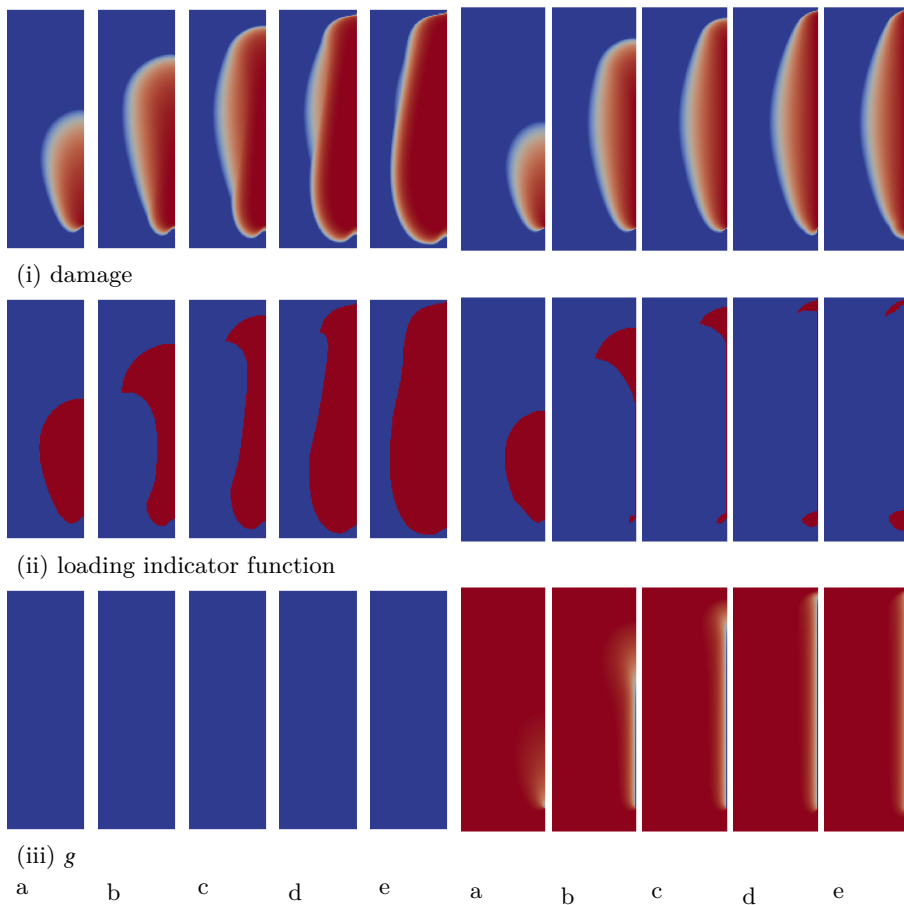
a   b   c   d   e   a   b   c   d   e

Figure 3.5: Four-point bending beam: evolution of (i) damage, (ii) loading indicator function and (iii) *g* contours at different load-increments (left) with constant model and (right) transient model. The ranges of all figures are [0: blue, 1: red]

Table 3.2: Shear-band problem: material and damage parameters.

	symbol	value
Young's modulus	E	20×10^3 MPa
Poisson's ratio	ν	0.2
constant gradient activity parameter	c	2 mm^2, 0.5 mm^2
damage softening law	ω	exponential
damage threshold equivalent strain	κ_0	10^{-4}
softening parameter	β	300
residual parameter	α	0.99
compressive to tensile strength ratio	k	1

3.3.2. Mode-II failure: shear-band problem

As a second two-dimensional test, the shear-band problem shown in Figure 3.6a and reported numerically in [5] is considered. Aim of this example is to show the performance of the proposed transient displacement-based GEDM in two-dimensional problems under mode-II failure. Due to symmetry, only half of the specimen is numerically simulated as shown in Figure 3.6b. The numerical parameters and material properties are listed in Table 3.2. As indicated in Table 3.2, the shear-band problem is studied with two values of the constant gradient activity parameter: $c = 2$ mm^2 and $c = 0.5$ mm^2. A damage threshold equivalent strain in the imperfection zone equals half that reported in Table 3.2.
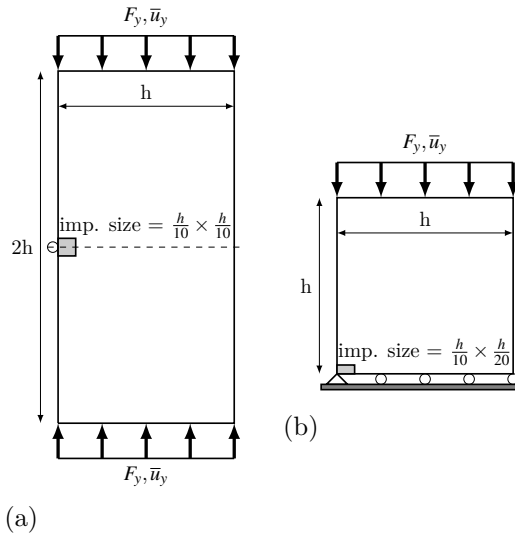

Figure 3.6: Shear-band problem: geometry and boundary conditions for the specimen in biaxial compression: (a) full specimen and (b) half specimen. The shaded part indicates the zone with reduced material property values (unit of length: mm).
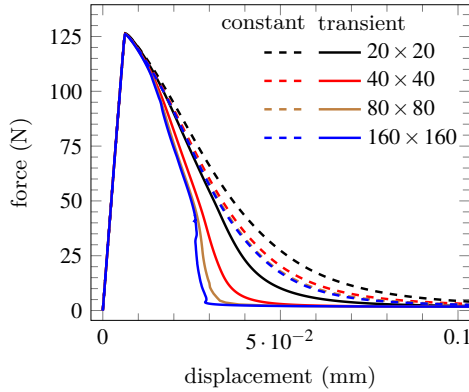
3

Figure 3.7: Shear-band problem: mesh-sensitivity study for $c = 2$ mm^2.

The mesh-sensitivity study for $c = 2$ mm^2 is performed using four uniform mesh configurations with the bilinear quadrilateral elements and the full integration scheme and with element sizes equal to 3, 1.5, 0.75 and 0.375 mm, respectively. For $c = 0.5$ mm^2 five mesh configurations with the bilinear quadrilateral elements and the full integration scheme and with element sizes equal to 3, 1.5, 0.75, 0.375 and 0.1875 mm, are employed. The first coarse mesh consists of 400 elements for both local and nonlocal displacement fields. The medium, fine, finest and tiny mesh configurations contain 1,600, 6,400, 25,600 and 102,400 elements, respectively. The corresponding force-displacement curves for different mesh configurations for $c = 2$ mm^2 and $c = 0.5$ mm^2 are plotted in Figure 3.7 and Figure 3.8, respectively. In these figures, the curves are also compared against the force-displacement curves obtained with a constant length scale model.
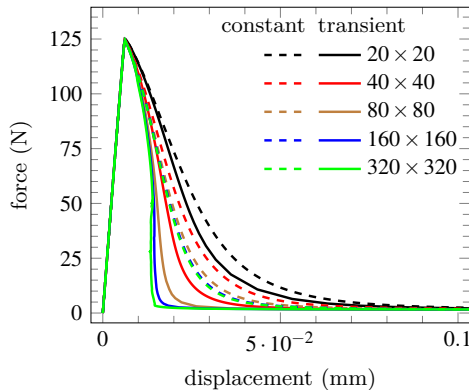

Figure 3.8: Shear-band problem: mesh-sensitivity study for $c = 0.5$ mm^2.

An analysis of the load-displacement curves in Figures 3.7 and 3.8 indicate that, despite the fact that the proposed transient model has a more brittle response when compared to a model with a constant length scale, the regularization of the transient model has been successfully performed and that a mesh size of half of the length scale size (element size equal to 0.75 mm for $c = 2$ mm^2 and the element size equal to 0.375 mm for $c = 0.5$ mm^2) is sufficient to guarantee almost convergence. It is also significant to note that the force-displacement curve shown in Figure 3.7 for $c = 2$ mm^2 with the element size equal to 0.375 mm is not smooth at the softening part, and we have not been able to determine the reason for this.

The mesh configuration with the element size equal to 0.375 mm (mesh configuration 160×160) is used to investigate the efficiency of the transient model in the removal of spurious damage growth. The load level has been increased up until a final displacement equal to 0.4 mm; the force-displacement responses are depicted for $c = 2$ mm^2 and $c = 0.5$ mm^2 in Figure 3.9 and Figure 3.10, respectively. The corresponding damage, nonlocal equivalent strain, loading indicator function and g contours at different load-increments indicated with the snap-shots for $c = 2$ mm^2 and $c = 0.5$ mm^2 are compared in Figures 3.11 and 3.12, respectively. The contours in Figures 3.11 and 3.12 indicate that the transient model, in contrast to the constant model, does not exhibit the incorrect widening of damage. The efficiency of the proposed transient model in addressing the issue of damage widening has been determined by analyzing the localized contour of the loading indicator function, as depicted in sub-figure (e) of Figures 3.11 and 3.12. However, the results were affected by incorrect damage migration, leading to an incorrect final migration point of damage outside of the imperfection zone before the inclined damage profile (i.e., the shear band) appeared. This point is illustrated with a black dashed line in Figures 3.11 and 3.12. In conclusion, despite the existence of incorrect damage migration, albeit to a lesser extent than in the constant model, the proposed transient activity function, with an isotropic gradient activity function, can be utilized to resolve the incorrect damage widening issue when mode II failure occurs in two-dimensional problems.
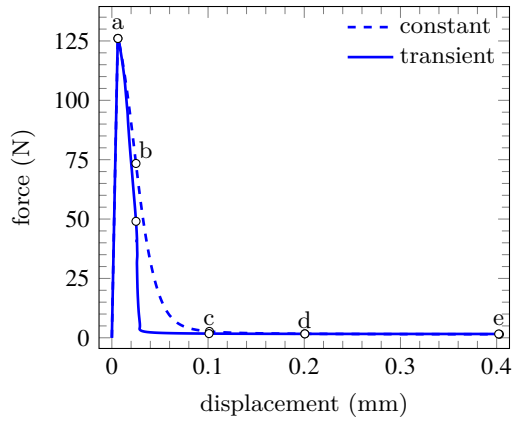
Figure 3.9: Shear-band problem: force-displacement curves with $c = 2 \text{ mm}^2$ using the 160×160 mesh configuration for the study on spurious damage growth.
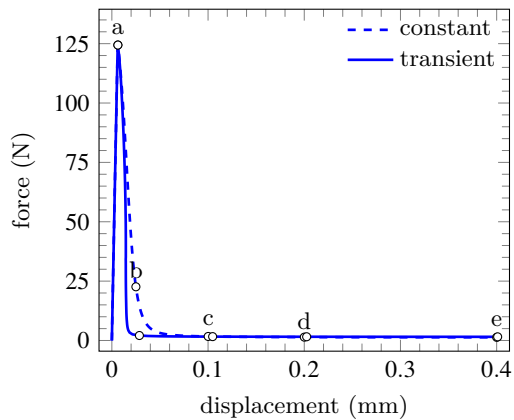
Figure 3.10: Shear-band problem: force-displacement curves with $c = 0.5 \text{ mm}^2$ using 160×160 mesh configuration for checking spurious damage growth.
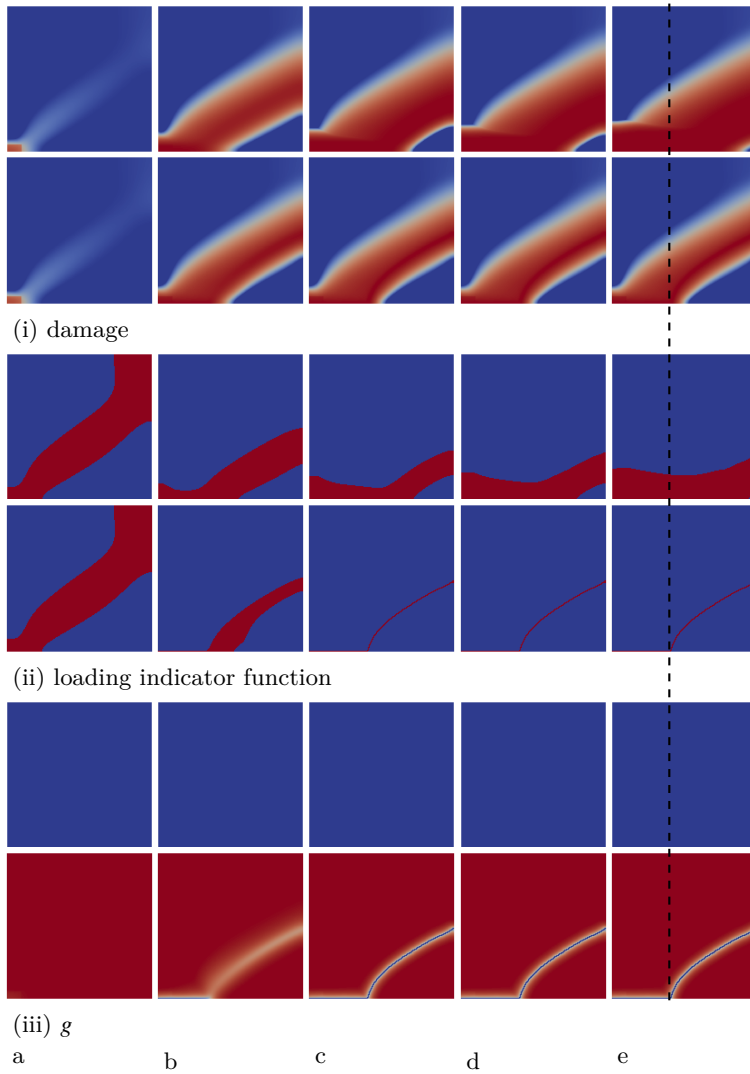
Figure 3.11: Shear-band problem: evolution of (i) damage, (ii) loading indicator function and (iii) g contours with $c = 2 \text{ mm}^2$ at different load-increments on 160×160 mesh configuration, (top) constant model, (bottom) transient model. The ranges of all figures are [0: blue, 1: red]
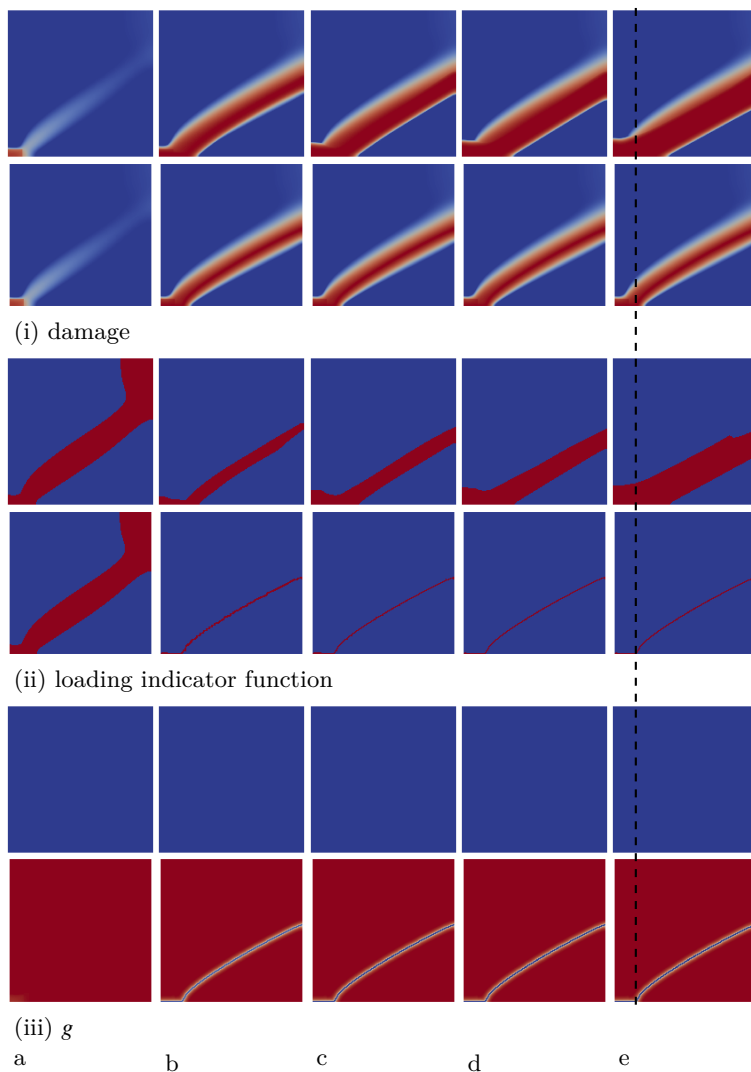
Figure 3.12: Shear-band problem: evolution of (i) damage, (ii) loading indicator function and (iii) g contours with $c = 0.5$ mm^2 at different load-increments on 160×160 mesh configuration, (top) constant model, (bottom) transient model. The ranges of all figures are [0: blue, 1: red]

Table 3.3: L-shaped panel: numerical and material parameters.

	symbol	value
Young's modulus	E	16.5×10^3 MPa
Poisson's ratio	ν	0.18
constant gradient activity parameter	c	0.5 mm^2
damage softening law	ω	exponential
damage threshold equivalent strain	κ_0	2×10^{-4}
softening parameter	β	250
residual parameter	α	0.96
compressive to tensile strength ratio	k	10

3.3.3. L-shaped panel test

Finally, we consider the L-shaped panel test conducted by Winkler [6, 7] which is governed by mode-I failure. Aim of this example is to show the capability of the proposed model to produce a curved and thin damage band. The geometrical properties and boundary conditions are shown in Figure 3.13. A specimen with long edge 500 mm, short edge 250 mm and thickness 100 mm under plane stress condition is investigated. A vertical displacement is applied. The material and numerical parameters are listed in Table 3.3.
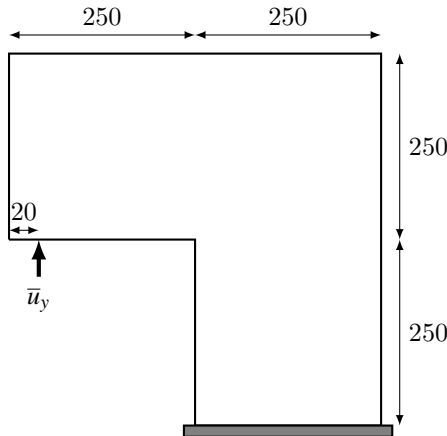
Figure 3.13: L-shaped panel test: geometry and boundary conditions (unit of length: mm).
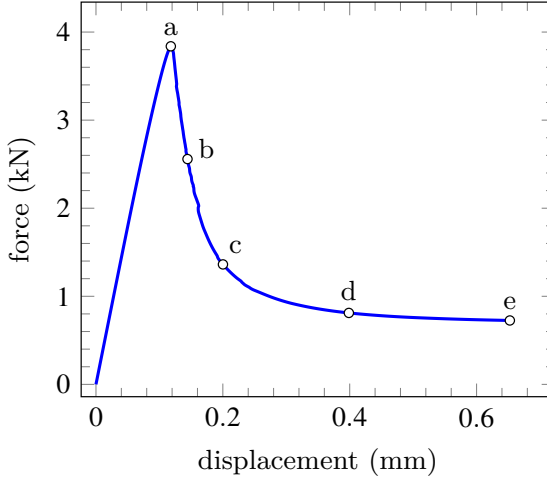
Figure 3.14: L-shaped problem: force-displacement curve for checking spurious damage growth.

Figure 3.14 shows the force-displacement response of the L-shaped specimen and the corresponding damage, nonlocal equivalent strain, loading indicator function and g contours at different load-increments are depicted in Figure 3.15, respectively. Also, the final contours on the full specimen are shown in Figure 3.16. The results indicate that while the proposed transient model is effective for obtaining a curved and thin damage band, a detailed contours analysis (by zooming in Paraview software [8]) shown in Figure 3.15 suggests that the results are affected by the incorrect widening of damage within the area surrounding the notch. This example indicates that the proposed transient activity function cannot solve the issue of incorrect damage widening in mode-I failure, which supports our conclusion from the first benchmark example.
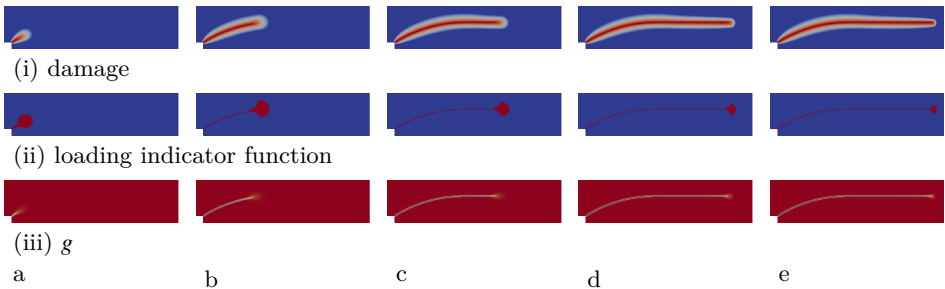
Figure 3.15: L-shaped panel test: (i) damage, (ii) loading indicator function and (iii) g contours at different load-increments. The ranges of all figures are [0: blue, 1: red]
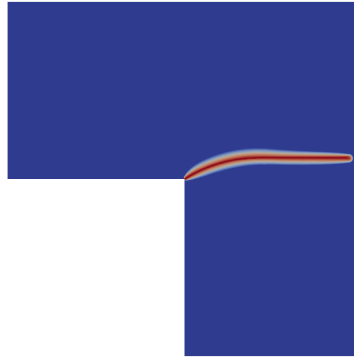
(i) damage
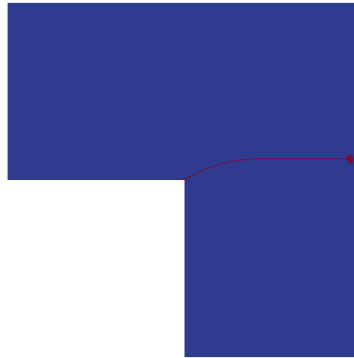
(ii) loading indicator function
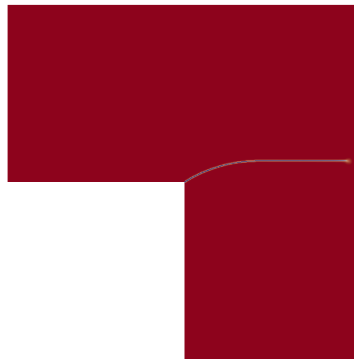
(iii) g

Figure 3.16: L-shaped panel test: final (i) damage, (ii) loading indicator function and (iii) g contours. The ranges of all figures are [0: blue, 1: red]

3.4. Conclusions

This chapter addressed the problem of incorrect damage widening in the gradient-enhanced damage models in a two-dimensional setting. The solution proposed relies on the use of a transient length scale in a displacement-based gradient-enhanced damage model. The choice of a displacement-based model over a classical strain-based model is dictated by some intrinsic features of the former. At variance with classical strain-based models [9], the displacement-based model by Rodríguez-Ferran et al. [10] does not show any pathological behavior when the length scale is set equal to zero and does not alter the representation of the elastic strain field governing damage initiation ahead of a crack tip [3, 5, 11]. However, being based on a diffusion equation, damage widening is an inherent feature if the length scale is kept constant.

As discussed in Chapter 2, the performance of the model strongly depends upon the function that governs the length scale decay. Here we have shown that a mode-I function performs reasonably well also in a mode-II dominated problem. A more in-depth analysis, beyond the heuristic perspective employed in this case, seems however necessary.

In spite of the heuristic definition of the transient length scale, the model can appropriately describe all stages of failure in a continuous setting, from damage initiation to strain localization, irrespective of the thickness of the damage band relative to the specimen size and of the deformation level.

The two-field displacement-based gradient-enhanced damage model has an obvious disadvantage compared to any two-field gradient-enhanced damage model based on a strain-based diffusion equation: the increased number of the degrees of freedom. While in strain-based formulations only one extra degree of freedom per node is needed, irrespective of the spatial dimensions of the problem, in displacement-based formulations the number of extra degrees of freedom per node is equal to the spatial dimensions of the problem.

References

[1] J. De Vree, W. Brekelmans, and M. Van Gils, Comparison of nonlocal approaches in continuum damage mechanics, Computers and Structures 55, 581 (1995).

[2] D. A. Hordijk, Local approach to fatigue of concrete, Phd dissertation, Doctoral Dissertation, Delft University of Technology (1991).

[3] A. Simone, G. N. Wells, and L. J. Sluys, From continuous to discontinuous failure in a gradient-enhanced continuum damage model, Computer Methods in Applied Mechanics and Engineering 192, 4581 (2003).

[4] C. Geuzaine and J.-F. Remacle, Gmsh: A 3-d finite element mesh generator with built-in pre-and post-processing facilities, International journal for numerical methods in engineering 79, 1309 (2009).

[5] A. Simone, H. Askes, and L. J. Sluys, Incorrect initiation and propagation of failure in non-local and gradient-enhanced media, International Journal of Solids and Structures 41, 351 (2004).

[6] B. J. Winkler, Traglastuntersuchungen von unbewehrten und bewehrten Betonstrukturen auf der Grundlage eines objektiven Werkstoffgesetzes für Beton (Innsbruck University Press, 2001).

[7] B. Winkler, G. Hofstetter, and H. Lehar, Application of a constitutive model for concrete to the analysis of a precast segmental tunnel lining, International Journal for Numerical and Analytical Methods in Geomechanics 28, 797 (2004).

[8] J. Ahrens, B. Geveci, and C. Law, ParaView: An End-User Tool for Large Data Visualization, Visualization Handbook (Elsevier, 2005).

[9] R. Peerlings, R. R. de Borst, W. Brekelmans, and J. de Vree, Gradient enhanced damage for quasi-brittle materials, International Journal for Numerical Methods in Engineering 39, 3391 (1996).

[10] A. Rodríguez-Ferran, I. Morata, and A. Huerta, A new damage model based on non-local displacements, International Journal for numerical and analytical methods in geomechanics 29, 473 (2005).

[11] M. Geers, R. de Borst, W. Brekelmans, and R. Peerlings, Strain-based transient-gradient damage model for failure analyses, Computer Methods in Applied Mechanics and Engineering 160, 133 (1998).

3

4

Anisotropic displacement-based GEDM: Two-dimensional study

A transient-anisotropic displacement-based gradient-enhanced damage model is proposed for failure analysis of quasi-brittle materials. This formulation is useful to control the material behavior when tensile or compressive strains are activated or deactivated unequally at different directions. The proposed model contrasts with existing gradient damage models by enhancing the displacement field rather than a nonlocal strain field or related state variable. The need for a correction on the gradient activity operator to obtain the correct kinetics is demonstrated by adjusting the gradient activity parameter upon strain localization. In practical terms this leads to a non-broadening fracture process zone in the wake of the crack tip, addressing one of the main criticisms of existing gradient damage models.

4.1. Introduction

To represent the effects of the presence of a random distribution of microcracks within the framework of continuum damage mechanics, an internal variable called internal length scale is usually employed in regularized descriptions of degradation. In the majority of cases, this quantity has been assumed to be a constant scalar, although there are also numerous examples of its tensorial representation. For homogeneous materials with isotropic material properties, a scalar internal length scale would be sufficient. However, a considerable number of materials in engineering applications such as bones, composites, woods, concrete, and rocks show heterogeneous behavior. Heterogeneity implies anisotropic degradation, and its incorporation into continuum damage models is necessary to properly describe crack patterns in strongly anisotropic materials.

Several anisotropic damage models have been proposed with the aim to represent the anisotropic degradation of quasi-brittle materials. These models are useful to control the material behavior when tensile or compressive strains are activated/deactivated with more or less smoothness. For instance, numerical formulations for anisotropic phase-field modeling of brittle fracture have been investigated in [1]. Nguyen et al. [2] proposed a phase-field model that could reproduce energetically a non-free anisotropic crack bifurcation within a framework allowing for robust and fast numerical simulations. In [3] the standard one-variable phase-field/gradient damage model, able to regularize Griffith's isotropic brittle fracture problem, was extended to describe different degradation mechanisms through several distinct damage variables. Li and Maurini [4] revisit the crack kinking problem in materials with strongly anisotropic surface energies by using a variational phase-field model. The phase-field term has a regularizing effect, energetically penalizing the crack curvature. Wu et al. [5] studied the failure of carbon fiber reinforced epoxy laminates using an anisotropic gradient-enhanced continuum damage model embedded in a mean-field homogenization scheme. Vandoren and Simone [6] proposed two types of anisotropic stress-based gradient-enhanced damage models to address the issue of spurious damage growth typical of standard gradient-enhanced damage models. Both models are based on a decreasing interaction length upon decreasing stresses and do not require additional model parameters or extra degrees of freedom when compared to standard gradient-enhanced models.

This chapter aims to present a family of the anisotropic damage models for the quasi-brittle materials characterized by their capabilities to describe nonlinear progressive stiffness recalculation. The proposed gradient-enhanced damage model contrasts with existing gradient-enhanced damage models by enhancing the displacement field rather than a nonlocal strain or related state variable. The need for a correction on the gradient activity operator is demonstrated. By reducing the gradient activity upon strain localization, the correct field representation for mode-II failure can be obtained. Applicability of the proposed framework is demonstrated by means of representative numerical examples. It should be noted that for the two-dimensional studies, the transient activity function $g_{\tilde{u}}$ that is proposed for a one-dimensional case in Section 2.3.4 is employed.

Following this brief introduction, Section 4.2 is devoted to the formulation and

finite element discretization of a new class of the anisotropic damage models characterized by their abilities to remove the incorrect damage widening and damage migration issues. In Section 4.3 the first two types of anisotropic gradient activity tensors are reviewed and then a new anisotropic gradient activity function is proposed. Section 4.4, is focused on the numerical benchmark shear-band example to highlight the robustness of the model for failure analysis of quasi-brittle materials in mode-II failure. Finally, some concluding remarks are presented in Section 4.5.

4

4.2. Governing equations and discretization
4.2.1. Strong-form equations and boundary conditions

A two-dimensional displacement-based gradient-enhanced damage model with an anisotropic length scale is formulated by a system of a coupled differential equations expressed in terms of the classical equilibrium equation and the modified Helmholtz (diffusion) equation as

$$\nabla^s \cdot \boldsymbol{\sigma} + \mathbf{b} = \mathbf{0}, \quad \text{in} \quad \Omega, \tag{4.1}$$

$$\tilde{\mathbf{u}} - \nabla \cdot \left(\overline{\mathbf{c}} \nabla \tilde{\mathbf{u}} \right) = \mathbf{u}, \quad \text{in} \quad \Omega, \tag{4.2}$$

subject to Dirichlet and Neumann boundary conditions applied to the local displacement field $\mathbf{u}$ and its gradient as

$$\mathbf{u} = \overline{\mathbf{u}}, \qquad \text{on} \quad \Gamma_{\overline{\mathbf{u}}}, \tag{4.3}$$

$$\boldsymbol{\sigma}\underline{\mathbf{n}} = \overline{\mathbf{t}}, \qquad \text{on} \quad \Gamma_{\overline{\mathbf{t}}}, \tag{4.4}$$

and the following Dirichlet and non-homogeneous Neumann boundary conditions applied to the nonlocal displacement field $\tilde{\mathbf{u}}$ and its gradient as

$$\tilde{\mathbf{u}} \cdot \underline{\mathbf{n}} = \mathbf{u} \cdot \underline{\mathbf{n}}, \qquad \text{on} \quad \Gamma, \tag{4.5}$$

$$\underline{\mathbf{n}} \cdot \nabla \tilde{\mathbf{u}} \cdot \mathbf{t} = \underline{\mathbf{n}} \cdot \nabla \mathbf{u} \cdot \mathbf{t}, \qquad \text{on} \quad \Gamma, \tag{4.6}$$

where boundary $\Gamma = \Gamma_{\overline{\mathbf{u}}} \cup \Gamma_{\overline{\mathbf{t}}}$ and $\Gamma_{\overline{\mathbf{u}}} \cap \Gamma_{\overline{\mathbf{t}}} = \oslash$ in which $\overline{\mathbf{u}}$ and $\overline{\mathbf{t}}$ are the prescribed displacement and traction vectors, respectively and $\boldsymbol{\sigma}$ is the stress tensor and $\mathbf{b}$ is the vector of body forces. Matrix $\overline{\mathbf{c}}$ controls the active nonlocal interactions between microcracks and $\mathbf{u}$ and $\tilde{\mathbf{u}}$ are local and smoothed displacement vectors, respectively and $\underline{\mathbf{n}}$ and $\mathbf{t}$ are the outward unit normal vector and tangent vector on the boundary Γ, respectively. The gradient operators ∇^s and ∇ are used for the local and nonlocal displacements and in 2D are defined as

$$\nabla^s = \begin{bmatrix} \frac{\partial}{\partial x} & 0 \\ 0 & \frac{\partial}{\partial y} \\ \frac{\partial}{\partial y} & \frac{\partial}{\partial x} \end{bmatrix}, \tag{4.7}$$

$$\nabla = \begin{bmatrix} \frac{\partial}{\partial x} & 0 \\ \frac{\partial}{\partial y} & 0 \\ 0 & \frac{\partial}{\partial x} \\ 0 & \frac{\partial}{\partial y} \end{bmatrix}. \tag{4.8}$$

4.2.2. Weak formulation

The weighted residual approach is used to obtain the weak-form of the governing equations. To this end, Equations (4.1) and (4.2) are multiplied by the vectorial functions $\mathbf{w}$ and $\tilde{\mathbf{w}}$, respectively. The resulting equations are then integrated over the problem domain Ω to yield

$$\int_{\Omega} \left[\mathbf{w} \cdot (\nabla^s \cdot \boldsymbol{\sigma} + \mathbf{b}) \right] \mathrm{d}\Omega = 0, \tag{4.9}$$

$$\int_{\Omega} \left[\tilde{\mathbf{w}} \cdot \left(\tilde{\mathbf{u}} - \nabla \cdot \left(\overline{\mathbf{c}} \nabla \tilde{\mathbf{u}} \right) \right) \right] \mathrm{d}\Omega = \int_{\Omega} \left[\tilde{\mathbf{w}} \cdot \mathbf{u} \right] \mathrm{d}\Omega. \tag{4.10}$$

Next, the identities

$$\mathbf{w} \cdot (\nabla^s \cdot \boldsymbol{\sigma}) = \nabla^s \cdot (\mathbf{w} \cdot \boldsymbol{\sigma}) - \nabla^s \mathbf{w} : \boldsymbol{\sigma}, \tag{4.11}$$

$$\tilde{\mathbf{w}} \cdot \left[\nabla \cdot \left(\overline{\mathbf{c}} \nabla \tilde{\mathbf{u}} \right) \right] = \nabla \cdot \left(\tilde{\mathbf{w}} \cdot \overline{\mathbf{c}} \nabla \tilde{\mathbf{u}} \right) - \nabla \tilde{\mathbf{w}} : \overline{\mathbf{c}} \nabla \tilde{\mathbf{u}}, \tag{4.12}$$

and

$$\int_{\Omega} \left[\nabla^s \cdot (\mathbf{w} \cdot \boldsymbol{\sigma}) \right] \mathrm{d}\Omega = \int_{\Gamma_{\tilde{\mathbf{t}}}} \left[\mathbf{w} \cdot (\boldsymbol{\sigma} \cdot \underline{\mathbf{n}}) \right] \mathrm{d}\Gamma = \int_{\Gamma_{\tilde{\mathbf{t}}}} \left[\mathbf{w} \cdot \overline{\mathbf{t}} \right] \mathrm{d}\Gamma, \tag{4.13}$$

$$\int_{\Omega} \left[\nabla \cdot \left(\tilde{\mathbf{w}} \cdot \overline{\mathbf{c}} \nabla \tilde{\mathbf{u}} \right) \right] \mathrm{d}\Omega = \int_{\Gamma} \left[\tilde{\mathbf{w}} \cdot \left(\overline{\mathbf{c}} \nabla \tilde{\mathbf{u}} \cdot \underline{\mathbf{n}} \right) \right] \mathrm{d}\Gamma, \tag{4.14}$$

substituted into Equations (4.9) and (4.10) lead to

$$\int_{\Omega} \left[\nabla^s \mathbf{w} : \boldsymbol{\sigma} \right] \mathrm{d}\Omega = \int_{\Omega} \left[\mathbf{w} \cdot \mathbf{b} \right] \mathrm{d}\Omega + \int_{\Gamma_{\tilde{\mathbf{t}}}} \left[\mathbf{w} \cdot \overline{\mathbf{t}} \right] \mathrm{d}\Gamma, \tag{4.15}$$

$$\int_{\Omega} \left[\tilde{\mathbf{w}} \tilde{\mathbf{u}} + \nabla \tilde{\mathbf{w}} : \overline{\mathbf{c}} \nabla \tilde{\mathbf{u}} - \tilde{\mathbf{w}} \mathbf{u} \right] \mathrm{d}\Omega = \int_{\Gamma} \left[\tilde{\mathbf{w}} \cdot \left(\overline{\mathbf{c}} \nabla \tilde{\mathbf{u}} \cdot \underline{\mathbf{n}} \right) \right] \mathrm{d}\Gamma. \tag{4.16}$$

To apply non-homogeneous Neumann boundary condition (Equation (2.8)b) we can decompose $\tilde{\mathbf{w}}$ as an arbitrary function $\tilde{\mathbf{w}} = (\tilde{\mathbf{w}} \cdot \mathbf{t}) \cdot \mathbf{t} + (\tilde{\mathbf{w}} \cdot \underline{\mathbf{n}}) \cdot \underline{\mathbf{n}}$ such that $\tilde{\mathbf{w}} \cdot \underline{\mathbf{n}} = 0$ leading to

$$\int_{\Omega} \left[\nabla^s \mathbf{w} : \boldsymbol{\sigma} \right] \mathrm{d}\Omega = \int_{\Omega} \left[\mathbf{w} \cdot \mathbf{b} \right] \mathrm{d}\Omega + \int_{\Gamma_{\tilde{\mathbf{t}}}} \left[\mathbf{w} \cdot \overline{\mathbf{t}} \right] \mathrm{d}\Gamma, \tag{4.17}$$

$$\int_{\Omega} \left[\tilde{\mathbf{w}} \tilde{\mathbf{u}} + \nabla \tilde{\mathbf{w}} : \overline{\mathbf{c}} \nabla \tilde{\mathbf{u}} - \tilde{\mathbf{w}} \mathbf{u} \right] \mathrm{d}\Omega - \int_{\Gamma} \left[(\tilde{\mathbf{w}} \cdot \mathbf{t}) \cdot \mathbf{t} \cdot \left(\overline{\mathbf{c}} \nabla \tilde{\mathbf{u}} \cdot \underline{\mathbf{n}} \right) \right] \mathrm{d}\Gamma = \mathbf{0}, \tag{4.18}$$

For a two-dimensional problem $\overline{\mathbf{c}} = g\mathbf{c}$ in which the transient activity function g and the matrix $\mathbf{c}$ control the active nonlocal interactions between microcracks.

4.2.3. Finite element discretization

The Bubnov-Galerkin method is employed for the discretization the weak-form of the governing equations. To this end, the local and nonlocal displacement fields, along with the corresponding weight functions, are discretized at the element level as follows:

$$\mathbf{u} = \mathbf{N}_p\mathbf{u}^h, \quad \mathbf{w_u} = \mathbf{N}_p\mathbf{w}_{\mathbf{u}}^h, \quad \nabla^s\mathbf{u} = \nabla^s\mathbf{N}_p\mathbf{u}^h, \quad \nabla^s\mathbf{w_u} = \nabla^s\mathbf{N}_p\mathbf{w}_{\mathbf{u}}^h, \tag{4.19}$$

$$\tilde{\mathbf{u}} = \mathbf{N}_p\tilde{\mathbf{u}}^h, \quad \mathbf{w}_{\tilde{\mathbf{u}}} = \mathbf{N}_p\mathbf{w}_{\tilde{\mathbf{u}}}^h, \quad \nabla\tilde{\mathbf{u}} = \nabla\mathbf{N}_p\tilde{\mathbf{u}}^h, \quad \nabla\mathbf{w}_{\tilde{\mathbf{u}}} = \nabla\mathbf{N}_p\mathbf{w}_{\tilde{\mathbf{u}}}^h, \tag{4.20}$$

The shape function matrix $\mathbf{N}_p$ is used to interpolate both nodal values $\mathbf{u}$ and $\tilde{\mathbf{u}}$, and ∇^s and ∇ are the gradient operators for the local and nonlocal displacements, respectively. For a quadrilateral linear element,

$$\mathbf{N}_p = \begin{bmatrix} N_{p1} & 0 & N_{p2} & 0 & N_{p3} & 0 & N_{p4} & 0 \\ 0 & N_{p1} & 0 & N_{p2} & 0 & N_{p3} & 0 & N_{p4} \end{bmatrix}, \tag{4.21}$$

$$\nabla^s\mathbf{N}_p = \begin{bmatrix} \frac{\partial N_{p1}}{\partial x} & 0 & \frac{\partial N_{p2}}{\partial x} & 0 & \frac{\partial N_{p3}}{\partial x} & 0 & \frac{\partial N_{p4}}{\partial x} & 0 \\ 0 & \frac{\partial N_{p1}}{\partial y} & 0 & \frac{\partial N_{p2}}{\partial y} & 0 & \frac{\partial N_{p3}}{\partial y} & 0 & \frac{\partial N_{p4}}{\partial y} \\ \frac{\partial N_{p1}}{\partial y} & \frac{\partial N_{p1}}{\partial x} & \frac{\partial N_{p2}}{\partial y} & \frac{\partial N_{p2}}{\partial x} & \frac{\partial N_{p3}}{\partial y} & \frac{\partial N_{p3}}{\partial x} & \frac{\partial N_{p4}}{\partial y} & \frac{\partial N_{p4}}{\partial x} \end{bmatrix}, \tag{4.22}$$

$$\nabla\mathbf{N}_p = \begin{bmatrix} \frac{\partial N_{p1}}{\partial x} & 0 & \frac{\partial N_{p2}}{\partial x} & 0 & \frac{\partial N_{p3}}{\partial x} & 0 & \frac{\partial N_{p4}}{\partial x} & 0 \\ \frac{\partial N_{p1}}{\partial y} & 0 & \frac{\partial N_{p2}}{\partial y} & 0 & \frac{\partial N_{p3}}{\partial y} & 0 & \frac{\partial N_{p4}}{\partial y} & 0 \\ 0 & \frac{\partial N_{p1}}{\partial x} & 0 & \frac{\partial N_{p2}}{\partial x} & 0 & \frac{\partial N_{p3}}{\partial x} & 0 & \frac{\partial N_{p4}}{\partial x} \\ 0 & \frac{\partial N_{p1}}{\partial y} & 0 & \frac{\partial N_{p2}}{\partial y} & 0 & \frac{\partial N_{p3}}{\partial y} & 0 & \frac{\partial N_{p4}}{\partial y} \end{bmatrix}. \tag{4.23}$$

The same shape functions are used to interpolate the nodal values of the weight functions $\mathbf{w_u}$ and $\mathbf{w}_{\tilde{\mathbf{u}}}$. Inserting the above relations into Equations (4.18) and (4.18), and expressing the stress and strain tensors in their vector form yields

$$\sum_p \mathbf{w}_{\mathbf{u}}^{h^{\mathrm{T}}}\nabla^s\mathbf{N}_p^{\mathrm{T}}\boldsymbol{\sigma}_p\mathrm{d}v_p = \sum_p \mathbf{w}_{\mathbf{u}}^{h^{\mathrm{T}}}\mathbf{N}_p^{\mathrm{T}}\mathbf{b}_p\mathrm{d}v_p + \int_{\Gamma_{\bar{\mathbf{t}}}} \mathbf{w}_{\mathbf{u}}^{h^{\mathrm{T}}}\mathbf{N}_p^{\mathrm{T}}\bar{\mathbf{t}}_p\mathrm{d}\Gamma, \tag{4.24}$$

$$\sum_p \left[\mathbf{w}_{\tilde{\mathbf{u}}}^{h^{\mathrm{T}}}\mathbf{N}_p^{\mathrm{T}}\mathbf{N}_p\tilde{\mathbf{u}}^h + \mathbf{w}_{\tilde{\mathbf{u}}}^{h^{\mathrm{T}}}\nabla\mathbf{N}_p^{\mathrm{T}}\bar{\mathbf{c}}_p\nabla\mathbf{N}_p\tilde{\mathbf{u}}^h - \mathbf{w}_{\tilde{\mathbf{u}}}^{h^{\mathrm{T}}}\mathbf{N}_p^{\mathrm{T}}\mathbf{N}_p\mathbf{u}^h \right]\mathrm{d}v_p$$

$$- \sum_p \left[\left(\mathbf{w}_{\tilde{\mathbf{u}}}^{h^{\mathrm{T}}}\mathbf{N}_p^{\mathrm{T}} \cdot \mathbf{t}_p \right) \cdot \mathbf{t}_p \cdot \left(\bar{\mathbf{c}}_p\nabla\mathbf{N}_p\tilde{\mathbf{u}}^h \cdot \underline{\mathbf{n}}_p \right) \right]\mathrm{d}\Gamma_p = \mathbf{0}. \tag{4.25}$$

These relations have to hold for any choice of $\mathbf{w_u}$ and $\mathbf{w}_{\tilde{\mathbf{u}}}$. By defining $\mathbf{M}$ and $\mathbf{D}$ as the mass and diffusivity matrices, respectively, as

$$\mathbf{M} = \sum_p \mathbf{N}_p^{\mathrm{T}}\mathbf{N}_p\mathrm{d}v_p, \tag{4.26}$$

$$\mathbf{D} = \sum_p \nabla \mathbf{N}_p^{\mathrm{T}} \overline{\mathbf{c}}_p \nabla \mathbf{N}_p \mathrm{d}v_p, \tag{4.27}$$

and defining

$$\mathbf{K}_{\partial\Omega} = \sum_p \left[(\mathbf{N}_p^{\mathrm{T}} \cdot \mathbf{t}_p) \cdot \mathbf{t}_p \cdot \left(\overline{\mathbf{c}}_p \nabla \mathbf{N}_p \cdot \underline{\mathbf{n}}_p \right) \right] \mathrm{d}\Gamma_p = \sum_p \left[\mathbf{N}_p^{\mathrm{T}} \mathbf{a}_p \overline{\mathbf{c}}_p \nabla \mathbf{N}_p \right] \mathrm{d}\Gamma_p, \tag{4.28}$$

in which

$$\mathbf{a}_p = \left[\begin{array}{cccc} n_x t_x^2 & n_y t_x^2 & n_x t_x t_y & n_y t_x t_y \\ n_x t_x t_y & n_y t_x t_y & n_x t_y^2 & n_y t_y^2 \end{array} \right], \tag{4.29}$$

the discretized form of the governing equations is obtained:

$$\sum_p \nabla^s \mathbf{N}_p^{\mathrm{T}} \boldsymbol{\sigma}_p \mathrm{d}v_p = \sum_p \mathbf{N}_p^{\mathrm{T}} \mathbf{b}_p \mathrm{d}v_p + \int_{\Gamma_{\overline{\mathbf{t}}}} \mathbf{N}_p^{\mathrm{T}} \overline{\mathbf{t}}_p \mathrm{d}\Gamma, \tag{4.30}$$

$$\mathbf{M}\tilde{\mathbf{u}}^h + \mathbf{D}\tilde{\mathbf{u}}^h - \mathbf{M}\mathbf{u}^h - \mathbf{K}_{\partial\Omega}\mathbf{u}^h = \mathbf{0}. \tag{4.31}$$

Finally, the discretized governing equations are rewritten in terms of external and internal nodal forces according to

$$\mathbf{f}_{\mathrm{int}}^{\mathbf{u}} = \mathbf{f}_{\mathrm{ext}}^{\mathbf{u}}, \tag{4.32}$$

$$\mathbf{f}_{\mathrm{int}}^{\tilde{\mathbf{u}}} = \mathbf{f}_{\mathrm{ext}}^{\tilde{\mathbf{u}}}, \tag{4.33}$$

in which

$$\mathbf{f}_{\mathrm{int}}^{\mathbf{u}} = \sum_p \nabla^s \mathbf{N}_p^{\mathrm{T}} \boldsymbol{\sigma}_p \mathrm{d}v_p, \tag{4.34}$$

$$\mathbf{f}_{\mathrm{ext}}^{\mathbf{u}} = \sum_p \mathbf{N}_p^{\mathrm{T}} \mathbf{b}_p \mathrm{d}v_p + \int_{\Gamma_{\overline{\mathbf{t}}}} \mathbf{N}_p^{\mathrm{T}} \overline{\mathbf{t}}_p \mathrm{d}\Gamma, \tag{4.35}$$

$$\mathbf{f}_{\mathrm{int}}^{\tilde{\mathbf{u}}} = \mathbf{M}\tilde{\mathbf{u}}^h + \mathbf{D}\tilde{\mathbf{u}}^h - \mathbf{M}\mathbf{u}^h - \mathbf{K}_{\partial\Omega}\mathbf{u}^h, \tag{4.36}$$

$$\mathbf{f}_{\mathrm{ext}}^{\tilde{\mathbf{u}}} = \mathbf{0}. \tag{4.37}$$

4.2.4. Consistent linearization

A consistent tangent stiffness is obtained by linearization of Equations (4.32) and (4.33) at iteration $i+1$ with respect to the previous iteration i. Accordingly,

$$\mathbf{f}_{\mathrm{ext},i+1}^{\mathbf{u}} = \mathbf{f}_{\mathrm{int},i}^{\mathbf{u}} + \delta\mathbf{f}_{\mathrm{int},i+1}^{\mathbf{u}}, \tag{4.38}$$

$$\mathbf{f}_{\mathrm{ext},i+1}^{\tilde{\mathbf{u}}} = \mathbf{f}_{\mathrm{int},i}^{\tilde{\mathbf{u}}} + \delta\mathbf{f}_{\mathrm{int},i+1}^{\tilde{\mathbf{u}}}, \tag{4.39}$$

gives

$$\delta \mathbf{f}_{\text{int},i+1}^{\mathbf{u}} = \mathbf{f}_{\text{ext},i+1}^{\mathbf{u}} - \mathbf{f}_{\text{int},i}^{\mathbf{u}}, \tag{4.40}$$

$$\delta \mathbf{f}_{\text{int},i+1}^{\mathbf{\tilde{u}}} = \mathbf{f}_{\text{ext},i+1}^{\mathbf{\tilde{u}}} - \mathbf{f}_{\text{int},i}^{\mathbf{\tilde{u}}}, \tag{4.41}$$

where

$$\delta \mathbf{f}_{\text{int},i+1}^{\mathbf{u}} = \sum_p \left[\nabla^s \mathbf{N}_p^{\text{T}} \delta \boldsymbol{\sigma}_{p,i+1} \right] \mathrm{d}v_p, \tag{4.42}$$

$$\delta \mathbf{f}_{\text{int},i+1}^{\mathbf{\tilde{u}}} = \mathbf{M} \delta \mathbf{\tilde{u}}_{i+1}^h - \mathbf{M} \delta \mathbf{u}_{i+1}^h + \mathbf{D} \delta \mathbf{\tilde{u}}_{i+1}^h +$$
$$\delta \mathbf{D}_{i+1} \mathbf{\tilde{u}}^h - \mathbf{K}_{\partial \Omega} \delta \mathbf{u}_{i+1}^h - \delta \mathbf{K}_{\partial \Omega_{i+1}} \mathbf{u}^h. \tag{4.43}$$

To obtain stress variation $\delta \boldsymbol{\sigma}_{i+1}$ we assume the free energy density potential function

$$\psi = \frac{1}{2} (1 - \omega) \, \boldsymbol{\epsilon} : \boldsymbol{\mathcal{C}} : \boldsymbol{\epsilon}, \tag{4.44}$$

from which the stress tensor and its derivative can be obtained through

$$\boldsymbol{\sigma} = \frac{\partial \psi}{\partial \boldsymbol{\epsilon}} = (1 - \omega) \, \boldsymbol{\mathcal{C}} : \boldsymbol{\epsilon}, \tag{4.45}$$

$$\delta \boldsymbol{\sigma}_{i+1} = (1 - \omega_i) \, \boldsymbol{\mathcal{C}} \delta \boldsymbol{\epsilon}_{i+1} - \boldsymbol{\mathcal{C}} \boldsymbol{\epsilon}_i \delta \omega_{i+1}, \tag{4.46}$$

where $\boldsymbol{\mathcal{C}}$ is the fourth order elastic moduli tensor and

$$\delta \boldsymbol{\epsilon}_{i+1} = \nabla^s \mathbf{N}_p \delta \mathbf{u}_{i+1}^h, \qquad \delta \boldsymbol{\tilde{\epsilon}}_{i+1} = \nabla^s \mathbf{N}_p \delta \mathbf{\tilde{u}}_{i+1}^h, \tag{4.47}$$

$$\delta \omega_{i+1} = \left(\frac{\partial \omega}{\partial \tilde{\epsilon}} \right)_i \delta \boldsymbol{\tilde{\epsilon}}_{i+1} = \left(\frac{\partial \omega}{\partial \kappa} \right)_i \left(\frac{\partial \kappa}{\partial \tilde{e}} \right)_i \left(\frac{\partial \tilde{e}}{\partial \tilde{\epsilon}} \right)_i \nabla^s \mathbf{N}_p \delta \mathbf{\tilde{u}}_{i+1}^h. \tag{4.48}$$

The stress variations is therefore expressed as

$$\delta \boldsymbol{\sigma}_{i+1} = (1 - \omega_i) \, \boldsymbol{\mathcal{C}} \nabla^s \mathbf{N}_p \delta \mathbf{u}_{i+1}^h - \boldsymbol{\mathcal{C}} \boldsymbol{\epsilon}_i \left(\frac{\partial \omega}{\partial \tilde{\epsilon}} \right)_i \nabla^s \mathbf{N}_p \delta \mathbf{\tilde{u}}_{i+1}^h. \tag{4.49}$$

Considering that $\mathbf{D}$ and $\mathbf{K}_{\partial \Omega}$ are a function of $\mathbf{u}_{i+1}^h$ and $\mathbf{\tilde{u}}_{i+1}^h$ as

$$\delta \mathbf{D}_{i+1} = \left(\frac{\partial \mathbf{D}}{\partial \mathbf{u}^h} \right)_i \delta \mathbf{u}_{i+1}^h + \left(\frac{\partial \mathbf{D}}{\partial \mathbf{\tilde{u}}^h} \right)_i \delta \mathbf{\tilde{u}}_{i+1}^h, \tag{4.50}$$

$$\delta \mathbf{K}_{\partial \Omega_{i+1}} = \left(\frac{\partial \mathbf{K}_{\partial \Omega}}{\partial \mathbf{u}^h} \right)_i \delta \mathbf{u}_{i+1}^h + \left(\frac{\partial \mathbf{K}_{\partial \Omega}}{\partial \mathbf{\tilde{u}}^h} \right)_i \delta \mathbf{\tilde{u}}_{i+1}^h, \tag{4.51}$$

leads to the expressions

$$\delta \mathbf{f}^{\mathbf{u}}_{\text{int},i+1} = \sum_p \left[\nabla^s \mathbf{N}_p^{\mathrm{T}} (1 - \omega_i) \, \boldsymbol{\mathcal{C}} \nabla^s \mathbf{N}_p \right] \delta \mathbf{u}^h_{i+1} \mathrm{d} v_p - $$

$$\sum_p \left[\nabla^s \mathbf{N}_p^{\mathrm{T}} \boldsymbol{\mathcal{C}} \boldsymbol{\epsilon}_i \left(\frac{\partial \omega}{\partial \tilde{\boldsymbol{\epsilon}}} \right) \nabla^s \mathbf{N}_p \right] \delta \tilde{\mathbf{u}}^h_{i+1} \mathrm{d} v_p, \tag{4.52}$$

$$\delta \mathbf{f}^{\tilde{\mathbf{u}}}_{\text{int},i+1} = \left[-\mathbf{M} - \mathbf{K}_{\partial \Omega} + \frac{\partial \mathbf{D}}{\partial \mathbf{u}^h} \tilde{\mathbf{u}}^h - \frac{\partial \mathbf{K}_{\partial \Omega}}{\partial \mathbf{u}^h} \mathbf{u}^h \right] \delta \mathbf{u}^h_{i+1} + $$

$$\left[\mathbf{M} + \mathbf{D} + \frac{\partial \mathbf{D}}{\partial \tilde{\mathbf{u}}^h} \tilde{\mathbf{u}}^h - \frac{\partial \mathbf{K}_{\partial \Omega}}{\partial \tilde{\mathbf{u}}^h} \mathbf{u}^h \right] \delta \tilde{\mathbf{u}}^h_{i+1}. \tag{4.53}$$

The system of discrete equations at a Newton-Raphson iteration is therefore expressed as

$$\underbrace{\begin{bmatrix} \mathbf{K}^i_{\mathbf{uu}} & \mathbf{K}^i_{\mathbf{u}\tilde{\mathbf{u}}} \\ \mathbf{K}^i_{\tilde{\mathbf{u}}\mathbf{u}} & \mathbf{K}^i_{\tilde{\mathbf{u}}\tilde{\mathbf{u}}} \end{bmatrix}}_{16 \times 16} \underbrace{\begin{bmatrix} \delta \mathbf{u}^{i+1} \\ \delta \tilde{\mathbf{u}}^{i+1} \end{bmatrix}}_{16 \times 1} = \underbrace{\begin{bmatrix} \mathbf{f}^{\mathbf{u}}_{\text{ext},i+1} - \mathbf{f}^{\mathbf{u}}_{\text{int},i} \\ \mathbf{f}^{\tilde{\mathbf{u}}}_{\text{ext},i+1} - \mathbf{f}^{\tilde{\mathbf{u}}}_{\text{int},i} \end{bmatrix}}_{16 \times 1}, \tag{4.54}$$

where the components of the consistent tangent matrix are

$$\underbrace{\mathbf{K}^i_{\mathbf{uu}}}_{8 \times 8} = \sum_p \left[\underbrace{\nabla^s \mathbf{N}_p^{\mathrm{T}}}_{8 \times 3} \underbrace{(1 - \omega_i)}_{\text{scalar}} \underbrace{\boldsymbol{\mathcal{C}}}_{3 \times 3} \underbrace{\nabla^s \mathbf{N}_p}_{3 \times 8} \right] \mathrm{d} v_p, \tag{4.55}$$

$$\underbrace{\mathbf{K}^i_{\mathbf{u}\tilde{\mathbf{u}}}}_{8 \times 8} = \sum_p \left[-\underbrace{\nabla^s \mathbf{N}_p^{\mathrm{T}}}_{8 \times 3} \underbrace{\boldsymbol{\mathcal{C}}}_{3 \times 3} \underbrace{\boldsymbol{\epsilon}_i}_{3 \times 1} \underbrace{\left(\frac{\partial \omega}{\partial \tilde{\boldsymbol{\epsilon}}} \right)_i}_{1 \times 3} \underbrace{\nabla^s \mathbf{N}_p}_{3 \times 8} \right] \mathrm{d} v_p, \tag{4.56}$$

$$\underbrace{\mathbf{K}^i_{\tilde{\mathbf{u}}\mathbf{u}}}_{8 \times 8} = -\underbrace{\mathbf{M}}_{8 \times 8} - \underbrace{\mathbf{K}_{\partial \Omega}}_{8 \times 8} + \underbrace{\frac{\partial \mathbf{D}}{\partial \mathbf{u}^h}}_{8 \times 1} \underbrace{\tilde{\mathbf{u}}^h}_{1 \times 8} - \underbrace{\frac{\partial \mathbf{K}_{\partial \Omega}}{\partial \mathbf{u}^h}}_{8 \times 1} \underbrace{\mathbf{u}^h}_{1 \times 8}, \tag{4.57}$$

$$\underbrace{\mathbf{K}^i_{\tilde{\mathbf{u}}\tilde{\mathbf{u}}}}_{8 \times 8} = \underbrace{\mathbf{M}}_{8 \times 8} + \underbrace{\mathbf{D}}_{8 \times 8} + \underbrace{\frac{\partial \mathbf{D}}{\partial \tilde{\mathbf{u}}^h}}_{8 \times 1} \underbrace{\tilde{\mathbf{u}}^h}_{1 \times 8} - \underbrace{\frac{\partial \mathbf{K}_{\partial \Omega}}{\partial \tilde{\mathbf{u}}^h}}_{8 \times 1} \underbrace{\mathbf{u}^h}_{1 \times 8}, \tag{4.58}$$

with

$$
\underbrace{\frac{\partial \mathbf{D}}{\partial \mathbf{u}^h} \tilde{\mathbf{u}}^h}_{8\times8} = \sum_p \left[\frac{\partial g_p}{\partial \mathbf{u}^h} \underbrace{\tilde{\mathbf{u}}^h}_{1\times8} \underbrace{\tilde{\mathbf{u}}^h}_{8\times1} \underbrace{\nabla \mathbf{N}_p^{\mathrm{T}}}_{8\times4} \underbrace{\mathbf{c}_p}_{4\times4} \underbrace{\nabla \mathbf{N}_p}_{4\times8} + \underbrace{g_p}_{\text{scalar}} \frac{\partial \mathbf{c}_p}{\partial \mathbf{u}^h} \underbrace{\tilde{\mathbf{u}}^h}_{1\times8} \underbrace{\tilde{\mathbf{u}}^h}_{8\times1} \underbrace{\nabla \mathbf{N}_p^{\mathrm{T}}}_{8\times4} \underbrace{\nabla \mathbf{N}_p}_{4\times8} \right] \mathrm{d}v_p, \quad (4.59)
$$

$$
\underbrace{\frac{\partial \mathbf{D}}{\partial \tilde{\mathbf{u}}^h} \tilde{\mathbf{u}}^h}_{8\times8} = \sum_p \left[\frac{\partial g_p}{\partial \tilde{\mathbf{u}}^h} \underbrace{\tilde{\mathbf{u}}^h}_{1\times8} \underbrace{\tilde{\mathbf{u}}^h}_{8\times1} \underbrace{\nabla \mathbf{N}_p^{\mathrm{T}}}_{8\times4} \underbrace{\mathbf{c}_p}_{4\times4} \underbrace{\nabla \mathbf{N}_p}_{4\times8} + \underbrace{g_p}_{\text{scalar}} \frac{\partial \mathbf{c}_p}{\partial \tilde{\mathbf{u}}^h} \underbrace{\tilde{\mathbf{u}}^h}_{1\times8} \underbrace{\tilde{\mathbf{u}}^h}_{8\times1} \underbrace{\nabla \mathbf{N}_p^{\mathrm{T}}}_{8\times4} \underbrace{\nabla \mathbf{N}_p}_{4\times8} \right] \mathrm{d}v_p, \quad (4.60)
$$

$$
\underbrace{\frac{\partial \mathbf{K}_{\partial\Omega}}{\partial \mathbf{u}^h} \mathbf{u}^h}_{8\times8} = \sum_p \left[\frac{\partial g_p}{\partial \mathbf{u}^h} \underbrace{\mathbf{u}^h}_{1\times8} \underbrace{\mathbf{u}^h}_{8\times1} \underbrace{\mathbf{N}_p^{\mathrm{T}}}_{8\times2} \underbrace{\mathbf{a}_p}_{2\times4} \underbrace{\mathbf{c}_p}_{4\times4} \underbrace{\nabla \mathbf{N}_p}_{4\times8} + \underbrace{g_p}_{\text{scalar}} \frac{\partial \mathbf{c}_p}{\partial \mathbf{u}^h} \underbrace{\mathbf{u}^h}_{1\times8} \underbrace{\mathbf{u}^h}_{8\times1} \underbrace{\mathbf{N}_p^{\mathrm{T}}}_{8\times2} \underbrace{\mathbf{a}_p}_{2\times4} \underbrace{\nabla \mathbf{N}_p}_{4\times8} \right] \mathrm{d}\Gamma_p (4.61)
$$

$$
\underbrace{\frac{\partial \mathbf{K}_{\partial\Omega}}{\partial \tilde{\mathbf{u}}^h} \mathbf{u}^h}_{8\times8} = \sum_p \left[\frac{\partial g_p}{\partial \tilde{\mathbf{u}}^h} \underbrace{\mathbf{u}^h}_{1\times8} \underbrace{\mathbf{u}^h}_{8\times1} \underbrace{\mathbf{N}_p^{\mathrm{T}}}_{8\times2} \underbrace{\mathbf{a}_p}_{2\times4} \underbrace{\mathbf{c}_p}_{4\times4} \underbrace{\nabla \mathbf{N}_p}_{4\times8} + \underbrace{g_p}_{\text{scalar}} \frac{\partial \mathbf{c}_p}{\partial \tilde{\mathbf{u}}^h} \underbrace{\mathbf{u}^h}_{1\times8} \underbrace{\mathbf{u}^h}_{8\times1} \underbrace{\mathbf{N}_p^{\mathrm{T}}}_{8\times2} \underbrace{\mathbf{a}_p}_{2\times4} \underbrace{\nabla \mathbf{N}_p}_{4\times8} \right] \mathrm{d}\Gamma_p (4.62)
$$

4.3. Gradient activity function

In the proposed anisotropic formulation of displacement-based gradient-enhanced damage model, the constant gradient activity parameter c is replaced by a second-order tensor $\overline{\mathbf{c}} = g\mathbf{c}$ in which the transient activity function g and the matrix $\mathbf{c}$ control the active nonlocal interactions between microcracks. The matrix $\mathbf{c}$ for a two-dimensional case is defined as

$$
\mathbf{c} = \left[\begin{array}{cccc} c_{xx} & c_{xy} & 0 & 0 \\ c_{yx} & c_{yy} & 0 & 0 \\ 0 & 0 & c_{xx} & c_{xy} \\ 0 & 0 & c_{yx} & c_{yy} \end{array} \right].
\tag{4.63}
$$

In case of isotropic diffusion, $g = 1$ and the shear components of the $\mathbf{c}$ matrix are zero ($c_{xy} = c_{yx} = 0$) and $c_{xx} = c_{yy} = c$ in which $c = \ell_0^2$. Below, first we describe two types of anisotropic models proposed in the stress-based GEDM [6]. Then, we propose a new anisotropic function to better capture the material anisotropy.

4.3.1. Anisotropic model based on principal stresses and with a constant length scale

As a first preliminary version, as defined in [6], the gradient activity function is modified by expressing it as a function of the principal stresses:

$$
c_{xx} = \frac{c \left(\sigma_{xx}^2 + \tau_{xy}^2 \right)}{E^2 \kappa_0^2},
\tag{4.64}
$$

$$
c_{yy} = \frac{c \left(\sigma_{yy}^2 + \tau_{xy}^2 \right)}{E^2 \kappa_0^2},
\tag{4.65}
$$

$$
c_{xy} = c_{yx} = \frac{c \tau_{xy} \left(\sigma_{xx} + \sigma_{yy} \right)}{E^2 \kappa_0^2},
\tag{4.66}
$$

and with a constant activity function, $g = 1$. These choices imply

$$
\frac{\partial g_p}{\partial \mathbf{u}} = 0, \qquad \frac{\partial g_p}{\partial \tilde{\mathbf{u}}} = 0,
\tag{4.67}
$$

and

$$
\frac{\partial \mathbf{c}_p}{\partial \mathbf{u}} = \frac{\partial \mathbf{c}_p}{\partial \boldsymbol{\sigma}_p} \frac{\partial \boldsymbol{\sigma}_p}{\partial \boldsymbol{\epsilon}_p} \frac{\partial \boldsymbol{\epsilon}_p}{\partial \mathbf{u}} = \frac{\partial \mathbf{c}_p}{\partial \boldsymbol{\sigma}_p} (1 - \omega_p) \, \mathcal{C} \nabla^s \mathbf{N}_p,
\tag{4.68}
$$

where $\mathcal{C}$ is the fourth order elastic moduli tensor and

$$
\frac{\partial \mathbf{c}_p}{\partial \tilde{\mathbf{u}}} = \frac{\partial \mathbf{c}_p}{\partial \boldsymbol{\sigma}_p} \frac{\partial \boldsymbol{\sigma}_p}{\partial \omega_p} \frac{\partial \omega_p}{\partial \kappa_p} \frac{\partial \kappa_p}{\partial \tilde{e}_p} \frac{\partial \tilde{e}_p}{\partial \tilde{\boldsymbol{\epsilon}}_p} \frac{\partial \tilde{\boldsymbol{\epsilon}}_p}{\partial \tilde{\mathbf{u}}} = -\frac{\partial \mathbf{c}_p}{\partial \boldsymbol{\sigma}_p} \mathcal{C} \boldsymbol{\epsilon}_p \frac{\partial \omega_p}{\partial \kappa_p} \frac{\partial \kappa_p}{\partial \tilde{e}_p} \frac{\partial \tilde{e}_p}{\partial \tilde{\boldsymbol{\epsilon}}_p} \nabla^s \mathbf{N}_p.
\tag{4.69}
$$

The derivatives $\frac{\partial \mathbf{c}_p}{\partial \boldsymbol{\sigma}_p}$ are defined as

$$
\frac{\partial \mathbf{c}_p}{\partial \boldsymbol{\sigma}_p} = \left[\begin{array}{ccc} \frac{\partial c_{xxp}}{\partial \boldsymbol{\sigma}_p} & \frac{\partial c_{yyp}}{\partial \boldsymbol{\sigma}_p} & \frac{\partial c_{xyp}}{\partial \boldsymbol{\sigma}_p} \end{array} \right]
\tag{4.70}
$$

4.3.2. Anisotropic model based on equivalent stresses combined with a transient length scale from strain-based model

As an improved version of the previous anisotropic model to avoid the oscillations in the force-displacement responses, a model based on an equivalent stress measure has been proposed [6]. In this model, an anisotropic gradient activity function is combined with a transient activity function to improve model performance. To this end, the following expressions of the components of the **c** matrix are used:

$$c_{xx} = \frac{c\left(\sigma_{xx}^2 + \tau_{xy}^2\right)}{\max(\sigma_1^2, \sigma_2^2)}, \tag{4.71}$$

$$c_{yy} = \frac{c\left(\sigma_{yy}^2 + \tau_{xy}^2\right)}{\max(\sigma_1^2, \sigma_2^2)}, \tag{4.72}$$

$$c_{xy} = c_{yx} = \frac{c\tau_{xy}\left(\sigma_{xx} + \sigma_{yy}\right)}{\max(\sigma_1^2, \sigma_2^2)}, \tag{4.73}$$

in which σ_1 and σ_2 are the principal stresses and the transient length scale expression from a strain-based model is employed:

$$g = \begin{cases} 1 & \text{if } \tilde{e} < \kappa_0 \\ (1 - \overline{\omega})\frac{\tilde{e}}{\kappa_0} & \text{else} \end{cases}, \tag{4.74}$$

in which $\overline{\omega} = 1 - \frac{\kappa_0}{\kappa}\left[\exp(-\overline{\beta}(\kappa - \kappa_0))\right]$ is the damage value computed by using the modified exponential damage softening law obtained with $\overline{\alpha} = 1$; $\overline{\beta}$ is an extra model parameter used to control the damage band. It should be noticed that $\overline{\beta}$ can be different than β, which is the material parameter used in the damage evolution law.

Taking the derivative of the transient activity function gives

$$\frac{\partial g_p}{\partial \mathbf{u}} = 0, \tag{4.75}$$

$$\frac{\partial g_p}{\partial \tilde{\mathbf{u}}} = \begin{cases} 0 & \text{if } \tilde{e} < \kappa_0 \\ \frac{\partial g_p}{\partial \tilde{e}_p}\frac{\partial \tilde{e}_p}{\partial \tilde{\epsilon}_p}\frac{\partial \tilde{\epsilon}_p}{\partial \tilde{\mathbf{u}}} & \text{else} \end{cases}. \tag{4.76}$$

4.3.3. Modified anisotropic model based on equivalent stresses combined with a transient length scale based on equivalent dissipation with the strain-based model

Although the gradient activity functions presented in the previous chapters work correctly in the strain-based model, our numerical investigations showed their deficiencies when combined with the displacement-based GEDM. The anisotropic model based on principal stresses and with a constant length scale shows oscillations in the force-displacement response. Also, both models show a too brittle force-displacement response. To avoid these issues, a new anisotropic model based on equivalent stress, combined with a transient length scale which is based on an equivalent dissipation with the strain-based model, is proposed. In this model

$$c_{xx} = \frac{c\left(\sigma_{xx}^2 + \tau_{xy}^2\right)}{\max(\sigma_1^2, \sigma_2^2)}, \tag{4.77}$$

$$c_{yy} = \frac{c\left(\sigma_{yy}^2 + \tau_{xy}^2\right)}{\max(\sigma_1^2, \sigma_2^2)}, \tag{4.78}$$

$$c_{xy} = c_{yx} = \frac{c\tau_{xy}^2}{\max(\sigma_1^2, \sigma_2^2)}, \tag{4.79}$$

and a transient length scale based on the equivalent dissipation with the strain-based model that has been proposed in Section 2.3.4 is employed:

$$g = g_{\tilde{u}} = \begin{cases} 1 & \text{if} \quad \tilde{e} < \kappa_0 \\ \frac{1}{\tilde{e}}\left[\kappa_0 - \frac{1}{\beta}\left(\exp\left(-\beta(\tilde{e} - \kappa_0)\right) - 1\right)\right] & \text{else} \end{cases}. \tag{4.80}$$

Taking the derivative of the transient activity function gives

$$\frac{\partial g_p}{\partial \mathbf{u}} = 0, \tag{4.81}$$

$$\frac{\partial g_p}{\partial \tilde{\mathbf{u}}} = \begin{cases} 0 & \text{if} \quad \tilde{e} < \kappa_0 \\ \frac{\partial g_p}{\partial \tilde{e}_p}\frac{\partial \tilde{e}_p}{\partial \tilde{\epsilon}_p}\frac{\partial \tilde{\epsilon}_p}{\partial \tilde{\mathbf{u}}} & \text{else} \end{cases}. \tag{4.82}$$

4.4. Results and discussions

In this section, the merits of the proposed anisotropic displacement-based gradient-enhanced damage model for failure analysis of quasi-brittle materials is demonstrated by means of a two-dimensional benchmark example. The modified anisotropic model based on equivalent stresses equipped with a transient length scale that is based on an equivalent dissipation with the strain-based model (presented in Section 4.3.3) is employed. First, the performance of the proposed model is investigated for removing spurious damage growth in model-I failure by means of a notched four-point concrete beam test (see Figure 3.1 and Table 3.1). Then, the formation of shear-bands in model-II failure is investigated on a plate with an imperfection (see Figure 3.6 and Table 3.2). A linear quadrilateral element-type with a full integration scheme is used for both local and smoothed displacement fields. These numerical tests use the transient activity function $g_{\tilde{u}}$ that is proposed in Section 2.3.4 and the modified gradient activity function presented in Section 4.3.3. It should be noticed that in the following results a constant gradient activity matrix is used during a load increment (this means that the components of the gradient activity matrix are kept constant in the Newton-Raphson iterations of a load increment). According to the anisotropic gradient activity matrix, **c**, defined in Section 4.3, its components update between load increments with respect to the stress components. Although the transient anisotropic formulation is consistently linearized, which means the convergence is quadratic, in the simulations with variable components of the gradient activity matrix in the Newton-Raphson iterations, the solution is not converging after the start of damage growth.

4.4.1. Mode-I failure: a notched four-point concrete beam

Aim of this example is to show the performance of the proposed transient anisotropic model for removing the incorrect damage widening in two-dimensional problems under mode-I failure. For the mesh sensitivity study, four pre-refined mesh configurations with bilinear quadrilateral elements and with element sizes in the central part (damaged zone) of the beam equal to 2.5, 1.25, 0.625 and 0.3125 mm are generated using Gmsh [7]. The corresponding force-displacement curves are plotted in Figure 4.1 and compared to those obtained with the transient isotropic model proposed and tested in the previous chapters. As shown in Figure 4.1, apart from a more brittle response of the proposed transient anisotropic model in comparison with the transient isotropic model, the load-displacement curves show that the transient anisotropic model is properly regularized and a mesh size equal to 1.25 mm, almost half of the length scale size $\ell_0 = 2\,\mathbf{mm}$, is sufficient to guarantee a converged mesh-independent solution. Also, the figure indicates that the proposed transient anisotropic model shows faster mesh convergence in comparison with the transient isotropic model. As a conclusion, the proposed transient anisotropic model is less sensitive to changes in the mesh size because by employing an anisotropic length scale the unnecessary nonlocal interactions that exist in the isotropic model are excluded.
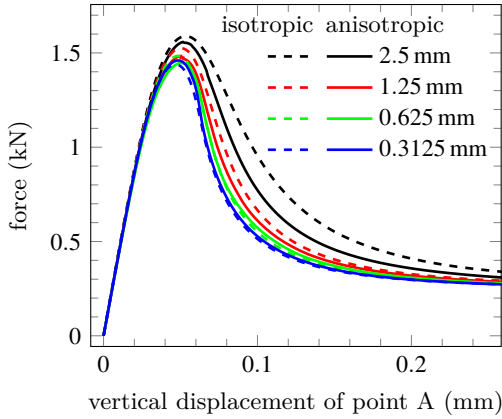
Figure 4.1: Four-point bending beam: mesh-sensitivity study for the transient anisotropic model with evolving $g_{\tilde{u}}$ (solid) and the isotropic model with evolving $g_{\tilde{u}}$ (dashed).

After analyzing the specimen under various deformation levels labeled as a, b, and c, in Figure 4.2, it became apparent that the efficiency of the proposed model in the removal of the incorrect damage widening can be evaluated with the same deformation level obtained in Figure 4.1. Hence, there was no need to increase the deformation level any further. Results are reported for the proposed transient anisotropic and the transient isotropic models in Figure 4.2. In Figure 4.3 the final damage, nonlocal equivalent strain, loading indicator function and g contours on the half of the specimen are compared and the corresponding contours at the indicated snap-shots are compared in Figure 4.4 using the finest mesh configuration with the element size equal to 0.3125 mm.
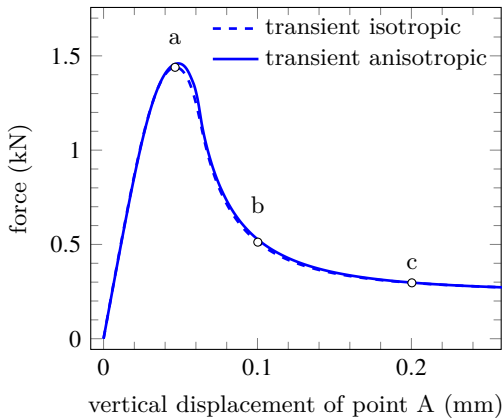

Figure 4.2: Four-point bending beam: force-displacement curves used to verify the presence of the incorrect damage widening in the transient anisotropic model.
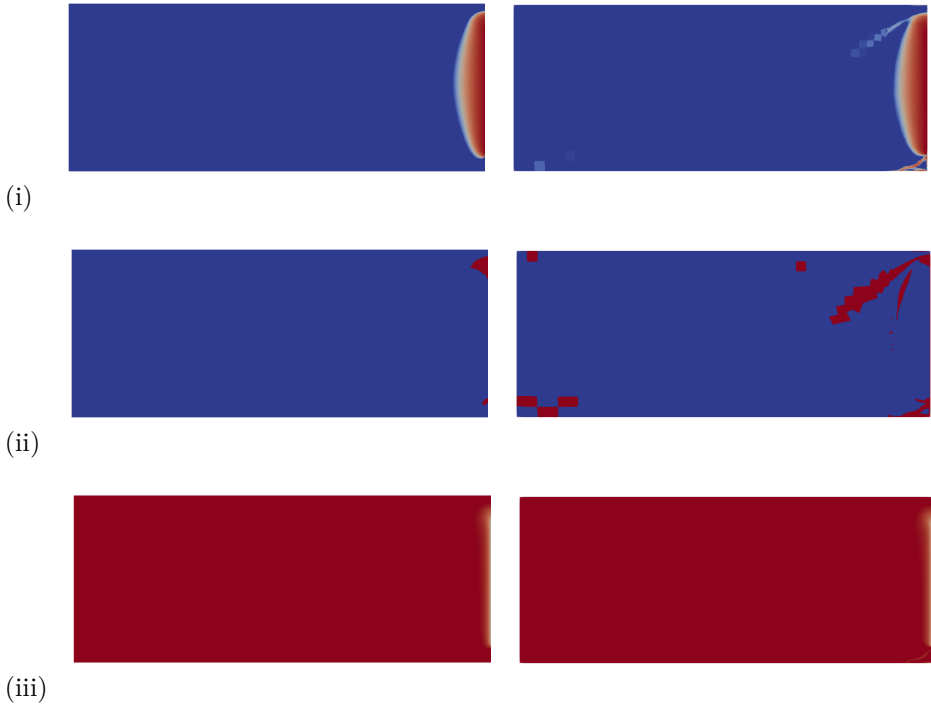
4

(i)

(ii)

(iii)

Figure 4.3: Four-point bending beam: comparison of the final (i) damage, (ii) loading indicator function and (iii) g contours with (left) transient isotropic model and (right) transient anisotropic model at displacement point c. The ranges of all figures are [0: blue, 1: red].

Analysis of the contours in Figures 4.3 and 4.4 reveals that there is still evidence of incorrect damage widening around the crack tip. As shown in sub-figure (c) of Figure 4.4, for the results obtained from the proposed transient-anisotropic model discussed in this chapter (i.e., the one displayed on the right side of the figures), both the damaged region and the loading indicator function exhibit a widening trend around the crack tip. It is evident from the comparison with the results obtained from the proposed transient model discussed in the previous chapter (i.e., displayed on the left side of the figure) that the incorporation of the proposed anisotropy has adversely affected the results. In conclusion, the results of this example demonstrate that the proposed transient anisotropic model is unable to completely eliminate the incorrect damage widening issue in two-dimensional problems under mode-I failure condition.

(i) damage

(ii) loading indicator function

(iii) g

a   b   c   a   b   c

Figure 4.4: Four-point bending beam: evolution of (i) damage, (ii) loading indicator function and (iii) g contours at different load-increments (left) with transient isotropic model and (right) transient anisotropic model. The ranges of all figures are [0: blue, 1: red]

4.4.2. Mode-II failure: shear-band problem

This example is intended to demonstrate the performance of the proposed transient anisotropic displacement-based GEDM for removing the incorrect damage migration issue in the two-dimensional problems under mode-II failure. As indicated in Table 3.2, the shear-band problem is studied with two values of the constant gradient activity parameter: $c = 2 \text{ mm}^2$ and $c = 0.5 \text{ mm}^2$.

The mesh-sensitivity study for $c = 2 \text{ mm}^2$ is performed using four uniform mesh configurations with bilinear quadrilateral elements with sizes equal to 3, 1.5, 0.75 and 0.375 mm, respectively. The first coarse mesh consists of 400 four-node quadrilateral elements for both local and nonlocal displacement fields. The medium, fine and finest mesh configurations contain 1,600, 6,400 and 25,600 elements, respectively. The corresponding force-displacement curves are plotted in Figure 4.5.

An analysis of the load-displacement curves in Figure 4.5 indicate that, despite the fact that the proposed transient anisotropic model has a more brittle response when compared to the transient isotropic model, the regularization of the transient anisotropic model has been successfully performed and that a mesh size of half the length scale size (element size equal to 0.75 mm for $c = 2 \text{ mm}^2$) is sufficient to guarantee an almost mesh-independent solution. In addition, it is noteworthy that the force-displacement curve shown in Figure 4.5 for $c = 2 \text{ mm}^2$ with the element size equal to 0.375 mm is not smooth at the softening part, and we have not been able to determine the cause.
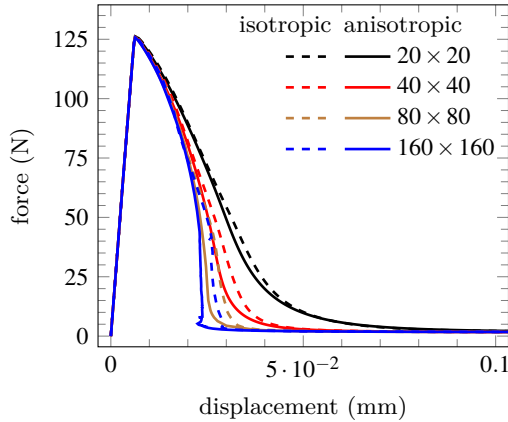

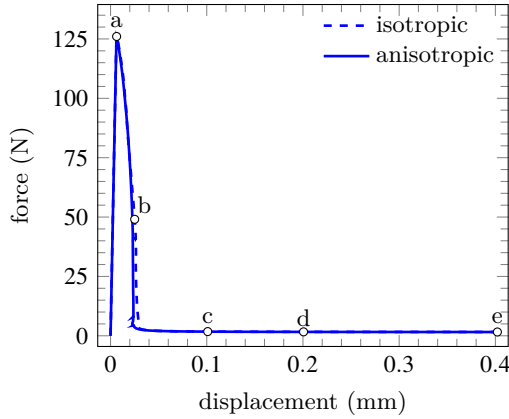Figure 4.5: Shear-band problem: mesh-sensitivity study for $c = 2 \text{ mm}^2$.

Figure 4.6: Shear-band problem: force-displacement curves with $c = 2$ mm^2 using the 160×160 mesh configuration to check spurious damage growth.

The discretization with element size equal to 0.375 mm (mesh configuration 160 × 160) is used to investigate the efficiency of the model for the removal of spurious damage growth (widening and migration). The load level has been extended compared to the mesh-sensitivity study and the force-displacement responses for $c = 2$ mm^2 and $c = 0.5$ mm^2 are depicted in Figures 4.6 and 4.7, respectively.
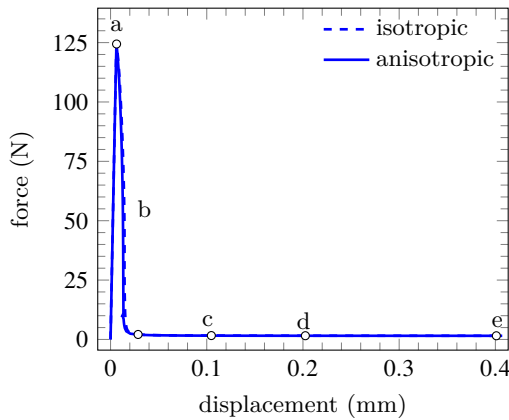

Figure 4.7: Shear-band problem: force-displacement curves with $c = 0.5$ mm^2 using 160×160 mesh configuration to check spurious damage growth.

4

(i) damage

(ii) loading indicator function
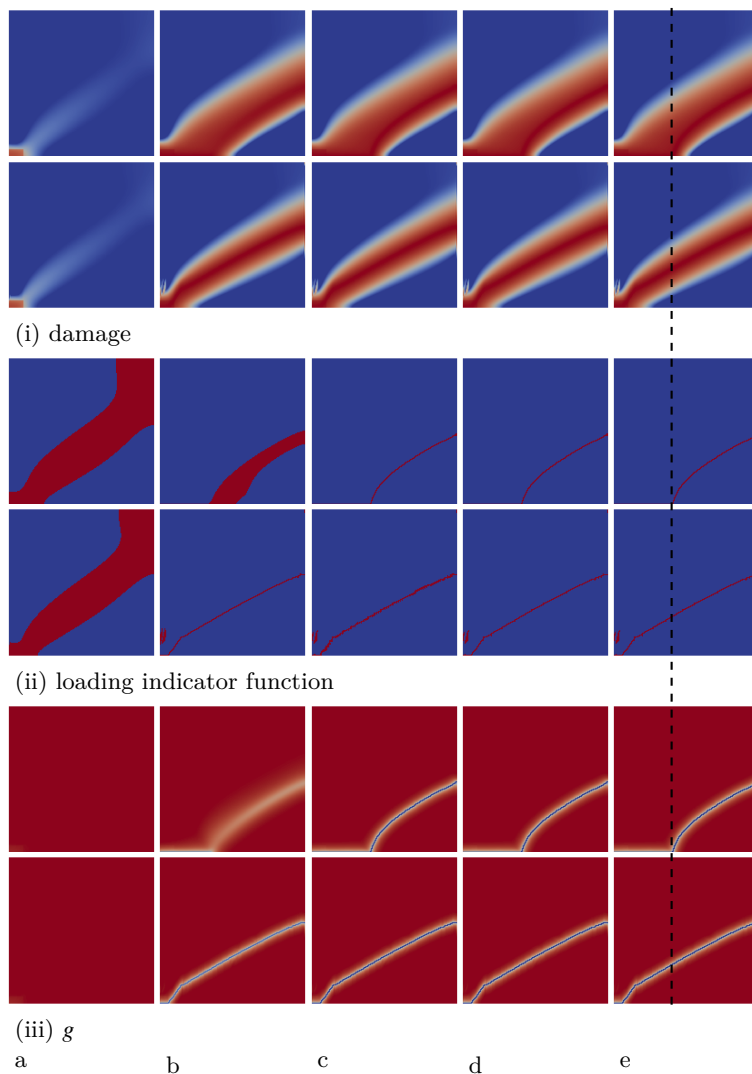
(iii) g

a   b   c   d   e

Figure 4.8: Shear-band problem: evolution of (i) damage, (ii) loading indicator function and (iii) g contours with $c = 2$ mm^2 at different load-increments on 160×160 mesh configuration, (top) transient isotropic model, (bottom) transient anisotropic model. The ranges of all figures are [0: blue, 1: red]

The corresponding damage, nonlocal equivalent strain, loading indicator function and g contours at different load-increments indicated with the snap-shots for the proposed transient anisotropic model with $c = 2$ mm^2 and $c = 0.5$ mm^2 are compared in Figures 4.8 and 4.9 against the transient isotropic model, respectively.

(i) damage

(ii) loading indicator function

(iii) g

a   b   c   d   e
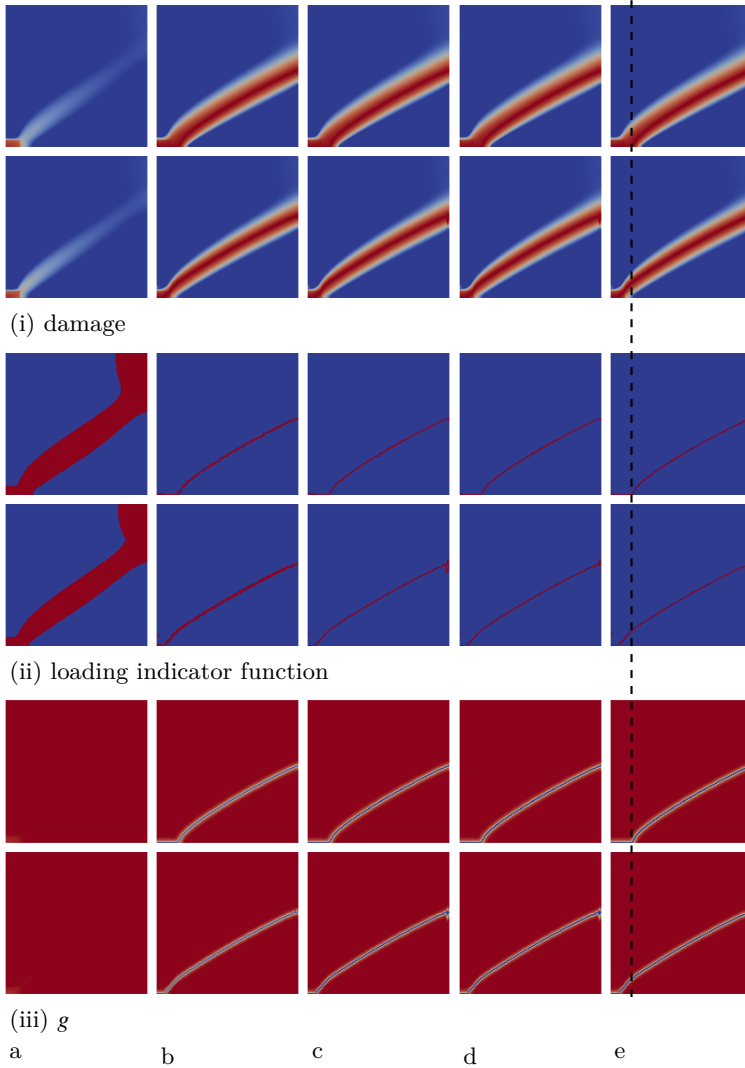
Figure 4.9: Shear-band problem: evolution of (i) damage, (ii) loading indicator function and (iii) g contours with $c = 0.5$ mm^2 at different load-increments on 160×160 mesh configuration, (top) transient isotropic model, (bottom) transient anisotropic model. The ranges of all figures are [0: blue, 1: red]

Figures 4.8 and 4.9 illustrate that the transient anisotropic model does not exhibit incorrect damage migration and is able to resolve the incorrect widening issue as well as the transient isotropic model. The proposed transient anisotropic model's efficiency in addressing the issue of damage widening has been determined by analyzing the localized contour of the loading indicator function, as depicted in subfigures (e) of Figures 4.8 and 4.9. Furthermore, comparing the intersection points of the black dashed line (which indicates the final migration point of the transient

isotropic model) with the sub-figure (e) of the loading indicator function in Figures 4.8 and 4.9 indicates that, unlike the transient isotropic model, the results of the transient anisotropic model were not affected by incorrect damage migration. This leads to a correct final migration point of damage resulting in the starting point of the shear band remaining in the imperfection zone. In conclusion, the proposed transient anisotropic model is capable of resolving both incorrect damage widening and migration issues when mode-II failure occurs in two-dimensional problems.

4

4.5. Conclusions

A transient anisotropic displacement-based gradient-enhanced damage model is formulated and used for failure analysis of quasi-brittle materials. In the proposed anisotropic formulation, the nonlocal interactions between the integration/material points are related to the stress states of the integration points. As a result of the anisotropic length scale based on the stress states, a relationship is established between the global response of the specimen (force-displacement curve) and the local response at integration points (strain-stress curve). First, the performance of the proposed model is evaluated for mode-I failure by means of a 4-point concrete beam test. The results show a deficiency of the proposed transient anisotropic model for removing spurious damage growth in mode-I failure and the presence of incorrect damage widening is still evident. Then, the model is tested for mode-II failure by means of a shear-band example. The results indicated that the proposed transient anisotropic model solves both incorrect damage widening and damage migration issues in the shear-band problem. A comparison of the force-displacement responses of the anisotropic and isotropic models indicated that the proposed transient anisotropic formulation has a higher mesh convergence rate than the transient isotropic model. As a result, in the case of mode-II failure, the transient anisotropic model provides more reliable results than the transient isotropic model.

4

References

[1] S. Teichtmeister, D. Kienle, F. Aldakheel, and M.-A. Keip, Phase field modeling of fracture in anisotropic brittle solids, International Journal of Non-Linear Mechanics 97, 1 (2017).

[2] T. T. Nguyen, J. Réthoré, and M.-C. Baietto, Phase field modelling of anisotropic crack propagation, European Journal of Mechanics-A/Solids 65, 279 (2017).

[3] J. Bleyer and R. Alessi, Phase-field modeling of anisotropic brittle fracture including several damage mechanisms, Computer Methods in Applied Mechanics and Engineering 336, 213 (2018).

[4] B. Li and C. Maurini, Crack kinking in a variational phase-field model of brittle fracture with strongly anisotropic surface energy, Journal of the Mechanics and Physics of Solids 125, 502 (2019).

[5] L. Wu, F. Sket, J. M. Molina-Aldareguia, A. Makradi, L. Adam, I. Doghri, and L. Noels, A study of composite laminates failure using an anisotropic gradient-enhanced damage mean-field homogenization model, Composite Structures 126, 246 (2015).

[6] B. Vandoren and A. Simone, Modeling and simulation of quasi-brittle failure with continuous anisotropic stress-based gradient-enhanced damage models, Computer Methods in Applied Mechanics and Engineering 332, 644 (2018).

[7] C. Geuzaine and J.-F. Remacle, Gmsh: A 3-d finite element mesh generator with built-in pre-and post-processing facilities, International journal for numerical methods in engineering 79, 1309 (2009).

4

5

Conclusions

A novel displacement-based gradient-enhanced damage model was proposed for bridging damage and fracture mechanics in quasi-brittle materials failure analysis to address incorrect damage initiation, widening, and migration issues observed with the gradient-based continuous damage models. To achieve this objective, a transient gradient activity function, as well as an anisotropic gradient activity function, were incorporated into the original displacement-based gradient-enhanced damage model. The original displacement-based model appropriately describes the discontinuous nature of the displacement field at the final failure stages. The proposed transient and anisotropic displacement-based gradient-enhanced damage models were numerically implemented into a two-field finite element method and applied on one- and two-dimensional benchmark examples under mode-I and mode-II failure conditions.

To achieve this goal, in Chapter 2, we relied on a one-dimensional setting to derive a new transient activity function. This chapter summarizes four transient activity functions that were chosen from fifteen transient activity functions that have been tested. These novel transient activity functions mobilize strain localization only in the damage process zone and neutralize it elsewhere. We have observed that the definition of a proper transient activity function requires careful consideration since some choices, such as those that decay rapidly from one to zero (meaning a fast localization process), result into mesh-dependent solutions. As the preliminarily transient activity function in the binary form was proposed in Section 2.3.1, its mesh-sensitivity study confirmed the correctness of the proposed regularization process. However, this model requires the input parameter ω_{crit} as a critical damage level, and by increasing this parameter, the model reverted to the original model with a constant length scale and exhibited again the incorrect damage widening issue. Furthermore, there is still no correct combination of the critical damage value, the constant gradient activity parameter, and the error tolerance used in the Newton-Raphson iterative procedure. When these parameters are combined incorrectly, and the damage profile is smooth, strain can also be localized incorrectly at more than one random location (generation of unrealistic spikes in the solution

97

fields) during a one-dimensional test. To avoid the extra model parameter ω_{crit} that was presented in the binary function, the transient activity function that is linked only to the damage field was tested and its mesh-sensitivity study confirmed the correctness of the regularization process proposed in Section 2.3.2. Our numerical investigations demonstrated that this transient activity function is unable to produce mesh-independent results in a two-dimensional setting, despite the fact that the model solved the incorrect damage widening in a one-dimensional setting. Due to the fast localization process of the proposed transient activity function, this transient activity function was unable to produce mesh-independent results with a reasonable fine mesh size in the damaged region. A problem similar to the unrealistic spike generation arises when using $g = 1 - \omega^n$ with a large exponent n. A third transient activity function was proposed in Section 2.3.3 to reduce the speed of the localization process, which takes into account both damage and nonlocal equivalent strain fields. Using this function, the mesh-sensitivity study confirmed its mesh-independency in a one-dimensional setting. However, this model failed to produce mesh-independent results for two-dimensional problems with a reasonable fine mesh size in the damaged region. As for the last transient activity function, in order to postpone the localization process in the displacement-based GEDM based on the same diffusion as the classical strain-based GEDM, a transient activity function was proposed in Section 2.3.4 and tested in Section 2.4.5 for one-dimensional problems. It was also tested in a two-dimensional setting that confirmed its capability to produce mesh-independent results with a reasonable fine mesh size in the damaged region.

Based on the pros and cons of the aforementioned functions in a one-dimensional setting, two-dimensional benchmark examples were simulated in order to evaluate these functions and determine a proper transient activity function in a two-dimensional setting, subject to mode-I and mode-II failure conditions. As a result of our two-dimensional numerical studies of different transient activity functions, we concluded that the transient activity function proposed in Section 2.3.4, based on equivalent dissipation, could be applied in this setting.

In Chapter 3, a transient displacement-based GEDM was formulated by incorporating the transient activity function in Section 2.3.4, and tested on the three benchmark examples. In this formulation, a constant (isotropic) gradient activity parameter was used. The numerical study indicated that by incorporating the transient length scale into the formulation of the displacement-based model, the incorrect damage widening, one of the main deficiencies of the existing gradient-enhanced damage models, is eliminated in mode-II failure. However, the proposed transient isotropic model in a two-dimensional setting does not perform as well as expected since it still shows incorrect damage widening in mode-I failure as well as incorrect damage migration in mode-II failure. These issues were addressed in Chapter 4 by the incorporation of an anisotropic gradient activity function, instead of the constant (isotropic) gradient activity function used in the formulation presented in Chapter 3. The results of a 4-point bending beam showed a deficiency of the proposed transient anisotropic model for removing the incorrect damage widening in mode-I failure. Then, the model is tested for mode-II failure by means of a

shear-band example. The results indicated that the proposed transient anisotropic model was able to solve both the issue of incorrect damage widening as well as the issue of damage migration in mode-II failure.

From a computational viewpoint an obvious deficiency of the proposed transient and anisotropic displacement-based gradient-enhanced damage models is the increase in the size of the element stiffness matrix (a 1.33 size increase in two-dimensional problems and a 1.5 size increase in three-dimensional problems compared to the element stiffness matrix of the strain-based gradient damage model). This increase could lead to problems for very large systems. In those cases, a suitable iterative solver could be considered. In addition, an adaptive coupled formulation of the governing equations can be used by activating the diffusion equation only in the damaged region.

In summary, the proposed model in this thesis could resolve the incorrect damage widening issue in a one-dimensional setting. However, it failed to resolve all incorrect damage widening and migration issues in a two-dimensional setting. It is therefore important to note that the displacement-based GEDM, which incorporates an anisotropic gradient activity function and a transient activity function, is merely the continuation of the process of developing a reliable model for quasi-brittle material failure analysis that is not currently available. The proposed displacement-based model requires further research in order to solve the incorrect widening and migration of damage as well as to reduce its computational cost.

5